Forschungszentrum Jülich

Institut für Plasmaphysik
EURATOM Association, Trilateral Euregio Cluster

Retention and Reemission Behaviour of Neon, Argon and Xenon on Graphite exposed to TEXTOR-94 Plasmas and Ion Beams

Young-Mo Kim

Jül-3670

Retention and Reemission Behaviour of Neon, Argon and Xenon on Graphite exposed to TEXTOR-94 Plasmas and Ion Beams

Young-Mo Kim

Berichte des Forschungszentrums Jülich ; 3670
ISSN 0944-2952
Institut für Plasmaphysik Jül-3670
EURATOM Association, Mitglied im Trilateral Euregio Cluster
D82 (Diss. RWTH Aachen, 1999)

Zu beziehen durch: Forschungszentrum Jülich GmbH · Zentralbibliothek
D-52425 Jülich · Bundesrepublik Deutschland
☎ 02461/61-6102 · Telefax: 02461/61-6103 · e-mail: zb-publikation@fz-juelich.de

Rückhaltungs- und Reemissionsverhalten von Neon, Argon und Xenon auf Graphit bestrahlt in TEXTOR-94 Plasmen und durch Ionenstrahlen

Kurzfassung

Die in TEXTOR-94 entdeckten "Radiative Improved Mode" (RI-Mode) Plasmen, bei denen durch den gezielten Einlaß von Verunreinigungen wie zum Beispiel Neon oder Argon eine strahlende Plasmarandschicht erzeugt wird, zeichnen sich durch einen verbesserten Energie- und Teilcheneinschluß aus. Trotz der bedeutenden Problematik der Rückhaltung und Rezyklierung der eingefügten Verunreinigungen (Ne, Ar, Xe) in den Wandkomponenten, liegen kaum detaillierte Untersuchungen zu diesem Themenkomplex vor. Deshalb wurden zum besseren Verständnis der RI-Mode die Eigenschaften der Rückhaltung und Rezyklierung von Neon, Argon und Xenon in und an Graphit in einer Ionenstrahlapparatur und in RI-Mode Plasmen an TEXTOR-94 untersucht.

Die Rückhaltungs- und Reemissionsprozesse von Neon und Argon in Graphit (EK98) wurden in der Ionenstrahlapparatur bei Ionenenergien von 2 bis 10 keV untersucht. In der Anfangsphase der Bestrahlung wird der größte Teil der einfallenden Ionen zurückgehalten. Nach Sättigung erreicht die Reemissionsausbeute einen Wert von eins. Die Desorptionsprozesse von Neon und Argon sind jeweils erster Ordnung. Es zeigt sich, daß Argon im Vergleich zu Neon ein breiteres Desorptionsspektrum mit höherer Maximumtemperatur (850 K, E_b = 2,06 eV für Argon bzw. 780 K, E_b = 2,35 eV für Neon) aufweist. Die Rückhaltungsmengen nach der Sättigung sind praktisch unabhängig von der Ionenenergie. **Die Sättigungskonzentration von Neon** (Ne/C = 0,15 für 10 keV bis Ne/C = 0,55 für 2 keV Ne^+) **ist größer als die von Argon** (Ar/C = 0,06 für 10 keV bis Ar/C = 0,18 für 3 keV Ar^+). Mit steigender Probentemperatur wird weniger Neon und Argon während der Bestrahlung zurückgehalten bis sich schließlich bei Temperaturen oberhalb 1200 K keine Rückhaltung mehr zeigt. Bei einer Nachbestrahlung der neonimplantierten Proben mit Deuteriumionen konnte keine ioneninduzierte Freisetzung von Neon durch Deuteriumbestrahlung beobachtet werden. Dies läßt sich wahrscheinlich auf zu niedrige Deuteriumfluenzen in Verbindung mit zu hohen Ionenenergien von Neon zurückführen. Bei Raumtemperatur wurde sowohl für Neon als auch für Argon keine Diffusion beobachtet. Für Argon wurden zusätzlich Messungen bis zu 800 K durchgeführt, bei denen ebenfalls keine Diffusion nachgewiesen werden konnte.

Bei den Untersuchungen im TEXTOR-Plasma wurde **eine neue Methode zur Bestimmung der gesamten Anzahl der in Plasmen eingefügten Verunreinigungen entwickelt**, die die

gesamte Bilanz des Einlasses und Abpumpens von Verunreinigungen berücksichtigt. Sowohl für die absolute Menge als auch für die Konzentration im gesamten Plasma ergeben sich, trotz geringerer Einlaßmenge von Argon, ähnliche Werte für Argon und Neon bei einem gleichen Strahlungspegel γ. Mit steigender Elektronendichte wurden geringere Mengen Neon und Argon im Plasma gemessen. Aus der Teilchenbilanz konnte sowohl die effektive Teilcheneinschlußzeit als auch die absolute dynamische Rückhaltung von Neon und Argon in den Wänden zeitlich verfolgt werden. Hierbei ergaben sich drei typische Phasen während des Verunreinigungseinlasses: In der ersten Phase (~ 100 ms für Neon) tragen die meisten der eingelassenen Verunreinigungen zu dem Aufbau der gewünschten Konzentration im Plasma bei (*Plasmapumpen*). Die zweite Phase (~ 600 ms) wird durch *dynamisches Wandpumpen* bestimmt. In der letzten Phase bis zum Ende des Verunreinigungseinlasses werden die meisten eingefügten Verunreinigungen schließlich durch den ALT II (Advanced Limiter Test II) abgepumpt (*ALT Pumpen*). Ein Vergleich der drei Pumpprozesse für Neon und Argon ergibt, daß der größte Teil von Neon (bis zu 70 %) durch ALT Pumpen entfernt wird. Dieser Pumpmechanismus trägt beim Argon nur bis zu maximal 50 % bei. Es zeigt sich, daß lediglich bis zu 15 % des eingelassenen Neons durch Wandpumpen abgepumpt wird, wohingegen dieser Mechanismus bei Argon bis zu 50 % beiträgt. Die Ausgasmenge von Argon (~ 50 % der Einlaßmenge) nach der TEXTOR-Plasmaentladung stimmt gut mit dem aus der Teilchenbilanz abgeschätzten Wert überein. Argon und Xenon zeigen dabei gleiche Freisetzungsraten, deren zeitliche Entwicklung sich proportional zu $t^{-1.1}$ verhalten.

Der Ionenfluß und die Rückhaltung von Wasserstoff und Verunreinigungen (Ne, Ar) in Graphit wurden in der Abschälschicht des Plasmas mittels der sogenannten Schnüffelsonde gemessen. Mit steigendem Verunreinigungseinlaß nimmt der Wasserstoffffluß stark ab, was eine Reduzierung der konvektiven Wärmebelastung der Wand zur Folge hat. Das Flußverhältnis von Verunreinigung zu Wasserstoff am Plasmarand beträgt bis zu 30 % für Neon und einige Prozent für Argon. Aus dem Vergleich der Verunreinigungskonzentration im Zentrum und am Plasmarand kann auf ein Hohlprofil der Verunreinigungskonzentration in radialer Richtung geschlossen werden. Die in der Schnüffelsonde gemessenen Rückhaltungsmengen von Neon und Argon in Graphit liegen bis zu einer Größenordnung über dem aus der Teilchenbilanz abgeschätzten Wert der Zurückhaltung in den ALT-Limitern. Diese Diskrepanz wird auf die unterschiedliche Geometrie- und die erhöhte Temperatur der ALT-Limiter zurückgeführt. Andererseits sind die in der Schnüffelsonde gemessenen Rückhaltungsmengen von Neon und Argon in Graphit aus dem TEXTOR-94 Plasma bis zu zwei Größenordnungen kleiner als die in Ionenstrahlexperimenten gemessenen Werte. Dieser Unterschied wird hauptsächlich mit der ioneninduzierten Freisetzung von Verunreinigungen durch das Wasserstoffplasma erklärt.

Abstract

The recently in TEXTOR-94 discovered Radiative Improved mode (RI-mode) plasmas, at which a radiating plasma boundary is produced by a controlled seeding of impurities such as neon or argon, are showing an improved energy- and particle-confinement. Despite the importance of the characteristics of retention and recycling of the impurities seeded, there are only a few direct investigations concerning this. For a better understanding of the RI-mode, the characteristics of retention and recycling of neon, argon and xenon in and on graphite were investigated in ion beam experiments and in RI-mode plasma of TEXTOR-94.

The retention and reemission processes of neon and argon in graphite (EK98) were investigated in an ion beam apparatus with ion energies between 2 and 10 keV. In the early phase of irradiation the majority of incident ions are retained. After saturation, the reemission reaches unity. The desorption processes of both neon and argon are first order ones. Argon, in comparison with neon, has a broader desorption spectra with a higher maximum temperature (850 K, E_b = 2.06 eV, for argon and 780 K, E_b = 2.35 eV for neon). The retention at saturation is almost independent of ion energy. **The saturation concentration of neon** (Ne/C = 0.15 for 10 keV Ne^+ up to Ne/C = 0.55 for 2 keV Ne^+) **is larger than that of argon** (Ar/C = 0.06 for 10 keV Ar^+ up to Ar/C = 0.18 for 3 keV Ar^+). Ion induced release of neon was simulated by irradiating the neon saturated graphite with deuterium ion. In this trial no ion induced release was observed. However, for a better simulation of this effect under TEXTOR plasma conditions, lower ion energies of neon and deuterium and larger fluence of deuterium are needed. With increasing sample temperature less neon and argon are retained in graphite during the irradiation with ion beams and above 1200 K no retention is observed. No diffusion of neon and argon was measured at room temperature. For argon additional experiments were carried out, in which no diffusion of argon up to 800 K was observed.

From the investigations in the TEXTOR plasma **a new method to determine the total amount of impurity seeded in the plasma was developed** from the overall balance of impurity seeding and pumping. The amounts and concentrations of neon and argon in the whole plasma are, though less amount of argon seeded, similar for the same radiation level γ. With increasing electron density, less amounts of neon and argon in the plasma were measured in the plasma. From the particle balance **it was possible to deduce the effective particle confinement time and the absolute dynamic retention of neon and argon as a function of time.** The dynamic retention can be divided into three phases during the impurity seeding period. In the first phase (~ 100 ms for neon), the majority of impurity seeded is contributed to build-up the desired concentration in the plasma (*plasma pumping*). The second phase (~ 600 ms) is dominated by *dynamic wall pumping*. In the third phase (until the end of the impurity injection), most of the impurity seeded are pumped out by ALT II (Advanced

Limiter Test II) pump (*ALT pumping*). Comparing the integration of the three pumpings of neon and argon; a larger portion of neon is pumped out via ALT pumping (up to 70 %) than argon (up to 50 %). *The wall pumping plays a greater role for argon* (up to 50 %) *than for neon* (up to 15 % of the injected neon). The outgassing of argon after the TEXTOR plasma discharges(~ 50 % of argon seeded) complies with that expected from particle balance. Argon and Xenon show the same release rate proportional to $t^{-1.1}$.

The ion flux and the retention of hydrogen and impurities (Ne, Ar) in graphite sample at the plasma edge (r = 0.49 m) were measured in the Sniffer probe. The hydrogen flux decreases significantly with increasing impurity seeding, which implies the decrease of convective power load onto the walls. *The flux ratio of impurity to hydrogen at the plasma edge reaches up to ~ 30 % for neon and several percent for argon.* From the comparison of impurity concentrations at plasma centre and edge, it is considered that the impurity concentrations have a hollow-like radial distribution. The retention of neon and argon in graphite, measured in the Sniffer probe, is up to one order of magnitude larger than those in the ALT limiters estimated from the particle balance, which is presumably due to the different geometry and higher temperature of the ALT limiters. On the other hand, the retention of neon and argon in graphite from TEXTOR-94 plasma measured in the Sniffer probe are up to two orders of magnitude smaller than those measured in the ion beam experiments. This discrepancy is explained by the *ion-induced release of impurities via hydrogen plasma impact.*

Table of contents

List of Symbols

M_{Ne}	:	Calibration factor of Ne VIII ($=\frac{N_{Ne}}{NeVIII}$)
$c_{Ne,G}$	:	Concentration of neon in plasma measured by global observation
τ_p^*	:	Effective particle confinement time [s]
P_{wall}^*	:	Effective wall pumping rate (Retention rate in the wall) [s^{-1}]
τ_E	:	Energy confinement time [s]
Γ_{ext}	:	External impurity seeding rate [s^{-1}]
τ_p	:	Global particle confinement time [s]
n_e	:	Line averaged central electron density [m^{-3}]
P_{plasma}	:	Plasma pumping rate [s^{-1}]
P_{ALT}	:	Pumping rate of ALT Limiter [s^{-1}]
IP_{wall}^*	:	Total amount of effective wall pumping (integration of P_{wall}^*)
IP_{plasma}	:	Total amount of plasma pumping (integration of P_{plasma})
N_{Ar}	:	Total number of argon in plasma at stationary state
N_{Ne}	:	Total number of neon in plasma at stationary state
IP_{ALT}	:	Total number of particle pumped out by ALT Limiter
γ	:	Radiated power level (= P_{rad}/P_{tot})
$\Phi_{Htot,S}$	:	Hydrogen flux measured in Sniffer probe
$\Phi_{Ne,S}$	:	Neon flux measured in Sniffer probe
ϕ_s	:	Sheath potential
ALT limiter	:	**A**dvanced **L**imiter **T**est limiter
B_P	:	Poloidal magnetic field
B_T	:	Toroidal magnetic field
B_V	:	Vertical magnetic field
$c_{Ne,S}$	:	Neon concentration at SOL measured by Snifferprobe (= $N_{Ne}/n_{e,tot}$)
CXRS	:	**C**harge e**X**change **R**ecombination **S**pectroscopy
ECRH	:	**E**lectron **C**yclotron **R**esonance **H**eating [MW]
E_{ion}	:	Ion energy [eV]
EOPG	:	**E**dge **O**riented **P**yrolytic **G**raphite
E_{rad}	:	Radiation Potential [keV]
ICRH	:	**I**on **C**yclotron **R**esonance **H**eating [MW]
I_p	:	Plasma current [kA]
ITER	:	**I**nternational **T**hermonuclear **E**xperimental **R**eactor
LCFS	:	**L**ast **C**losed **F**lux **S**urface

NBI	:	**N**eutral **B**eam **I**njection [MW]
NeVIII	:	Line radiation of Li-like neon ion (2s-2p, λ =77.4 nm)
$n_{e,tot}$	:	Total Number of electron in plasma
P_α	:	α-heating power
P_{rad}	:	Total radiation power [MW]
P_{tot}	:	Total heating power [MW]
QMS	:	**Q**uadruple **M**ass **S**pectrometry
R	:	Recycling coefficient
RBS	:	**R**utherford **B**ack **S**cattering
RES	:	**R**adiation **E**nhanced **S**ublimation
RI-mode	:	**R**adiative **I**mproved mode
$R_{Ne,G}$	:	Retention density of neon measured by global observation
$R_{Ne,S}$	:	Retention density of neon measured in the Sniffer probe
R_p	:	Mean implantation range [nm]
S	:	Stopping cross section
SOL	:	**S**crape **O**ff **L**ayer
TDS	:	**T**hermal **D**esorption **S**pectroscopy
$T_{e,edge}$	:	Electron temperature at the plasma edge [eV]
TEXTOR	:	**T**orus **EX**periment for **T**echnology **O**riented **R**esearch
$T_{i,edge}$	:	Ion temperature at the plasma edge [eV]
T_p	:	Temperature of maximum desorption spectra
Y_{Re}	:	Reemission yield
Z_{eff}	:	Effective charge number of plasma

1. Introduction

It has been one of the most confronting tasks of mankind to solve the energy problem. In these days this problem has become a matter of great urgency than at any other time since the conventional energy sources are not inexhaustible and are becoming less acceptable environmentally. Nuclear fusion, due to its inexhaustibility and environmental affinity, has been intensively investigated during the past several decades as a promising alternative energy source.

1.1 Nuclear Fusion

The sun is a good example of nuclear fusion. In the nuclear reaction two light nuclei combine to produce a heavier nucleus, the mass defect in this process ($\Delta E = \Delta m \cdot c^2$) is converted into kinetic energy of the fusion product. Among the several candidates for the nuclear fusion with light isotopes, the D-T reaction is, due to its high cross section, most intensively investigated:

$$^2\mathrm{D} + {}^3\mathrm{T} \Rightarrow {}^4\mathrm{He}\ (3.52\ \mathrm{MeV}) + \mathrm{n}\ (14.1\ \mathrm{MeV}). \qquad (1\text{-}1)$$

In order to overcome the Coulomb barrier, the energies of the reaction partners should be high enough. However with the help of the tunnelling effect the fusion reaction can occur with a sufficient rate at temperatures of about 10-20 keV, which is much lower than predicted from the Coulomb interaction alone.

To sustain a *self-consistent* fusion reaction, the total power loss out of the plasma should be compensated by the heating power from the fusion process (*ignition*). The total power loss can be characterised by the ratio of total thermal energy of plasma and the total power loss, which defines the energy confinement time τ_E. The ignition condition is usually expressed by the triple product of plasma density n, energy confinement time τ_E and plasma temperature T. To achieve the ignition, this triple product for a pure D-T plasma has to be

$$n \cdot \tau_E \cdot T \geq 4.5 \cdot 10^{21}\ \mathrm{m^{-3}s\ keV} \qquad (1\text{-}2)$$

where $n = n_D + n_T$. Up to now, two main confinement concepts have been investigated in order to achieve this condition: one concept is *the inertial confinement*, in which the fuels are heated up to the needed temperature within a very short time period (10^{-9} – 10^{-7} s) with intensive laser pulses to very high densities (~ 10^{32} $\mathrm{m^{-3}}$). In the second concept, *the magnetic*

confinement, charged particles are confined via a strong magnetic field, in which the prerequisite temperature is reached by the energy transfer within collisions of the fuel ions (relatively low density ~ 10^{20} m^{-3}) with the highly energetic fusion product (^{4}He with 3.52 MeV in case of D-T).

1.2 Tokamak and Technical Issues

The tokamak concept (from Russian: **to**roidalnaya **Ka**mera **ma**gnitnaya **k**atushka), in which the hot plasma is confined in a torus form by strong magnet fields, is the most worldwide investigated concept of magnetic confinement. As shown in fig. 1-1, the torus-like reactor vessel is surrounded by many toroidal field coils. Constant currents running through the toroidal field coils provide a toroidal magnetic field (B_T). A set of transformer coils generates an inductive plasma current (I_p) in the toroidal direction using the plasma as the secondary winding. A poloidal magnetic field (B_P) is induced by the plasma current and added to the toroidal magnetic field B_T resulting in a magnetic field line which is helically screwed around the torus. With the help of vertical field coils (B_V) the position of the plasma can be adjusted at a controlled position.

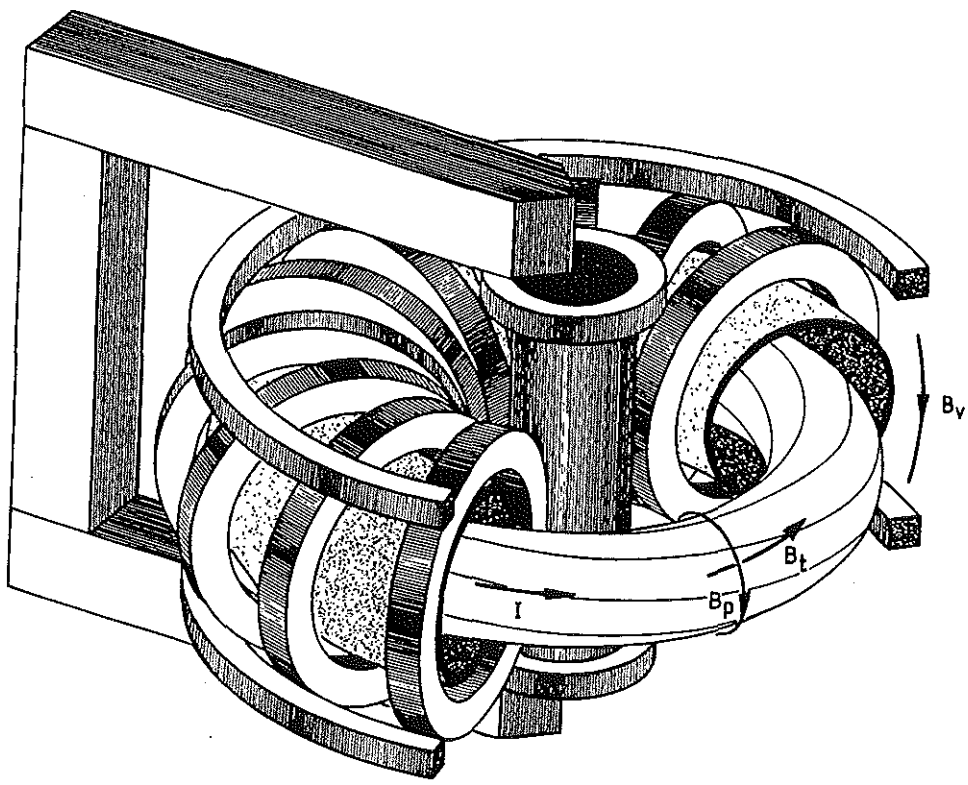

Figure 1-1 : Schematic diagram of tokamak principle.

Heating of the plasma is done at first, due to the plasma resistivity, by the plasma current itself, called ohmic heating. Since the ohmic heating, which however decreases with increasing plasma temperature due to the decrease of the plasma resistivity, is limited, auxiliary heating systems are inevitable: NBI (**N**eutral **B**eam **I**njection) and ECRH (**E**lectron **C**yclotron **R**esonance **H**eating) or ICRH (**I**on **C**yclotron **R**esonance **H**eating) are most usually applied.

The confinement, however, in a tokamak is not perfect. Radial transport, through Coulomb collision, drift and turbulence, leads to the escape of particles from the plasma. This results in energy and particle fluxes to the wall components. In order to protect the wall components and the vacuum chamber from these particle fluxes and heat loads, two concepts are used in today's tokamaks as shown in fig. 1-2:

- ***Limiter*** defines directly the last close flux surface and takes over the heat and particle flux from the plasma. Among the several types of limiter concepts, a successful realisation of a limiter concept was achieved by the pump limiter in TEXTOR and JET (fig. 1-2(a)).

- ***Divertor*** uses a special magnetic configuration which turns the magnetic field line of plasma edge into a separate divertor chamber to the target plate. Charged particles moving along the magnetic field impinge onto the target plate and are neutralised.

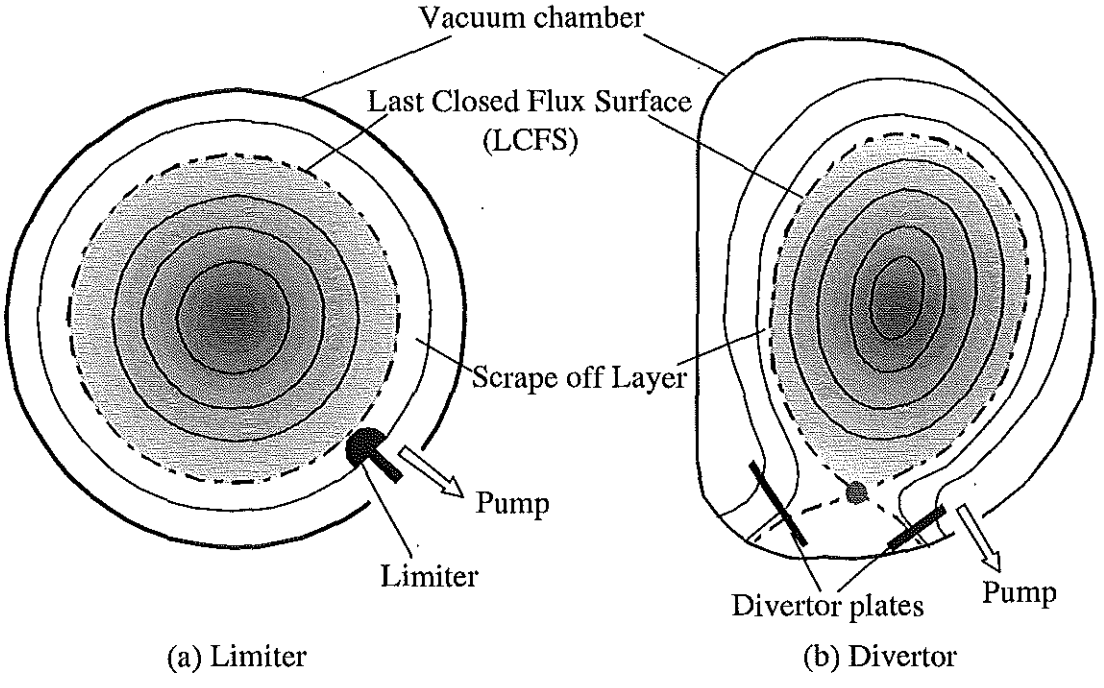

Figure 1-2 : Schematic diagrams of **(a)** limiter and **(b)** divertor configuration.

It is apparent that the thermal load and the sputtering are concentrated on the limiter or divertor targets. In the latest ITER (**I**nternational **T**hermonuclear **E**xperimental **R**eactor) design report about 600 MW of α-particle thermal power is assumed, from which a heat flux of ~ 50 MWm^{-2} on the limiter or divertor plates is expected. This is far beyond the technically acceptable limit of about 5 MWm^{-2} for the stationary operation. One of the most promising ways to solve this problem is to spread the thermal load homogeneously onto the whole wall by extracting the power in form of electromagnetic radiation. This concept is called '***Radiation Cooling***'. Various possibilities of this concept have been discussed since 1970s but realised in a systematic way for the first time in TEXTOR by seeding impurities such as neon into the plasma [Sam93,Mes96]. This will be described in the following chapter. With neon or argon impurity seeding, up to 90 % of the input heating power could be exhausted via radiation in TEXTOR by which the thermal load on the limiter was significantly reduced. It was a very surprising result that by seeding the neon impurities the energy confinement was much improved. This regime is called **R**adiative **I**mproved confinement mode, ***RI-mode***.

1.3 Objectives of this Thesis

With respect to the RI-mode discharge, *the understanding of the retention and recycling characteristics of the seeded impurities such as neon or heavier noble gases in graphite as wall materials is of particular interest.* Noble gases were never seeded intentionally into the fusion devices before the radiation cooling was considered. For this reason only *a small data base on the retention and recycling of neon or argon in graphite is available.* As an exception, Brosset et al. have investigated the retention of neon and the influence of simultaneous impact of incident hydrogen using glow discharge techniques [Bro97]. Choi et al. have investigated the retention of helium, neon and argon in graphite with low energy (10 - 600 eV) ion beam irradiation [Cho93]. Though the laboratory data are helpful to predict the retention and recycling of noble gases, taking into account the quite different conditions in a tokamak with higher fluxes up to 10^{21} $m^{-3}s^{-1}$ and also the simultaneous impact of incident hydrogen, which always takes part in the majority of the impinging species (more than 90 %), it is difficult to describe the retention and recycling of noble gases in fusion devices. Up to now there is no direct measurement of the retention and recycling of neon and other noble gases in fusion environments. An exception is the retention and recycling of helium, which has been investigated to some extent. In fusion experiments with carbon walls it has been concluded that the wall retention of helium is very small or negligible. The objectives of this thesis can be listed as following:

- Experimental determination of the retention and recycling characteristic of neon and argon in graphite under ion beam impact conditions as a function of both the ion energy and sample temperature.

- Quantitative determination of the overall dynamic retention and recycling behaviour of different noble gases in TEXTOR discharges via global observations and the indirect determination of the retention of noble gases in the first wall components.

- Direct measurement of the incident flux and the retention of noble gases within a graphite sample exposed in the scrape off layer and comparison with global observations

In the following section, a brief review of the basic physics related to this thesis and the key features of the concept of radiation cooling are presented.

In section 3 and 4, the retention and reemission behaviour of neon and argon measured in the ion beam experiments are presented.

In section 5, the experimental facility for the measurement of the ion fluxes and their retention (Sniffer probe) in TEXTOR-94 is described.

Section 6 describes the detailed results of the dynamic retention of neon, argon and xenon during the discharge together with the results of Sniffer probe experiment.

The summary of this thesis is presented in section 7.

2. Basic Physics

2.1 Tokamak Edge Plasma

The boundary region of the plasma can be divided into two zones: a zone inside the **L**ast **C**losed magnetic **F**lux **S**urface (LCFS) in which the ionization processes and also a large part of the radiation of low Z impurities takes place and the **S**crape-**O**ff **L**ayer (SOL) which is the region outside the LCFS. In the scrape off layer the magnetic field lines are open since they are cut by the target plates such as limiters or divertors. Charged particles in the SOL travel along the magnetic field line until they impact onto the target surface. In the following section several important *plasma-wall interaction processes* will be described.

While a certain (small) part of the incident particle flux onto the target plates are retained and thus leave the plasma, most of the particles are backscattered or released again by various mechanisms from the surface. Released particles are excited and ionized again by the plasma and contribute again to the plasma. This overall process is called ***recycling***. The characteristic of the recycling is dependent on the nature of incident particles and of the target materials used. This will be discussed in the following section in more detail.

Due to the smaller mass of the electrons, their flow to the surface in the scrape off layer is much larger than that of the ions. In consequence the surface is charged up negatively with respect to the bulk plasma so that the flow of electrons and ions are balanced and the electrons are repelled and ions are accelerated (***Debye Sheath***). This negative potential is due to the balance of the ion and electron fluxes, from which the sheath potential (ϕ_s) can be derived [Sta86]:

$$\frac{e\phi_s}{kT_e} = 0.5 \ln\left[2\pi \cdot \frac{m_e}{m_i}\left(1+\frac{T_i}{T_e}\right)(1-\delta)^{-2}\right] \qquad (2\text{-}1)$$

where T_i and T_e are ion and electron temperatures, m_i and m_e are the ion and electron masses respectively and δ is the secondary emission coefficient. For a hydrogen plasma the sheath potential (ϕ_s) is about $3kT_e$. One can then derive the ion energy incident onto the surface by the summation of ion energy entering the sheath ($2kT_i$) and that gained in the sheath ($3Z{\cdot}kT_e$) [Rei98]:

$$E_{ion} = 2kT_i + 3Z{\cdot}kT_e\,. \qquad (2\text{-}2)$$

where Z is the charge number of the ions. Taking into account the typical electron temperature at the plasma edge (20 – 80 eV) and the average charge number of deuterium (1), neon (5.5) [Unt97] and argon (5 - 7) [Unt99]; one can estimate the ion energies impinging on the target plate of deuterium $E_{ion,D}$ = 150 – 400 eV, neon $E_{ion,Ne}$ = 400 – 800 eV and argon $E_{ion,Ar}$ = 400 – 1000 eV.

2.1.1 Basic processes of plasma-wall interaction

Projectiles incident onto a solid target lose their energy via two collision processes: **first**, projectiles transfer their energy and momentum to the solid atoms in elastic collisions. **Second**, projectiles transfer their energy to free electrons leading to excitation or ionization (*inelastic collision*). If the transferred energy by elastic collision is larger than a specific limit (displacement energy), the target atoms leave the lattice leaving a vacancy behind and forming an interstitial (*displacement*). If the energy transfer to the lattice atom is large enough, the recoiled atom itself can displace other lattice atoms, producing a so called collision cascade.

2.1.1.1 Implantation

In the following, incident ions which penetrate the surface and slowed down in the target lattice are considered. The loss of kinetic energy E of an incident atom per unit path length x is described by the stopping cross section (S):

$$S = -\frac{1}{n} \cdot \frac{dE}{dx} \tag{2-3}$$

where n denotes the target atomic density. In the case of inelastic collision, the angular deflections of the atoms during this collision are negligibly small due to the small relative mass of electron. In the case of elastic collision, the incident particles can be deflected significantly. Consequently, the total stopping cross section is divided into an 'electronic' and 'nuclear' fraction. In the case of neon implantation in the graphite target, the nuclear stopping power has its maximum in the ion energy range of several keV and is dominant in the ion range of less than 10 keV. Detailed descriptions of each stopping process is found in [Zie84,Möl86]. When the total stopping cross section is known, the mean total path length of implanted ions (implantation range: R_p) can be calculated as following

$$R_p = \frac{1}{n} \cdot \int_0^{E_0} \frac{dE}{S(E)} \tag{2-4}$$

where E_0 is the incident energy. In the case of the irradiation with a great number of ions, it is shown that the implanted ions have a Gaussian distribution in the homogeneous and endless target bulk [Lin61]. With the help of simulation programs such as TRIM [Zie87], it is possible to calculate the implantation range and the width of the distribution.

2.1.1.2 Physical sputtering

Due to the collision cascade the energy transfer to surface atoms may exceed their binding energy of the surface or highly energetic recoils may leave the solid directly. This is called ***physical sputtering*** [Eck96]. Physical sputtering is the most important mechanism of impurity release processes since it occurs for all materials regardless of their chemical nature, wall condition and wall temperature. The basic concept of physical sputtering is shown in a simple case in fig. 2-1. The projectile or the recoiled atoms transfer enough energy to the surface (or subsurface) atom so that it exceeds the surface binding energy. It is apparent that the sputtering yield, defined as the ratio of the number of sputtered atoms and projectiles, should have a threshold value of E_{th} since no surface atom can leave the solid surface if the maximum transferable energy is smaller than the binding energy (U_s). Introducing the maximum energy transfer factor γ (ratio of the maximum transferable energy to the recoiled atom and the energy of projectile), one can express the threshold energy as follows:

$$E_{th}(1-\gamma)\gamma \geq U_s . \tag{2-5}$$

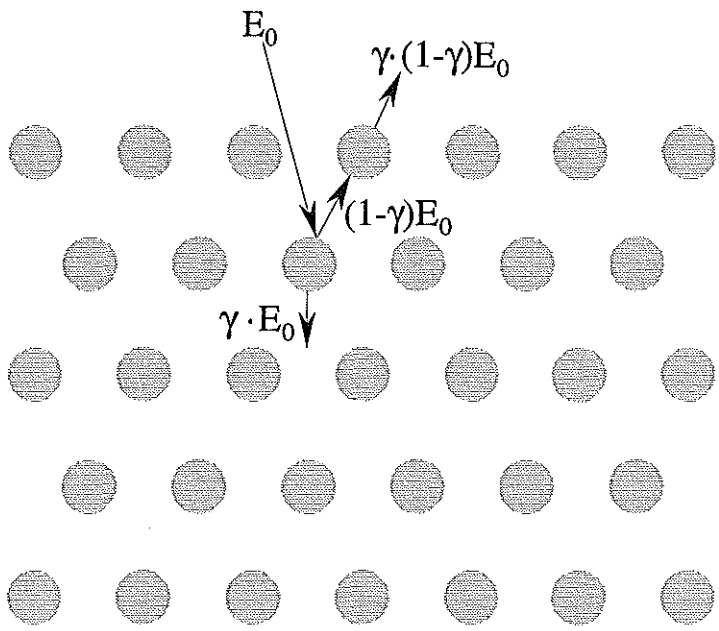

Figure 2-1 : Schematic sketch of the energy transfer in physical sputtering.

As discussed, physical sputtering is due to the elastic collision. Therefore the energy transfer reaches its maximum when the masses of the projectile and the target atom are identical, which is called ***self sputtering***. It is obvious that for the impact of light projectiles the energy transfer in the elastic collision decreases strongly with increasing target mass, leading to an increase of E_{th}. This is why high-Z materials are considered to be attractive in the fusion devices.

2.1.1.3 Chemical erosion

Some projectiles can cause erosion of the target material by forming volatile molecules via chemical reaction with the target material, which is called ***chemical erosion*** [Rot83]. While all projectiles can cause in principle physical sputtering with all target atoms, chemical erosion occurs only for certain projectile-target atom combinations. Chemical erosion is of great importance for present and for future fusion devices since graphite, which suffers severely from chemical erosion, is still the most promising material for the plasma facing material. Chemical erosion of carbon occurs due to the formation of hydrocarbons by interaction with the plasma fuel (hydrogen atoms) and the formation of CO and CO_2 by interaction with oxygen. Different from physical sputtering, chemical erosion depends on the target temperature [Vie82]. Methane formation, e.g. has its peak yield at a target temperature of about 800 K. Chemical erosion by oxygen (formation of CO and CO_2) has a very high erosion yield ($(CO+CO_2)/O$) and shows little dependence on the projectile energy and the target temperature. Since via CO and CO_2 additional carbon impurities enter the main plasma, the control of the oxygen impurity content is of great importance in order to reduce the impurity content in the plasma.

2.1.1.4 Radiation enhanced sublimation (RES)

One of the greatest advantages of carbon is that it does not melt and retains thus its shape at any temperature. Thermal sublimation of carbon happens at a very high temperatures of above 2500 K. Carbon however has an additional sublimation process which is called **R**adiation **E**nhanced **S**ublimation (RES) [Phi98]. This effect, which leads to the emission of carbon atoms with thermal energy, is observed only for carbon as a target material under the bombardment of any energetic projectiles [Phi91]. RES is considered to be due to the formation of carbon interstitials by energetic particle impact. Some of these carbon interstitials diffuse to the surface and are desorbed thermally, due to their low surface binding energy, at the temperature far below that for pure thermal sublimation.

2.1.1.5 Ion induced release

Winters et al. [WinB74] show that the sputtering yields of adsorbed nitrogen within the several monolayers of tungsten target bombarded by nitrogen ions are surprisingly large. This phenomena can be accounted for by the dynamics of collision processes leading to sputtering which is called *'ion induced release'* [Sig69]. Fig. 2-2 shows three different mechanisms that are dominating the sputtering of an atom adsorbed on a thick target bulk.

I ***An incident ion hits an adsorbed atom.*** The adsorbed atom is reflected from the target lattice either directly, for oblique incidence, or at high enough energy after some penetration.

II ***An incident ion penetrates into the target, and eventually reflected.*** The ion, on its

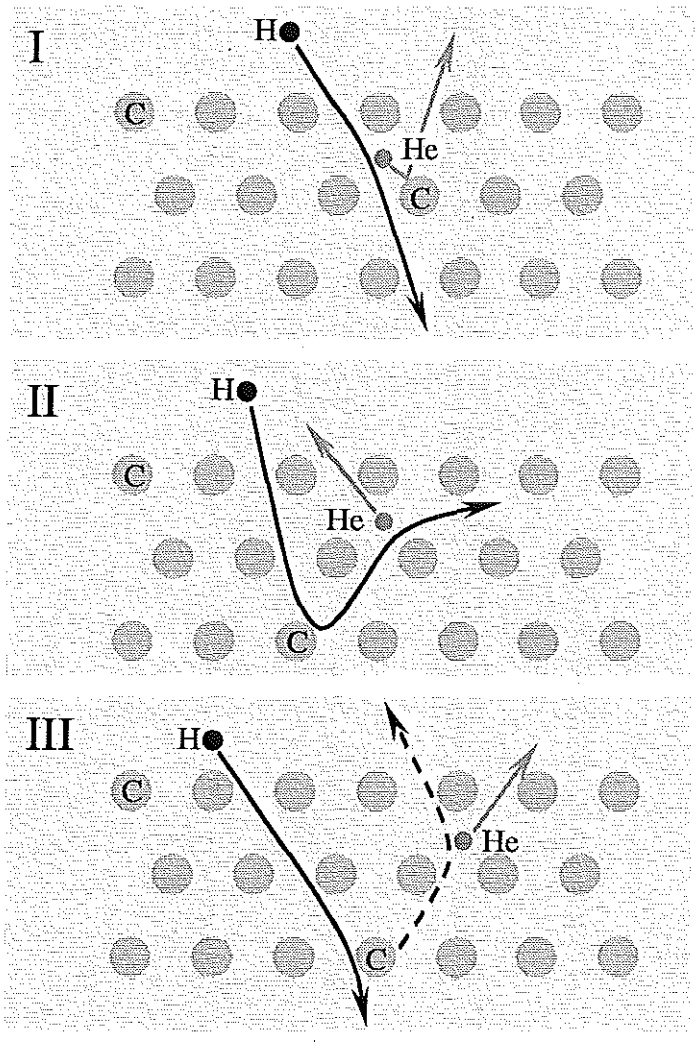

Figure 2-2 : Schematic sketch of three possible postulated release processes of ion induced release.

way out, may also knock off an adsorbed atom. This mechanism is dependent on the reflection of the incident atom on the target atom.

III ***The incident ion causes an outward flux of target atoms near the surface, i.e. sputtered flux.*** Some of these atoms may knock off the adsorbed atoms on their way out.

Since reflection is the crucial process in mechanisms I and II, I and II have a maximum energy for incident ions. For the same projectile atom the maximum energy increases with increasing mass of adsorbed atom. Mechanism III, increases monotonically with increasing projectile energy, has a threshold energy due to the sputtering of lattice atoms. These processes happen only within several monolayers of the target lattice and are more significant for light adsorbed atoms.

2.1.1.6 Thermal desorption

When the thermal excitation of adsorbed particles is large enough to overcome the adsorbate-substrate binding energy (activation energy), the bondage of adsorbate-substrate is broken and the adsorbed particle can be released from the substrate surface. This phenomena is called *thermal desorption* and the rate of desorption can be expressed as following [Gum90]:

$$N(t) = -\frac{d\Theta}{dt} = \nu_m \Theta^m e^{-\frac{E_b}{RT}} \qquad (2\text{-}6)$$

where m is the order of the desorption reaction; Θ ($= N/N_0$) is the surface coverage with N the number of adsorbed particles and N_0 the total number of substrate surface atoms per cm^2; ν is the preexponential factor; and E_b is the activation energy of desorption. The order of desorption m describes the dependence of the desorption rate on the concentration of the reactants adsorbed on the surface. In the case of first order desorption (m = 1), the preexponential factor ν is connected with the vibrational frequency of the adsorbed atoms. In the case of second order desorption (m = 2), ν is connected with the number of collisions per unit time per unit concentration of adsorbed atoms. The activation energy of desorption (E_b) describes the binding of adsorbed on the substrate atoms. Since ν, E_b and m are dependent on coverage, the exact analysis of the thermal desorption spectra (TDS) is very complex. Therefore the most frequently used TDS analysis is based on a given m and the assumption that ν and E_b are independent of the coverage.

From the spectral shape and their dependence on the coverage the order of desorption can be identified. For the case of **the first order desorption** the peak energy (T_p) is independent

to the initial coverage Θ_0, and the spectral shape is slightly unsymmetric. In the case of **the second order desorption** the peak temperature increases with increasing initial coverage and the spectral shape is symmetric. For the case of first order desorption, the relation of E_b and T_p is linear over wide range of ν_1/β ($10^8 < \nu_1/\beta < 10^{13}$ K^{-1}, where β is the heating rate) and can be determined from the measured peak temperature T_p [Red62]:

$$\frac{E_b}{RT} = \ln\frac{\nu_1 T_p}{\beta} - 3.64 \qquad (2\text{-}7)$$

where the preexponential factor ν_1 is assumed 1×10^{13} s^{-1}.

2.1.2 *Particle balance and recycling*

The confinement of particles in the plasma is characterised by *the ratio of the total number of particles (N) in the plasma to the outgoing flux* (Γ_o) of particles. This time is called ***particle confinement time*** τ_p:

$$\tau_p = \frac{N}{\Gamma_o}. \qquad (2\text{-}8)$$

When plasma ions or neutrals impinge onto the wall components, they undergo a series of elastic and inelastic collisions with the atoms of the solid. Some of them are released immediately via elastic reflection. Others are trapped physically or chemically in the solid but can also be released from the solid when the trapping reaches its saturation or when the trapped particles diffuse to the surface. The released neutrals from the surface are ionized and come back to the surface again. This process is called ***recycling*** and the ratio of the released to the incident flux is called ***recycling coefficient R***. The recycling coefficient determines thus how much of the outgoing flux is released back into the plasma. From this one can define the ***effective particle confinement time*** (τ_p^*) as following [Ehr96]:

$$\tau_p^* = \frac{N}{\Gamma_o - R\Gamma_o} = \frac{\tau_p}{1-R}. \qquad (2\text{-}9)$$

While τ_p is determined by the diffusion processes inside the plasma and τ_p^* is determined by the recycling characteristic of the projectile particle at a given wall surface. Concerning the recycling characteristic, elements can be divided into two categories:

- ***Fully recycling species*** ***(R ~ 1)*** : these species undergo many recycling processes, which results in a much larger τ_p^* in comparison to τ_p. Elements which have *no chemical binding* with the solid surface e.g. *noble gases* are typical examples.

- ***Condensing species (R ≪ 1)*** : these elements easily condense onto the solid surface, which results in a τ_p^* which is not much larger than τ_p. Typically these elements are chemically bonded on the solid surface and released by the processes mentioned above. Carbon and silicon are typical condensing elements.

2.2 Radiation Cooling

In the concept of the '***cold, radiating plasma mantle***' the power is distributed over the whole vessel walls via edge line radiation from the injected impurities. In this way the peak load of the convective power on to the limiter or divertor is significantly reduced. Details of this concept can be found in [Unt95], and the following section describes only the key aspects of it, as shown schematically in fig. 2-3. At first glance it seems contradictory to have a strong radiation loss without any drawback of fusion process since the radiation loss means immediately a loss of fusion power. The radial profiles of electron temperature and of the α-heating power density (P_α) profile as expected in ITER [Cum90] (in fig. 2-4) show, however, that *the outer edge of the plasma does not significantly influence the fusion process*: The α-heating power density P_α is proportional to the density of fuel ions ($n = n_D + n_T$) and the rate coefficient of fusion process ($\langle \sigma v \rangle_{DT}$: integration of the cross-section over the velocity with Maxwellian velocity distribution). With the α-particle energy of E_α, one can describe the α–heating power density as following [Wes87]:

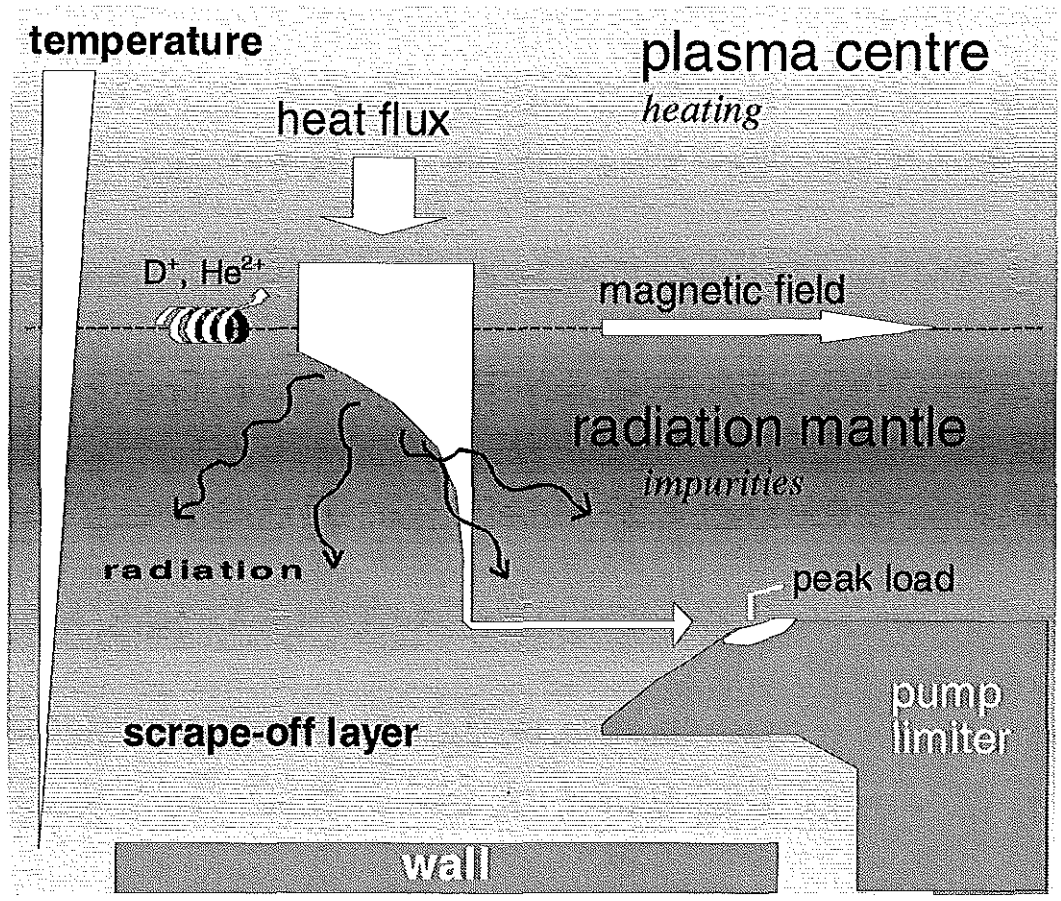

Figure 2-3 : Schematic illustration of radiation cooling concept.

$$P_\alpha = \frac{1}{4} n^2 \langle \sigma v \rangle_{DT} E_\alpha . \qquad (2\text{-}10)$$

As shown in fig. 2-4, it is apparent that in the region r/a > 0.8 the contribution to the fusion process is negligible. If the radiating zone is restricted only to this region, it is not harmful for the fusion process.

The impurity radiation is the combination of line radiation (emission of radiation from the de-excitation of atom or ions) and continuous radiation (bremsstrahlung radiation and recombination). It is reported by Summers et al. [Sum79] that under the typical plasma edge conditions ($10^{18} < n_e < 10^{19}$ m^{-3}, $10 < T_e < 100$ eV) the line radiation dominates the impurity radiations. Therefore it is of great importance to choose the impurity species for radiation cooling so that the line radiation of the impurity seeded is well restricted in the region of the plasma edge. The dimension of the line radiation-dominant region is mainly dependent on the charge number Z of the impurity species that decides how many ionization states up to the fully ionized state are possible and how high the corresponding ionization energies are. Impurities with higher atomic number are not fully ionized in the fusion volume and thus provoke, besides bremsstrahlung radiation, strong radiation loss by line radiation in the

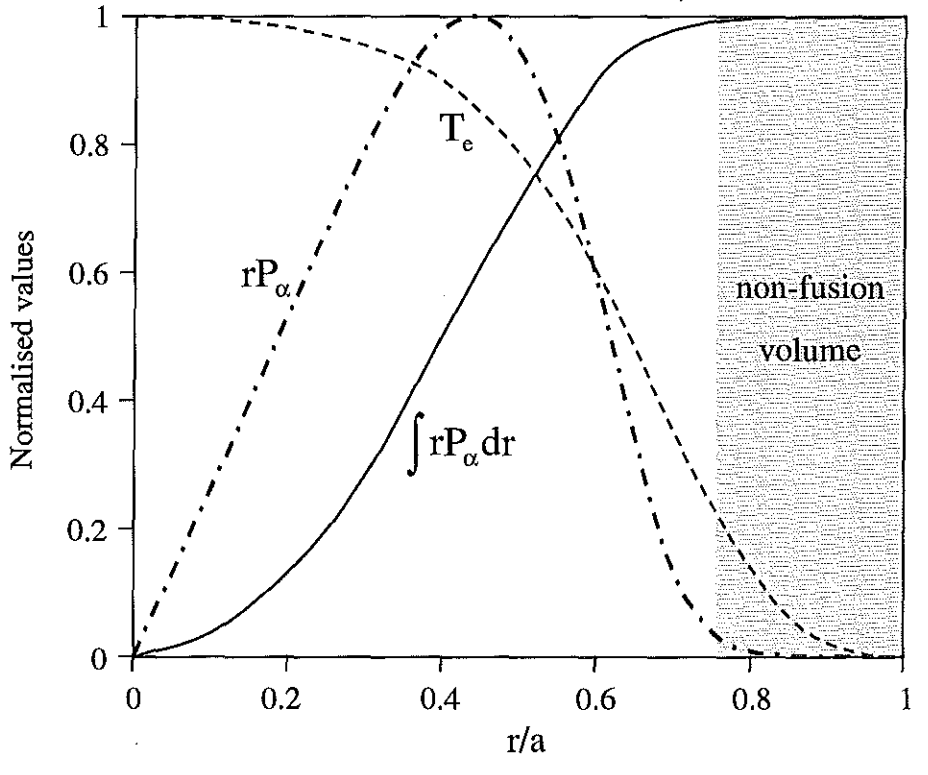

Figure 2-4 : Radial profiles of electron temperature (T_e), α-heating power density (P_α) and its integration expected in ITER.

plasma core region. Therefore high-Z atoms are not preferable for the radiation cooling. Accordingly low-Z impurities were considered and it is proved that *noble gases such as neon or argon fulfil the important limiting conditions*: **first**, the concentration of the impurities in the plasma edge should be stationary and controllable. **Second**, the concentration of the impurity in the plasma edge should be large enough to radiate the majority of heating power and to reduce the convective power load on the limiter or divertor.

In general, impurities seeded as neutral particles undergo dissociation or ionization by the electron impact. The characteristic time of the ionization can be written as $\tau_i = \frac{1}{n_e \langle \sigma_i v \rangle}$, where n_e is electron density and $\langle \sigma_i v \rangle$ is the rate coefficient for ionization. The excitation rate is given by:

$$\varphi_z^j = n_e n_z \langle \sigma_e v \rangle_z^j \tag{2-11}$$

where n_z is the local ion density of a given charge state z and $\langle \sigma_e v \rangle_z^j$ is the rate coefficient for the energy level j [Sam98]. The excitation of the particles is closely linked to the ionization since the excitation is restricted to the lifetime of the ion at the given ionization state (ionization time τ_i). The total number of excitations is the product of φ_z^j and τ_i. Then *the number of excitations per ionization* can be expressed with the given rate coefficients:

$$\alpha_z^j = \frac{\varphi_z^j \tau_i}{n_z} = \frac{\langle \sigma_e v \rangle_z^j}{\langle \sigma_i v \rangle}. \tag{2-12}$$

The rate coefficients decrease strongly with increasing T_e [Sob81,Jen77]. The power radiated from a given energy state can be obtained by multiplying α_z^j with the excitation energy from this energy state ΔE_z^j. The summation of this product over all energy levels and charge states of the impurity gives *the total energy radiated by line radiation during the life time of the impurity in the plasma*, which is called ***radiation potential*** (E_{rad}):

$$E_{rad} = \sum_z \xi_z \sum_j (\alpha_z^j \Delta E_z^j) \tag{2-13}$$

where ξ_z is the probability for a neutral particle to reach the charge state z. The total power radiated P_{rad} is then obtained by multiplying E_{rad} with the total flux of the impurity Γ_i entering the plasma:

$$P_{rad} = E_{rad} \Gamma_i . \tag{2-14}$$

E_{rad} can thus be determined by measuring P_{rad} [Rap96] and Γ_i. Fig. 2-5 shows the results of E_{rad} for various impurities as a function of T_e [Tok94]. It is apparent that E_{rad} and thus the cooling efficiency of neon is much larger than those of oxygen and carbon. Fig. 2-5 shows also clearly that ***E_{rad} increases significantly with decreasing T_e*** as a result of the temperature dependence of α_z^j. This is a very favourable characteristic, though this could also lead to instabilities [Sam98], since it is possible to obtain more radiation power at the same amount of impurities by decreasing T_e, i.e. n_e. The ***radiation level*** γ is defined as the ratio of the total radiation power P_{rad} to the total heating power P_{tot}. This is a useful parameter to characterise the efficiency of the radiation cooling and most of the phenomena in this work are expressed with this parameter.

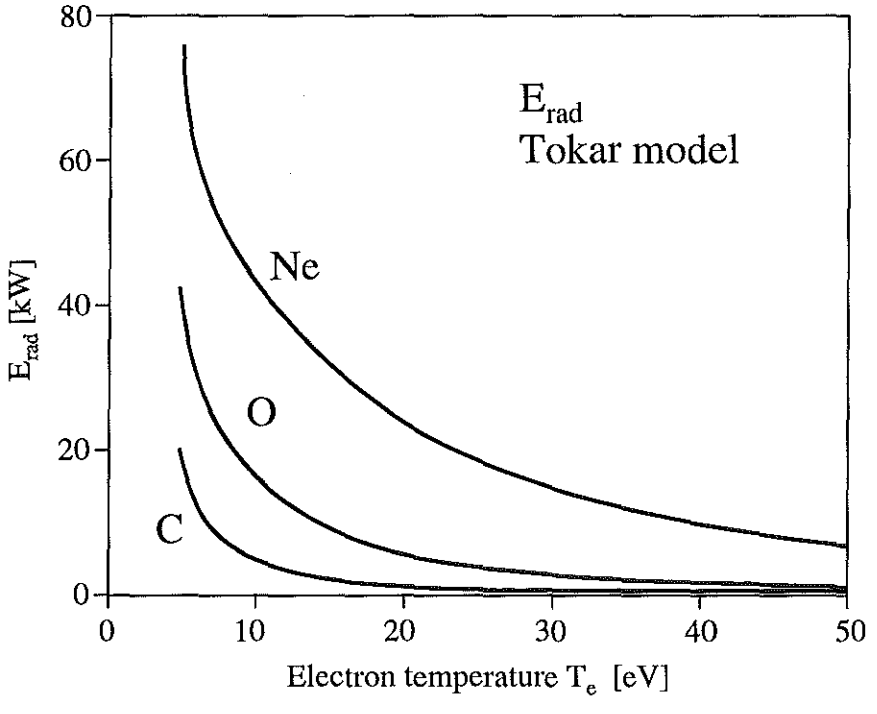

Figure 2-5 : Radiation power (E_{rad}) of neon, oxygen and carbon as a function of electron temperature (T_e) (calculated by Tokar et al. [Tok92]).

Fig. 2-6 shows the radial distribution of the neon concentration and its total radiation power for each ionization state obtained with model calculation of RITM [Unt95]. As shown in fig. 2-6(b) the total radiation power P_{rad} is indeed well restricted in the plasma edge (r ~ 0.4 m). It is remarkable that the contribution of Li- and Be-like ions (Ne^{7+}, Ne^{6+}) to P_{rad} is much higher than those of He- or H-like ions (Ne^{8+}, Ne^{9+}). Furthermore the envelope of the total radiation P_{rad} shows a sharp decrease when the Li- and Be-like ions decay. The radiations of He- or H-like ions are spread deep into the plasma centre. This is due to the jump of ionization energy from Li-like (Ne^{7+}, E_I = 239 eV) to He-like ion (Ne^{8+}, E_I = 1196 eV). For

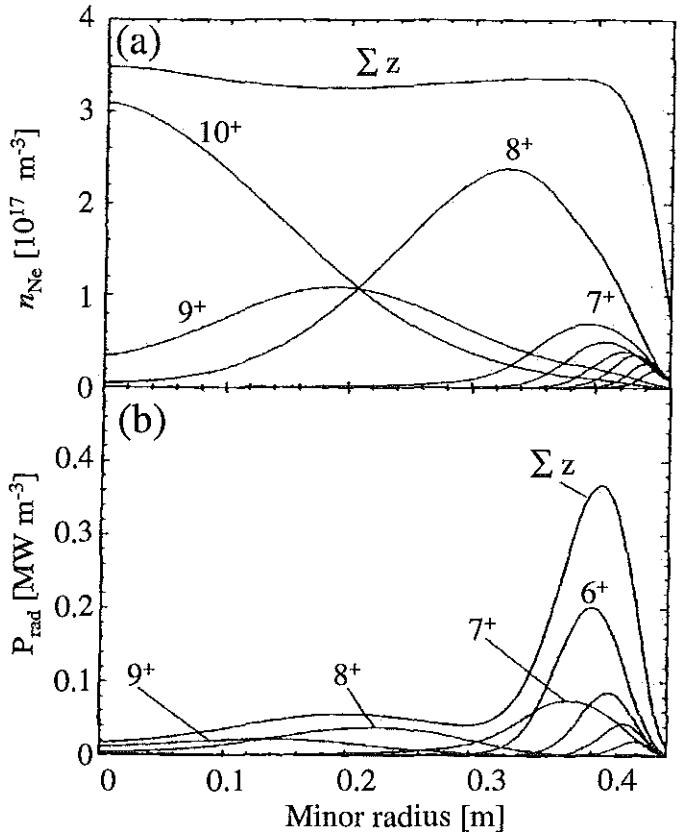

Figure 2-6 : Radial distribution of **(a)** the neon concentration and **(b)** its total radiation power for each ionization state calculated by the model calculation RITM. [Unt95]

this reason the intensity of the resonance line of the Li-like neon ion (Ne^{7+}, 2s-2p, λ = 77.4 nm) is chosen as the control signal of the neon content in the plasma.

3. Experimental Set-up of the Ion Beam Apparatus

3.1 Overview of the Ion Beam Experiment

For the irradiation and thermal desorption spectroscopy, an already existing ion beam apparatus was used. Mass separated ions with energies 2 - 10 keV were irradiated onto the graphite (EK98) target and the reemitted particles were measured by the partial pressure rise of the residual gas with a **Q**uadruple **M**ass **S**pectrometer (QMS). After the irradiation the amount of retained particles was determined by thermal desorption spectroscopy also with a QMS. Fig. 3-1 shows the set-up of ion beam apparatus. This apparatus is composed of three components: **1.** Ion source and bending magnet for the mass separation; **2.** Beam guiding system with differential pumping system, electrostatic Einzel-lens and x-y beam scanning system and **3.** The irradiation chamber with target module and QMS.

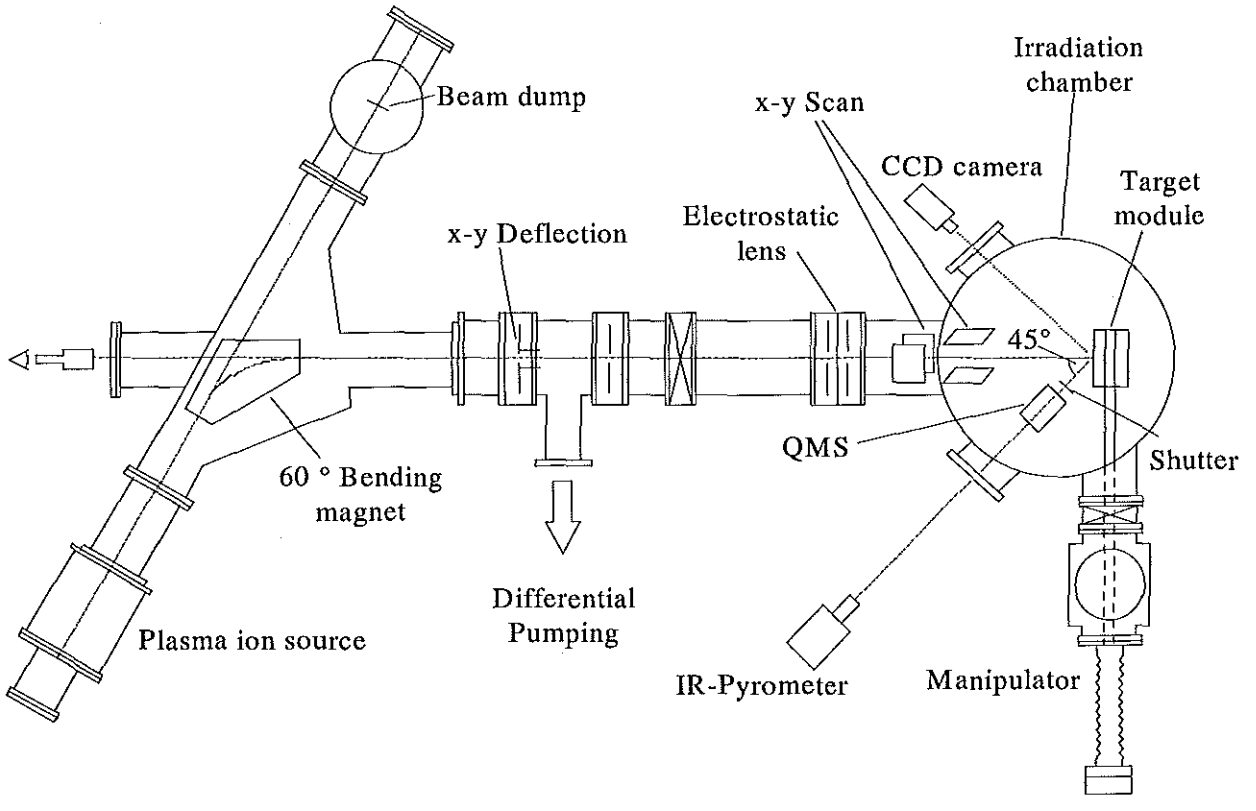

Figure 3-1 : Schematic diagram of the ion beam apparatus.

Since Refke [Ref94] has already described the main features of this apparatus in detail, we briefly describe the key features of it and the essential experimental procedures.

3.2 Experimental Facilities

3.2.1.1 Vacuum system

All the components of the ion beam apparatus are separately pumped by turbo molecular pumps backed by two-step mechanical pump (5 l/s). The resulting effective pumping speed is 180 l/s for the volume of the irradiation chamber (21.5 l). All the components can be separated by gate valves and pumped out without breaking the vacuum. With the help of a sample manipulator system the sample can be exchanged and driven into the irradiation chamber without breaking the vacuum. For the direct measurement of reaction product, one quadruple mass spectrometer is installed directly in the irradiation chamber without isolating valve. The pressure is monitored via Bayard-Alpert type ionization gauges (IE211, Leybold-Heraeus) and thermal conductivity gauges (TR250, Leybold-Heraeus). The maximum background pressure was ~ 1×10^{-6} Pa in irradiation chamber and ~1×10^{-5} Pa in ion source chamber.

3.2.2 Ion source and bending magnet

A plasma ion source (A-DIDA, Atomica) was used which can be operated with a hot cathode or as a cold cathode penning ion source. All the irradiations in this thesis were carried out in hot cathode mode. Ions could be accelerated up to ion energy of 15 keV. 2 keV was the minimum ion energy in this thesis with which the ion source can produce a reasonable ion beam current density. Four different gases can be supplied simultaneously.

For the generation of hydrogen ions, pressure, discharge current and magnetic field are important factors to decide the contribution of atomic and molecular ions [Val77].

The ion beam was mass- separated with a double-focusing 60° magnet sector field (Elektromagnet type EA2060, Drusch). The magnetic field can be varied continuously and has a mass resolution of $m/\Delta m \sim 50$ so that the mass separation with $\Delta m = 1$ for the mass range of up to $m = 50$ was possible. Before the ion beam is mass filtered, the unselected ion beam is optimised by a collector in the beam dump (see fig. 3-1). The optimisation conditions for each gas species and energy are very reproducible and the typical ion current of neon with 10 keV reaches up to 15 μA at the beam dump.

3.2.3 ***Beam guiding system***

3.2.3.1 Differential pumping

The usual working pressures in the ion source (p_I) was ~ 10^{-3} Pa and the background pressure in the irradiation chamber (p_R) was ~ 10^{-6} Pa. By differentially pumping the two chambers ($S_{dp,eff}$ ~ 180 l/s), it was possible to prevent an effect of p_I on p_R and also to reduce the neutralisation of the ions by charge exchange collision. Fig. 3-2 shows the differential pumping system schematically. As already mentioned by Refke [Ref94], from the geometry one can calculate the pressure rise in irradiation chamber with the given pressure in the ion source as follow:

$$\Delta p_R = \frac{p_I \cdot L^2}{S_{dp,eff} \cdot S_{R,eff}}. \qquad (3\text{-}1)$$

In our system the typical working pressure in ion source chamber ($p_I = 3\times10^{-3}$ Pa) results in the pressure rise of 5×10^{-10} Pa, which is, in comparison to the typical background pressure of irradiation chamber p_R = ~ 10^{-6} Pa, negligible. It was also experimentally shown that p_R is practically independent of the change of p_I.

Besides differential pumping, as shown in fig. 3-2, the system defines the axes of the ion beam. By measuring the ion beam on the first plate in front of the first sectorial aperture, one

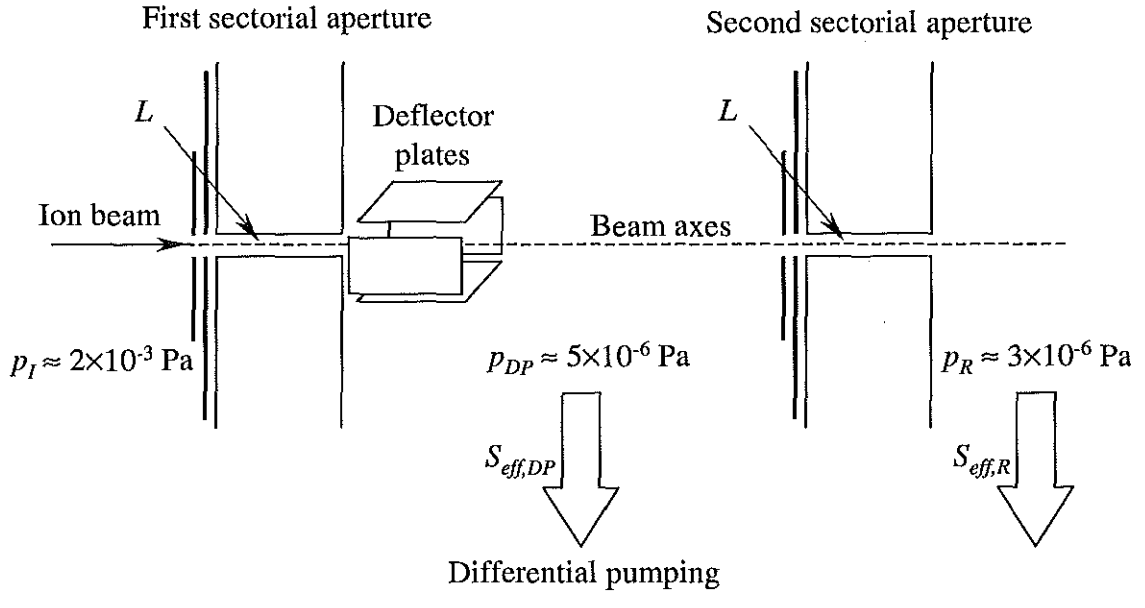

Figure 3-2 : Schematic diagram of the differential pumping system between ion source and irradiation chamber.

can optimise the ion source setting and the mass separation. Two sets of deflector plates (10×30 mm^2, d = 14 cm) behind the first sectorial aperture, by measuring the ion beam on the second plate in front of the second sectorial aperture, allow to adjust the ion beam through the second sectorial aperture. The deflecting voltage can be varied ± 500 V for each plate sets so that both positive and negative ion can be deflected. With ion energy 6 keV the maximum deflection on the second sectorial aperture was ~ 10 mm [Ref94]. By applying the maximum voltage at the deflector plates, it was possible to turn on and off the irradiation of the target without turning off the ion source or bending magnet.

3.2.3.2 Electrostatic Einzel-lens and beam scanning system

The ion beam through the second sectorial aperture (ϕ = 2.5 mm) is, on its way to the 540 mm distant target, expanded by its divergence. It is experimentally shown that the 6 keV O_2^+ beam has it diameter of 5.6 mm at the target [Ref94], which is larger than the width of the target (3 mm). In order to focus the ion beam smaller than 3 mm, a set of electrostatic einzel-lens was installed, whose detailed description is given by Refke [Ref94]. In order to minimise the spherical aberration, the lens was installed at the possible nearest position from the target (~ 180 mm) [Wil73]. For the present configuration, the minimum beam sizes on the target of only 3×3 mm^2 for Ne^+ 10 keV and 3×5 mm^2 for Ar^+ 10 keV were obtained, which is presumably considered to be due to the aged Ni-grid in the second sectorial aperture. The ion beams beyond the target width are impinged onto the stainless steel target holder and causes a exaggeration in current measurement. The correction of this effect will be described in the following section.

In order to irradiate the target homogeneously, the ion beam was scanned in x- and y-direction after the focusing lens. The scanning system is composed of two sets of electrodes for x- and y-direction scanning and an aperture with a diameter of 9 mm. For the deflection sawtooth voltage was used and in order to prevent an inhomogeneous irradiation, e.g. Lissajous figure, most different deflecting frequencies were chosen (ν_x = 300 Hz, ν_y = 1 Hz). For the neon irradiation the minimum scanned beam area was 3×3 mm^2. For argon however, especially for 10 keV irradiation, the deflecting voltage was not sufficient and the minimum area was 3×5 mm^2.

3.2.4 Set-up of measuring instruments

3.2.4.1 Target manipulator

The target samples with a dimension of 3×35×0.2 mm^3, made of *fine grain isotropic graphite* (EK98: isotropic fine grain graphite, ρ = 1.86 g/cm^3, Ringsdorff) which is used as a

standard limiter material in TEXTOR, are mounted on a continuously rotatable target holder. Maximum 10 samples can be mounted and simply by rotating the holder different samples can be successively irradiated under same irradiating condition. One target position was occupied by a copper stripe for the measurement of the ion current. In order to visualize the incident ion beam, another target position was occupied by a aluminium stripe coated with fluorescent film. Each sample has a common end with a ground potential and can be heated separately during the irradiation. The target module can be driven into and withdrawn from the irradiation chamber, with a precision of < 0.3 mm in x-direction, via a manipulator system. The adjustment of the sample positions was done by an alignment telescope on the beam axes and a CCD camera 45° from the beam axes (see fig. 3-1). With a help of a target exchange chamber beside the irradiation chamber it was possible to exchange the samples without breaking the vacuum of the irradiation chamber.

3.2.4.2 Ion current and beam profile measurement

In measuring the ion current it was impossible to use the conventional Faraday cup due to the geometrical reason. The ion current incident onto the target was measured directly via the voltage drop of 1 MΩ resistance. In the measurement of the ion current, two possible error sources were corrected: 1. Secondary Electron Emission and 2. The contribution of the current from the target holder especially for 10 keV Ar^+ irradiation. Secondary electron emission is caused by highly energetic incident ions. In this experiment the Secondary Emission Coefficient ($C_{SE} = \frac{I_{SE}}{I_{ion+SE}}$) were measured by biasing the target up to +100 V during irradiation, which was then subtracted from the measured ion current. Table 3-1 lists the measured C_{SE}. They are relatively constant for the given ion energy and ion species.

Ion Species	2 keV	3 keV	5 keV	10 keV
Ne	0.25		0.30	0.35
Ar		0.10	0.19	0.25
D_2			0.31	

Table 3-1 : Measured Secondary Emission Coefficient (C_{SE}) for Ne, Ar and D_2 of various ion energy.

In order to measure the horizontal and vertical beam profile, a target with one end open was used. As mentioned in the previous section, the minimum beam size on the target was 3×3 mm² for Ne^+ (10 keV) and 3×5 mm² for Ar^+ (10 keV) respectively. For the case of energetic argon irradiation the contribution of ion beams impinging onto the stainless steel

target holder was corrected, which amounts to ~ 50 % of measured current for 10 keV Ar^+. For smaller energies of argon and other ion species however no such a correction was needed.

3.2.4.3 Target heating and temperature measurement

Each target can be heated separately up to 2000 K by DC current ramping. During the irradiation a constant target temperature can be maintained. Experiments show that a constant target temperature of 1000 K can be maintained for several minutes without causing a significant rise of the background [Ref94]. For the thermal desorption spectroscopy the heating voltage was given by a ramp generator, with which the target could be heated up to 2000 K with a quasi-linear temperature rise between 700 and 1600 K. Most thermal desorptions were carried out with a heating rate of 11.5 K/s. The target temperature was monitored via a infrared spectral pyrometer (TMR95-d, Maurer) with a measurement range of 473 K – 1773 K in spectral range of 1.0 – 2.6 μm. The pyrometer, mounted 45° from the beam axes, observes just the irradiation point of the target through the cross beam ion source of QMS (see fig. 3-1). For the calibration of the pyrometer the target temperature was measured simultaneously by a filament optical pyrometer (Nr.3534, Mikro-Werk) between 1000 and 1500 K.

3.2.4.4 Quadruple mass spectrometer (QMS) and its calibration

For the investigation of the reaction product of the irradiation and the thermal desorption a **Q**uadruple **M**ass **S**pectrometer (QMG311, Balzers) was used. The QMS is equipped with a "cross-beam" ion source, quadruple mass filter and a Secondary Electron Multiplier (SEM) mounted 90° with respect to the mass filter axes. The QMS signals were registered by a computer controlled data acquisition program (Quadstar 4.20, provided by the manufacturer). Other signals (ion current, pressures of irradiation chamber and calibration chamber, and the target temperature) were monitored simultaneously by a personal computer. The QMS was positioned at 45° rotated with respect to the beam axes so that the direct measurement of the neutral particles and secondary ions emitted from the target (SIMS) was possible without wall contact. The target could be shielded with a screen, in order to distinguish the signal from the residual gas and that directly emitted from the target.

In this thesis signals only in the residual gas were measured. QMS measures only the particles that are not stuck on the inner wall of vacuum chamber. Due to the collision with the wall these particles are thermalized and have a Maxwellian energy distribution with the wall temperature (room temperature). In this case the change of ion current of a gas species measured by QMS (ΔI_R) is exactly proportional to the change of the corresponding partial pressure (Δp_R), which is again proportional to the particle flux (Φ_i) from the source chamber. In order to calibrate the measured signal, a special gas inlet system was used. The calibration

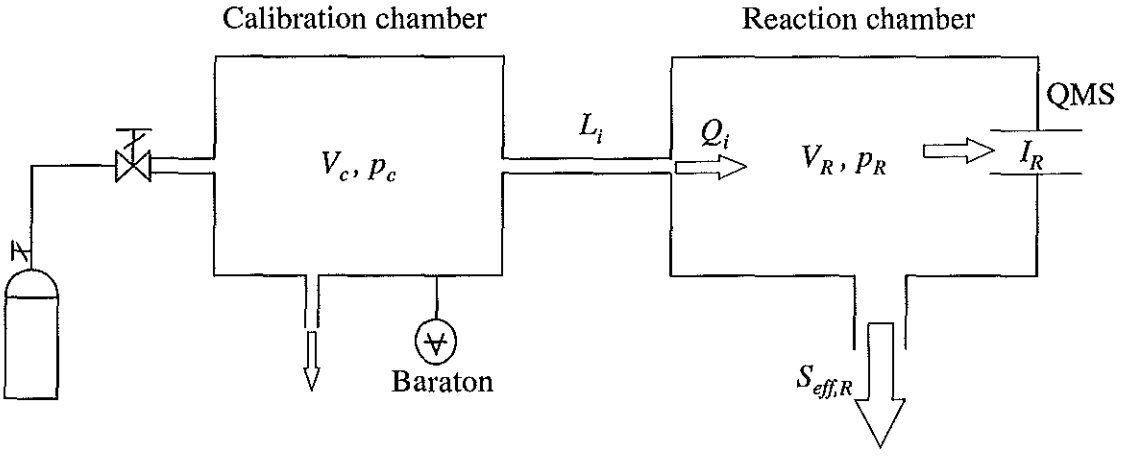

Figure 3-3 : Schematic diagram of gas inlet system for the calibration of QMS.

gas was puffed via a leak valve into the calibration chamber with a volume of 0.287 l and flows into the irradiation chamber through a small leak with a known geometry (diameter: 0.2 mm, length 2 m). The pressure in the calibration chamber (p_c) was measured by a capacitance diaphragm gauge (Baraton 223B, MKS) in the range of 10^{-1} – 100 Pa. Fig. 3-3 shows the calibration of QMS signal schematically.

Here we want to calculate the calibration factor ($\varepsilon_i = \frac{\Phi_i}{I_R}$) of QMS. From the ideal gas law and from the definition of the gas flow one can write as following:

$$pV = NkT \tag{3-2}$$

$$Q_i = V\frac{dp}{dt}. \tag{3-3}$$

From the fact that $Q_i = L_i(p_c - p_R) \approx L_i p_c$ and by differentiating Eq. 3-2,

$$V\frac{dp}{dt} = \frac{dN}{dt}kT = L_i p_c. \tag{3-4}$$

Then one can derive the calibration factor of ($\varepsilon_i = \frac{\Phi_i}{I_R}$):

$$\Phi_i = \frac{dN}{dt} = \frac{L_i p_c}{kT} \equiv \varepsilon_i I_R \tag{3-5}$$

where $\frac{1}{kT} = \frac{1}{1.38\times10^{-22}T(K)}$. L_i can be calculated from the known formula of a tube with circular cross section ($L = 12.1 \cdot \frac{d^3}{l}$) [Ede86]: L_{D_2} = 1.30×10^{-3} l/s, L_{Ne} = 5.83×10^{-4} l/s, L_{Ar} = 4.12×10^{-4} l/s. From the pressure drop of the vacuum system one can also measure the conductance L_i (L_{D_2} = 1.28×10^{-3} l/s, L_{Ne} = 5.97×10^{-4} l/s, L_{Ar} = 4.09×10^{-4} l/s). The values show a good agreement with the calculated ones.

4. Results of the Ion Beam Experiments

The ion beam apparatus is used to study the reemission and retention behaviour of energetic neon and argon ions in graphite. The graphite samples were irradiated by rastering the ion beam over an area of 3×3 mm^2 with an averaged flux density between ~ 10^{16} $m^{-2}s^{-1}$ at 2 keV and ~ 10^{18} $m^{-2}s^{-1}$ at 10 keV ion energy. The reemitted or desorbed neon and argon were measured by residual gas analysis.

4.1 Neon Ion Implantation into Graphite

4.1.1 Fluence dependence

Fig. 4-1 shows the typical reemission of neon (measured as mass 20) during the irradiation of graphite (EK98) with monoenergetic 2 keV neon ions as a function of incident neon fluence. In the very beginning of the irradiation the reemission yield is small. Nearly all implanted neon is retained in the sample. The reemission rises with increasing incident fluence and is saturated to unity after a certain fluence (~ 1×10^{20} m^{-2}), that means all the incident neon is reemitted simultaneously. As expected, the implanted neon reemits as atom.

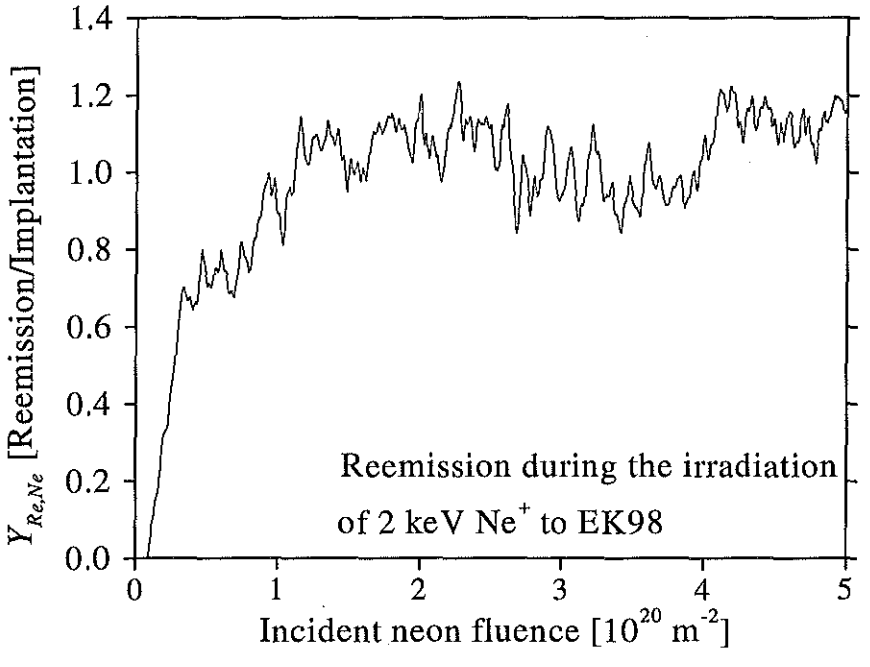

Figure 4-1 : Typical reemission spectra of neon during the irradiation of graphite with 2 keV Ne^+ at room temperature.

The retained neon in the graphite was measured by **T**hermal **D**esorption **S**pectroscopy (TDS) after the irradiation. The graphite sample was heated up to 2000 K with a linear DC current (ramp rate 11.5 K/s, see 3.2.4.3). Fig. 4-2 shows the thermal desorption spectrum of neon irradiated by 10 keV of different fluences at room temperature. As shown, the temperature of maximum desorption spectra (T_p ~ 780 K) is independent to the incident fluence. As will be discussed later on, the desorption of neon can be described as a nearly first order one [Gum90]. From the maximum temperature of the desorption spectra the binding energy for neon in graphite (E_b) of 2.06 eV is determined.

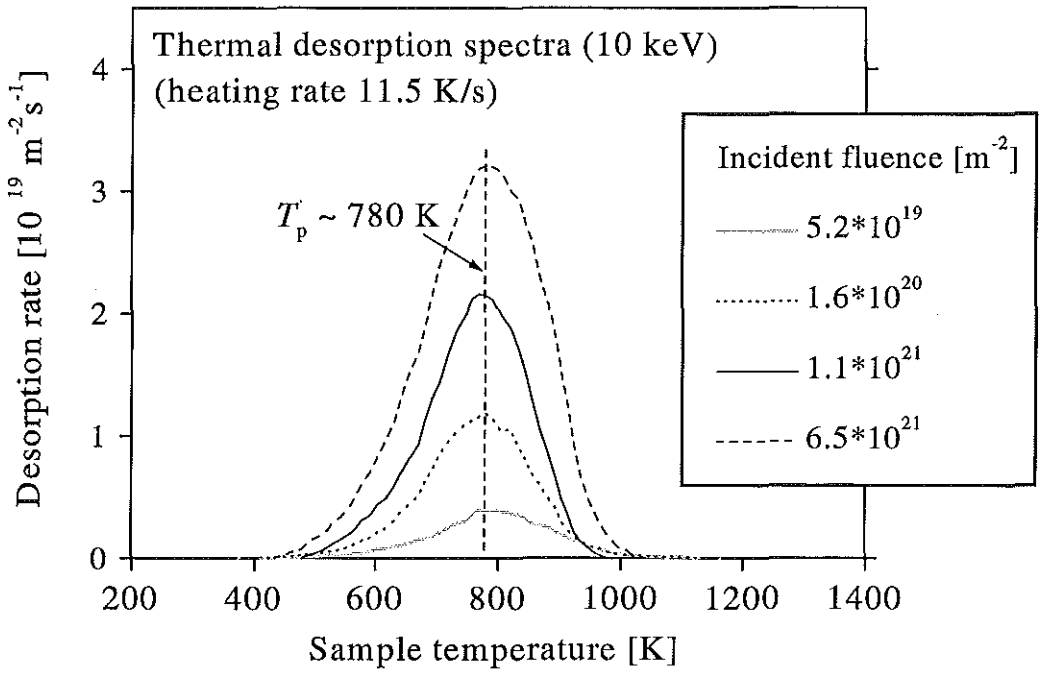

Figure 4-2 : Desorption spectra after the irradiation of graphite with 10 keV neon of different fluences.

4.1.2 Ion energy dependence

Fig. 4-3 shows the reemission yield of neon ($Y_{Re,Ne}$) from graphite (EK98) as a function of the incident fluence for different ion energies (2, 5, 10 keV). In the transient phase of irradiation the reemission yield $Y_{Re,Ne}$ by implantation of higher neon ion energy is smaller than that of lower energy and the saturation fluence of higher energy is greater than that of lower energy. This is mainly due to the effect that the implantation range (R_p) of ions increases with increasing ion energy. As discussed in 2.1.1.1, the implantation range can be calculated by Monte Carlo code calculations TRIM: 5.7, 12, 21 nm for 2, 5, 10 keV Ne^+ in graphite respectively.

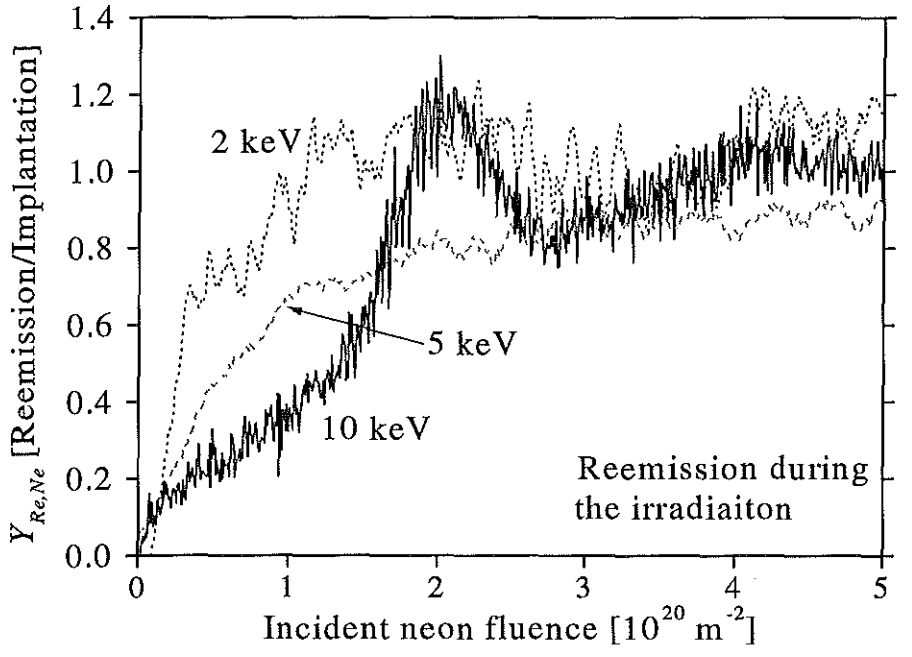

Figure 4-3 : Reemission spectra of neon during the irradiation graphite with different ion energies of 2, 5, 10 keV at room temperature.

In the reemission spectra of the irradiation with 10 keV Ne^+ a hump appears at the fluence of ~ 2×10^{20} m^{-2}, which is reproducible and found only for this energy. Possible explanation for it will be discussed later on.

The thermal desorption spectra of neon desorbed from graphite irradiated at different ion energies have a similar maximum temperature of the desorption spectra (~ 780 K). The amount of desorbed neon increases with increasing neon energy. As shown in fig. 4-4, however, the increase of retention density with increasing energy is very small or practically none. This is already expected from the reemission spectra and also reported by other authors [Cho93]: in the low energy range (< 100 eV) the saturation retention density of neon and argon increases with increasing ion energy but is saturated over several hundred eV of ion energy. This retention characteristic is significantly different from those of deuterium or oxygen in graphite whose saturation retention density increases with increasing ion energy [Ref94,Doy80].

In order to cross-check the amount of retained neon in graphite, graphite samples irradiated with 2, 5, 10 keV Ne^+ are investigated by **R**utherford **B**ack **S**cattering (RBS) measurement [Rub96]. The results are shown in fig. 4-4 and relatively in good agreement with those by thermal desorption except the one with 2 keV.

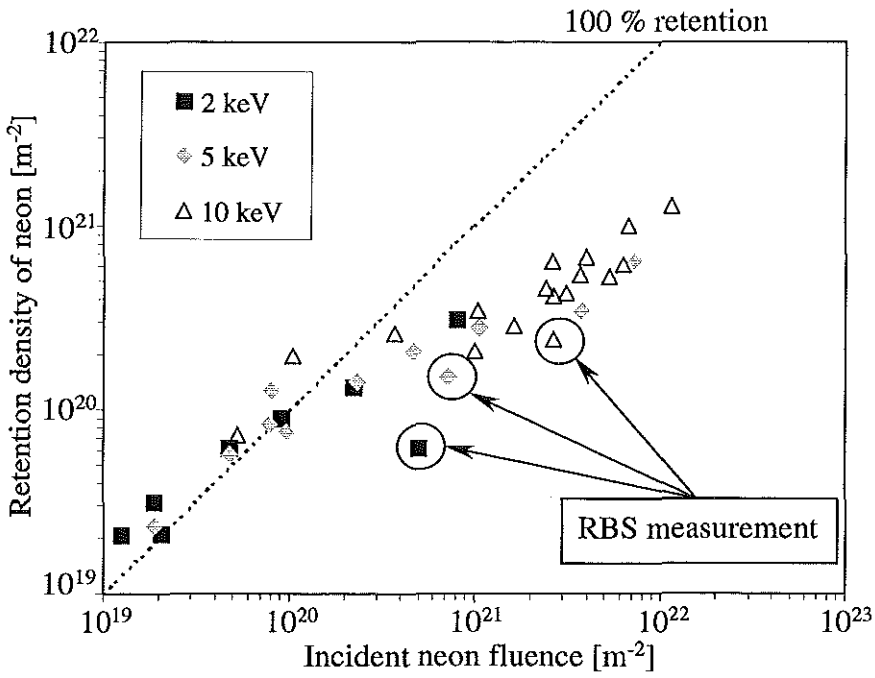

Figure 4-4 : Retention density of neon in graphite at room temperature for different incident neon energy and comparison of those measured by RBS (in circle).

Granting that the depth distribution of neon in graphite is homogeneous within the implantation range, one can calculate the saturation concentration of neon in graphite (Ne/C) with the implantation range (R_{Ne}) and the known concentration of graphite (ρ_{EK98} = $9.3\times10^{19}m^{-2}nm^{-1}$) [Wam81]. Tab. 4-1 lists the calculated saturation concentrations of neon in graphite for each ion energy, the mean implantation ranges (R_p) and standard deviations (σ) of Gaussian distribution calculated by TRIM (see 2.1.1.1). In this calculation the same saturation retention density (4×10^{20} m^{-2}) is taken, which is reasonable as shown in fig. 4-3. For 10 keV ion energy the saturation concentration Ne/C is about 0.15, which is smaller than that of deuterium (D/C ~ 0.44 [Wam81]) and oxygen (O/C ~ 0.2 [Ref94]). What is here to note is

Ion energy [keV]	R_p [nm]	σ [nm]	Ne/C
2	5.7	2.1	0.55
5	12	4.3	0.27
10	21	7.5	0.15

Table 4-1 : The saturation concentration of neon in graphite (Ne/C) for the incident ion energy of 2, 5, 10 keV (R_p: mean implantation range, σ : standard deviation of implantation range for Gaussian distribution).

that Ne/C decreases with increasing ion energy, which is different from O/C measured by Refke [Ref94]. This also implies that neon has a different retention mechanism from that of oxygen or hydrogen.

4.1.3 Sample temperature dependence

In order to investigate the dependence of the reemission and retention characteristic of neon on the sample temperature, the sample temperature during the irradiation was varied from room temperature up to ~1200 K. Fig. 4-5(a) shows the reemission yield of neon from the graphite with different sample temperature during the irradiation. Observing the early phase of irradiation, the reemission yield of neon $Y_{Re,Ne}$ increases with increasing sample temperature. Taking into account that the thermal desorption of neon begins at the sample

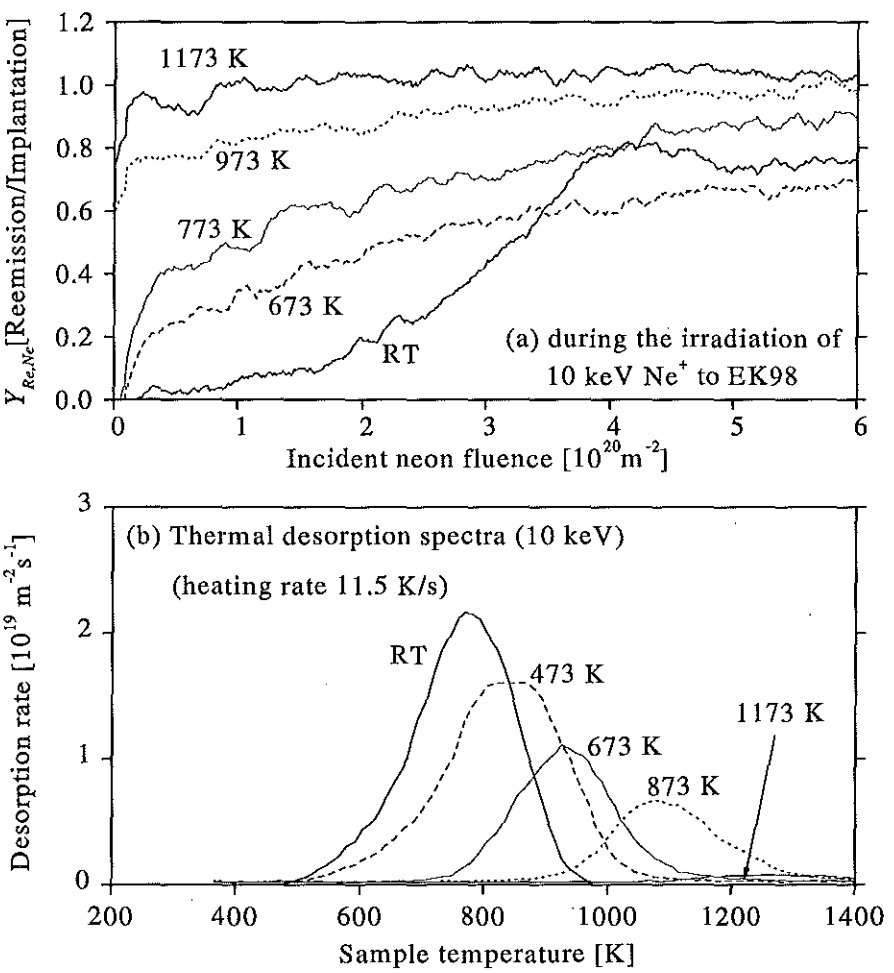

Figure 4-5 : Sample (EK98) temperature dependence of **(a)** reemission spectra of neon during the irradiation with 10 keV ion energy and **(b)** desorption spectra after the irradiation with the incident fluence of 1×10^{21} m^{-2}.

temperature of ~ 400 K, it is logical that the neon incident onto the sample at temperatures over 400 K releases partly simultaneously during the irradiation. At a sample temperature of ~ 1200 K the reemission yield reaches immediately unity after the onset of the irradiation, implying no retention of neon at this temperature. After the saturation fluence the reemission yields $Y_{Re,Ne}$ at all measured temperatures are saturated to unity and no further increase is observed even at higher temperature. This is a good evidence that neon does not diffuse into the bulk of graphite even at higher temperature, which will be further discussed in the following section.

Fig. 4-5(b) shows the desorption spectra of neon after the irradiation of 10 keV neon with the same fluence (1×10^{21} m^{-2}), up to saturation, at different sample temperatures. As expected from the reemission spectra, the amount of desorbed neon decreases with increasing sample temperature and at ~ 1200 K there is practically no desorption. The shift of the maximum temperature toward higher temperatures can be understood since the neon atoms, which can be captured at the temperature lower than the sample temperature during the irradiation, are already released during the irradiation. The result of it is the shift of the desorption spectra, i.e. the increase of the average binding energy. What we should here note however is that the envelope of the desorption spectra with increasing sample temperature is shifted beyond that of lower sample temperature. If the retention mechanism of neon at higher temperature is the same as that at lower temperature, all the envelopes at higher temperature should be placed within that at room temperature. It is not yet understood and one can only speculate that the structure of defects formed by energetic incident neon at higher temperature is different from that formed at lower temperature, which should be further investigated.

4.1.4 Investigation of ion induced release and diffusion of neon

Neon is only a minority component in the TEXTOR plasma. The majority of them (over 90 %) are hydrogen or deuterium ions. Thus, if we want to compare the neon retention in graphite in ion beam experiments with that in a TEXTOR plasma, we have to be aware that the irradiation in the TEXTOR plasma occurs always with the simultaneous irradiation of the majority of hydrogen/deuterium ions. The effect of simultaneously incident hydrogen on the retention of neon in graphite is already investigated by Brosset et al. [Bro97] with a DC-plasma. It has been observed that the retention of neon decreases significantly under a simultaneous impact of hydrogen ions. This behaviour is interpreted by the so called *'ion induced release of implanted atoms'* [WinB74], in which the atoms retained within the several monolayers of the bulk are released by incident ions. It is therefore expected that the simultaneous impact of hydrogen influences the retention of neon in graphite in fusion devices. In order to simulate this effect with the available ion beam apparatus; a graphite sample was first irradiated with 10 keV neon, followed by an irradiation with 5 keV molecular deuterium ion (D_2^+). The ratio of these ion energies are similar to the typical

energies of neon and atomic deuterium plasma ions impinging on the graphite target in TEXTOR (E_{Ne}^{5+} ~ 800 eV and E_D^+ ~ 200 eV). Unfortunately, a simultaneous irradiation was not possible in our ion beam apparatus.

Fig. 4-6 shows that the retention densities of neon in graphite after the irradiations of 10 keV Ne^+ followed by 5 keV D_2^+ (▲) with the same irradiation fluences are exactly the same as those after the irradiations with 10 keV neon alone (△). An 'ion-induced release of neon' in this way of ion exposure is not observed. In order to understand this discrepancy, we suggest several explanations: **first**, the energies of neon and deuterium were too high. The ion induced release was observed within the some monolayers of bulk atoms (graphite monolayer is 0.3 nm) [Del79], the implantation range of neon is far larger than that (21 nm for 10 keV Ne^+). The possibility that the neon released deep in the graphite bulk find another sink on its way out, is quite high. **Second**, the incident fluence of deuterium was too low in comparison to that of neon. Taking into account that the incident fluence of hydrogen in the plasma edge of TEXTOR is more than one order of magnitude greater than that of neon, the incident fluence of deuterium should be much larger. It was however technically very difficult to keep the small current of deuterium (several hundred nA) up to 10 hours, due to the change of various parameters (e.g. pressure in ion source chamber).

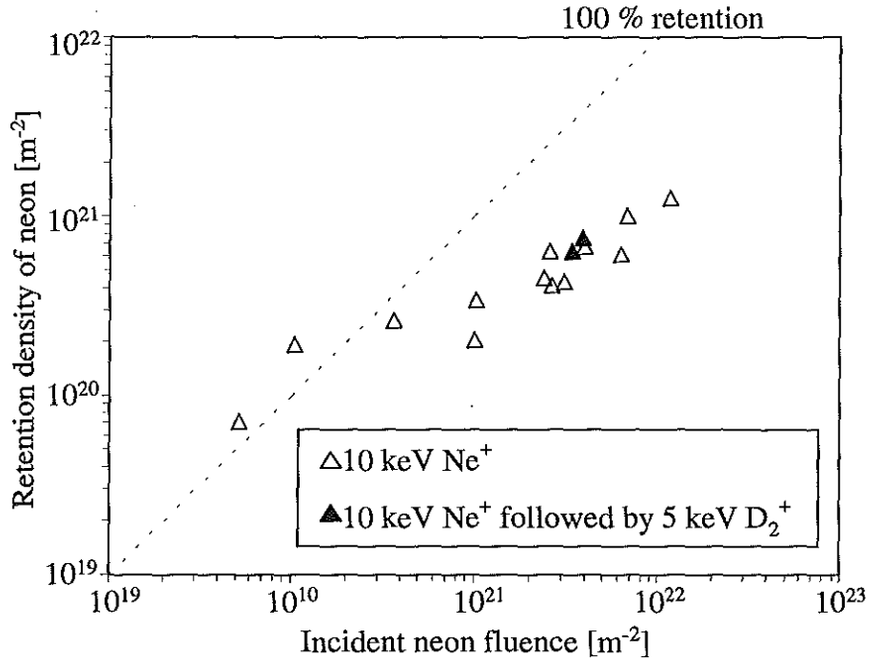

Figure 4-6 : Comparison of the retention density of neon in graphite (△: only after 10 keV neon irradiation, ▲ : after 10 keV Ne^+ irradiation and 5 keV D_2^+ irradiation).

It is also an interesting question whether there is a diffusion of neon into the graphite bulk. In order to investigate it, two trial experiments were carried out: **first**, the irradiation was stopped above the saturation fluence and was started again after one hour. The amount of reemitted neon shows exactly the same value as before. **Second**, after the irradiated sample was left 15 hours in the UHV chamber, thermal desorption was carried out. The desorption spectra and the amount of desorbed neon were exactly identical to those done immediately after the irradiation. These two experiments suggest that there is no diffusion of neon in graphite in this time period at room temperature. The same conclusion can be drawn from the RBS results (see fig. 4-3). These samples were transported at atmospheric pressure to Stockholm and investigated two weeks after the irradiations.

4.2 Argon Ion Implantation into Graphite

4.2.1 Fluence dependence for different incident ion energies

Fig. 4-7 shows the reemission yield spectra of argon ($Y_{Re,Ar}$) from graphite (EK98) as a function of the incident argon fluence for different argon ion energies (3, 5, 10 keV). As was the case of neon, the reemission of argon increases and is saturated with increasing incident argon fluence. In the early phase of irradiation the reemission yield $Y_{Re,Ar}$ at higher impact energy is smaller than that at lower energy. In comparison to neon, the saturation fluence of argon (2×10^{20} m^{-2} for 10 keV argon) is smaller than that of neon for the same energy (4×10^{20} m^{-2} for 10 keV neon), partly due to the smaller implantation depth and partly due to a smaller argon retention in graphite as will be shown below.

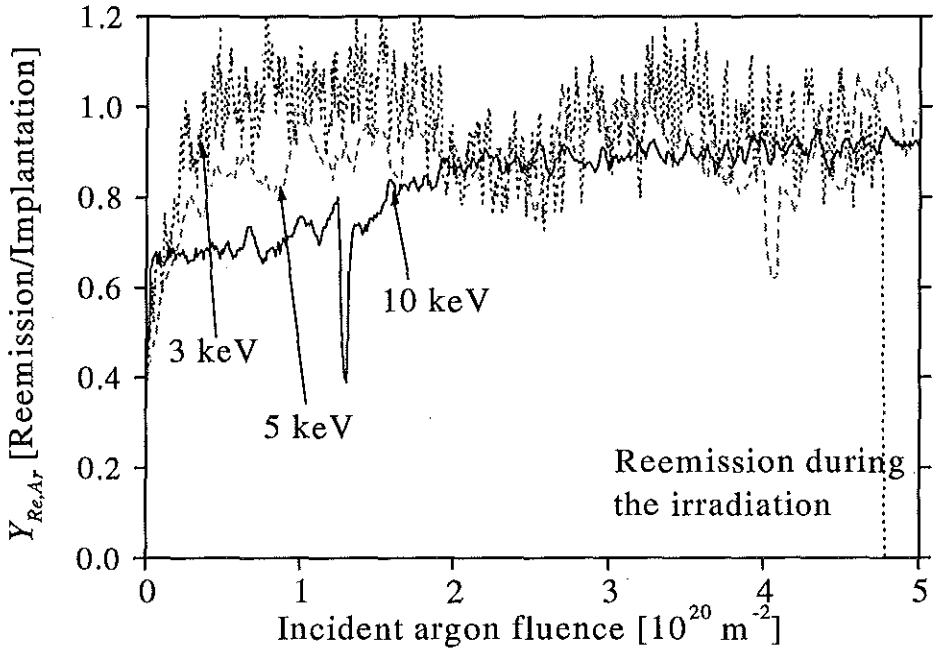

Figure 4-7 : Reemission spectra of argon during the irradiation of graphite with different argon ion energy (3, 5, 10 keV).

The amount of retained argon during the irradiation is again investigated by thermal desorption spectroscopy after the irradiation. The graphite sample was heated up to 2000 K with a linear DC current (ramp rate 9.5 K/s) and the retained argon was released in form of an argon atom. Fig. 4-8 shows the thermal desorption spectra of retained argon irradiated by 10 keV argon with various incident argon fluences at room temperature. The desorption spectrum of argon is broader and the temperature of maximum spectra (850 K, with heating

rate 9.5 K/s) is higher than that of neon (780 K, with heating rate 11.5 K/s). The temperature of the maximum desorption does not depend on the incident ion energy and the fluence. The desorption spectrum of argon is also somewhat asymmetric to the peak temperature. From this it is indicated that the desorption of argon is a first order procedure (see 2.1.1.6). From the maximum temperature one can calculate the binding energy of argon in graphite (E_b) of 2.35 eV, which is somewhat larger than that of neon.

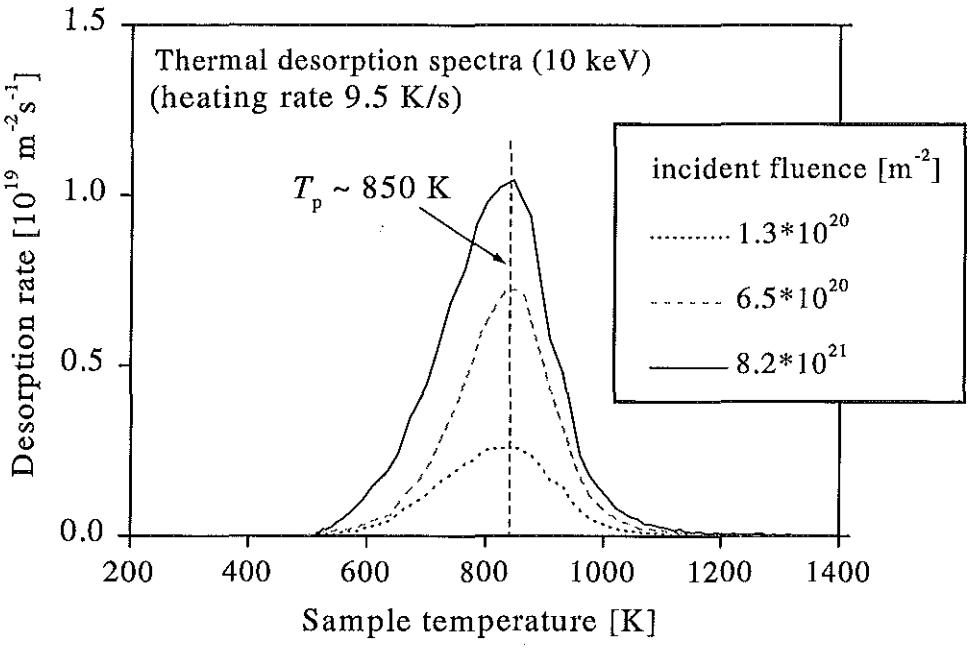

Figure 4-8 : Desorption spectra after the irradiation of graphite (10 keV Ar^+) with different incident fluence.

The amount of desorbed argon increases with increasing fluence, which can be better seen in fig. 4-9. After a certain fluence the retention is saturated or increases with a smaller slope. In comparison to the retention density of neon, the retention of argon is smaller and never reaches 100 % even at a small fluence, which is also in good agreement with other measurements [Cho93]. As for neon one can calculated the saturation concentration of argon in graphite with the concentration of graphite (ρ_{EK98} =9.3x10^{19} m^{-2}nm^{-1}). Table 4-2 lists the saturation concentrations of argon in graphite for different incident ion energies. For 10 keV ion energy the ratio of argon to carbon (Ar/C) reaches about ~ 0.08, which is much smaller than that of neon (Ne/C ~ 0.15 [Wam81]). As for the neon case, the increase of the ratio of argon to carbon (Ar/C) with decreasing ion energy shows that also argon is retained more densely at lower impact energy than with higher energy.

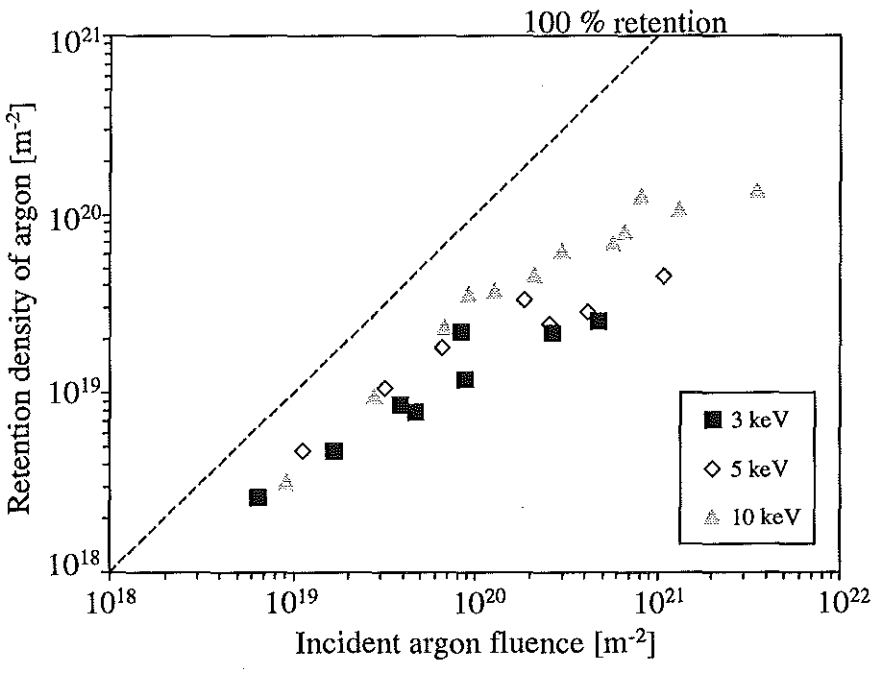

Figure 4-9 : Retention density of argon in graphite at room temperature for different incident argon energy.

Ion energy [keV]	R_p [nm]	σ [nm]	Ar/C
3	4.6	1.3	0.18
5	8.4	2.5	0.10
10	14	4.2	0.08

Table 4- 2 : The saturation concentration of argon (Ar/C) in graphite (EK98) for the incident ion energy of 3, 5, 10 keV (R_p: mean implantation range, σ: standard deviation of implantation range for Gaussian distribution).

4.2.2 Sample temperature dependency

The dependence of the reemission and retention characteristics of argon on the sample temperature was also investigated: the sample temperature during the irradiation was varied from room temperature up to 1200 K. Fig. 4-10(a) shows the reemission yield spectra of argon from the graphite at different sample temperatures during the irradiation. Most observations are similar to those of neon. In the early phase of irradiation, the reemission yield of argon $Y_{Re,Ar}$ increases with increasing sample temperature. At a sample temperature of 1200 K the reemission yield reaches immediately unity (within the accuracy of our calibration) after the onset of the irradiation, implying no retention of argon at this

temperature. For all measured sample temperatures the reemission yields $Y_{Re,Ar}$ are saturated to unity after a certain fluence and no further increase is observed even at higher temperature.

Fig. 4-10(b) shows the desorption spectra of argon after the irradiation of 10 keV Ar^+ with similar irradiation fluence up to saturation (5×10^{20} m^{-2}: about half of that at neon irradiation in fig. 4-5(b)) at different sample temperatures. The overall dependence of desorption spectra on the sample temperature is also similar to that of neon: With increasing sample temperature the amount of desorbed argon decreases and the maximum temperature is shifted toward higher temperature. With increasing sample temperature the shift of the spectrum envelope beyond that at lower energy is also observed. Further is remarkable that the amount of desorbed argon at 800 K is larger than that at 600 K. This is, from more than 10 measurements, reproducible but the reason for that is not yet understood.

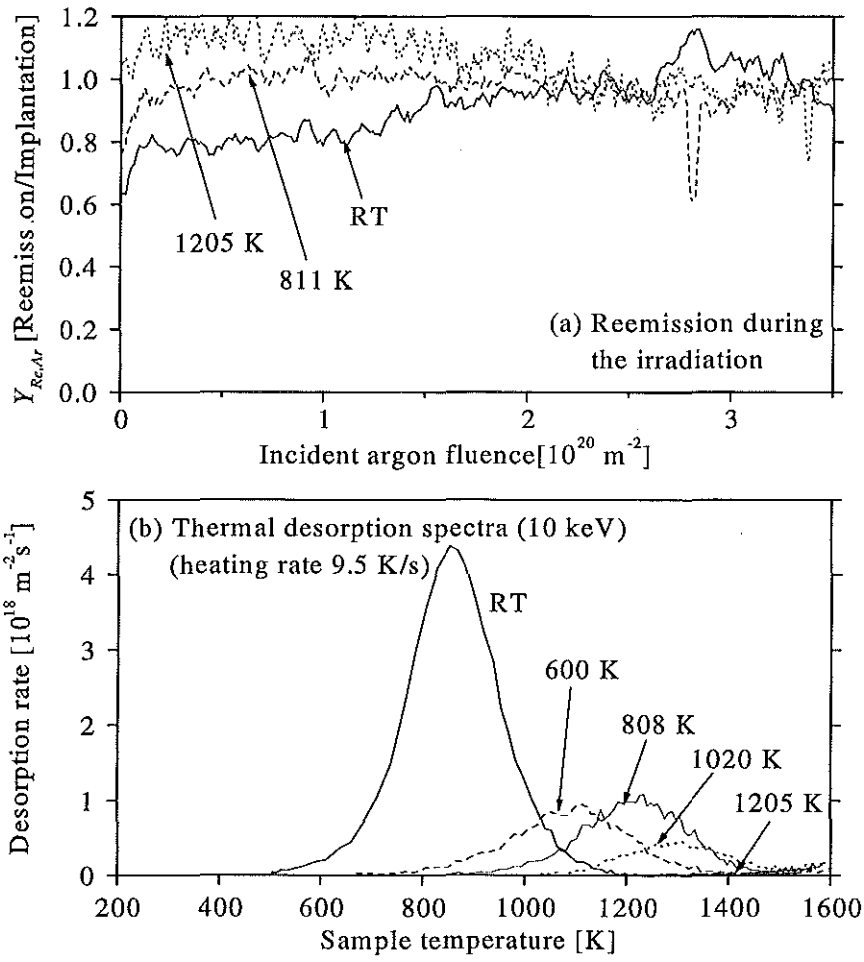

Figure 4-10 : Sample (EK98) temperature dependence of **(a)** reemission yield and **(b)** desorption spectra of argon (with similar incident fluence (5×10^{20} m^{-2})).

4.2.3 Investigation of the diffusion of argon

In section 4.1.4 it was shown that there is no diffusion of neon in graphite at room temperature. In order to investigate this also for argon the irradiated sample was left up to 3 days in the UHV chamber and the thermal desorption was carried out afterwards. This procedure was not only done at room temperature but also at 600 and 800 K. As was the case of neon, the desorption spectra and the amount of desorbed argon were identical to those done immediately after the irradiation, even at 600 and 800 K. One can therefore conclude that there is no diffusion of argon in graphite even at a temperature of 800 K. The same conclusion can also be drawn from the fact that the reemission yield does not increase with further irradiation after reaching unity (see Fig. 4-10(a), 811 K case).

4.3 Summary and Discussion of Ion Beam Experiments

Irradiations of graphite (EK98) with neon and argon ions at energies of 2, 5 and 10 keV were carried out. The reemission spectra during the irradiation were investigated and the amount of retained neon and argon was determined by thermal desorption spectra.

The reemission of neon after the start of the neon irradiation of graphite at room temperature behaves as expected: the reemission starts with zero and increases then gradually. This increase is smaller for irradiations at higher energies since more trapping sides are available due to the larger implantation range. This behaviour is in agreement with the small reflection coefficient of neon on graphite in this energy range. For energies above 1 keV Ne^+, the particle reflection coefficient is in the order of 10^{-3} at normal incidence [Eck98], which can also be neglected. Choi et al. [Cho93] explains the retention behaviour of neon in graphite with so called '*site-filling model*' [Bal84]: in the beginning of the irradiation most incident neon are trapped among the available trapping sites (between the basal planes of graphite, grain boundary, or dislocation), and the self-relocation or ion induce desorption plays a small role. As the concentration of neon in the graphite increases, the probability of self-relocation of neon starts to play an important role. Finally, after most available trapping sites in graphite are occupied, the probabilities of trapping and self relocation are balanced, then the reemission yield of neon reaches it maximum unity. However, this model assumes an uniform distribution of the implanted neon, which is not observed as seen in the retention dependence on the ion energy of the incident neon. And the reproducible hump in the reemission spectra for the irradiation with 10 keV neon at the fluence of ~ 2×10^{20} m^{-2} (see fig. 4-3) is difficult to understand with this model.

The reproducible hump in the reemission spectra during the irradiation was also reported in [Che96,Ali95], in which the reemission yield of helium from the **E**dge **O**riented **P**yrolytic **G**raphite (EOPG) implanted with 40 keV helium at room temperature shows a similar hump

in the early phase of irradiation. The authors explain it with the formation of helium bubbles and opening of them by the following incident heliums. The same experiment with EK98 however shows no such a hump [Ali95] and it is not yet proven whether such neon bubbles are formed or not. Even more difficult to understand is the neon retention. We have no model to explain that the saturation retention (area) density does not depend on the ion energy between 2 and 10 keV. If an uniform distribution of neon up to the implantation depth is assumed (a depth distribution was not investigated) the particle density is 0.55 Ne/C for 2 keV and 0.15 Ne/C for 10 keV Ne^+ implantation. General features of the irradiations of graphite (EK98) with argon, e.g. fluence and ion energy dependence, is quite similar to those with neon. The (area) retention density depends on the implantation energy, which is however is smaller than those of neon (0.18 Ar/C for 3 keV Ar^+ and 0.06 Ar/C for 10 keV Ar^+).

The desorption processes of both neon and argon seems to be of first order type. First, both are released from graphite as atoms; second, the maximum desorption temperature is independent of the incident fluence; and third, the desorption spectra is slightly asymmetric to the peak temperature. The maximum temperature of the neon desorption is 780 K and is comparable with other experiments: 390 – 430 K (HOPG, ramp rate: ~50 K/s) [Cho93], 615K (polycrystalline graphite, ramp rate: 2 K/s) [Bro97]. From the maximum temperature of the desorption spectra a binding energy for neon in graphite (E_b) of 2.06 eV is determined, which is comparable with that of 1.78 eV by Brosset et al. [Bro97]. The desorption spectra of argon is broader than that of neon and has a higher maximum temperature at 850 K. From the maximum temperature the binding energies of argon are derived to 2.35 eV.

The dependence of the reemission and desorption characteristic on the sample temperature was investigated for neon and argon. As the sample temperature increases more neon and argon are reemitted during the irradiation and at 1200 K practically all the incident neon and argon are immediately reemitted. The amount of desorbed neon and argon decreases with increasing sample temperature and over 1200 K no desorption was observed. The desorption spectra are shifted toward higher temperature with increasing sample temperature. What is remarkable, though not yet understood, is the fact that the shift of the desorption spectra is not within the envelope of that at room temperature but beyond it.

Ion-induced release of neon by subsequent D_2^+ irradiation and the diffusion of neon and argon were investigated. In this experiment no ion-induced release of neon by D_2^+ was observed. In order to simulate this effect for the application in TEXTOR more accurately, both neon and deuterium energy of less than 1 keV and the incident deuterium fluence of one order of magnitude greater than that of neon are needed, and the irradiation should be done simultaneously. Such experimental conditions were however impossible in our ion beam irradiation apparatus.

Both neon and argon show no diffusion in graphite at room temperature. It is already partly investigated by Choi et al. that diffusion of argon in graphite at room temperature is negligible [Cho93]. In addition, argon shows no diffusion in graphite even at elevated temperatures of 600 and 800 K.

5. Experimental Set-up of TEXTOR Experiment

In the beginning of this section the general features of TEXTOR-94 will be described. In the following section, details of the experimental features of the Sniffer probe and the characteristics of operation are provided.

5.1 TEXTOR-94

The tokamak experiment of Jülich TEXTOR-94 (**T**orus **EX**periment for **T**echnology **O**riented **R**esearch) [Wol84] was begun in 1981 with a goal of ***the investigation of the physical processes of plasma-wall-interaction***. For this purpose TEXTOR-94 has an extraordinary good accesses to the plasma edge and a good possibility for the active optimisation of the wall and plasma edge. TEXTOR has been upgraded several times and the name of TEXTOR-94 is named after the last upgrade in 1994.

TEXTOR-94 has a vacuum chamber with the major radius of 1.75 m which is surrounded by 16 toroidal field magnet. Inside of the vacuum chamber TEXTOR-94 has an exchangeable and heatable (up to ~ 900 K) inner torus, so called liner, made of stainless steel (Inconel 625). In order to define the plasma radius and to protect the liners, three limiter systems made of graphite [Sam89] are installed in TEXTOR-94. With the help of them the minor radius (the radial position of **L**ast **C**losed **F**lux **S**urface) can be varied from r = 0.4 m to r = 0.48 m. Main features of three limiters are summarised below:

- ***Three poloidal main limiters*** are poloidally 0.25 m long and placed top, outside, and bottom of the vacuum chamber. The radial position of them is variable within the limit mentioned above.

- ***A toroidal pump limiter (ALT II)*** [Goe89] is composed of 8 pieces which are parallel to the toroidal magnetic field (B_T) and movable in radial direction. The length of total toroidal limiter is 12 m. With a help of turbo molecular pump in the back side of this limiter, neutral hydrogen as well as impurity atoms such as neon and helium can be removed from the particle cycling.

- ***The inner bumper limiter*** is placed inside of the torus at the fixed radius of r = 0.488 m. The role of it is to prevent the direct contact of plasma with the metallic liner (inside).

Beyond these features, TEXTOR-94 has 2 limiter locks through which further test limiters, made of various materials, can be inserted into the plasma edge up to r = 0.4 m without breaking of vacuum.

The maximum plasma current (I_p) is 800 kA and the maximum toroidal magnetic field (B_T) is 2.8 T. Most of the experiments in this work are carried out under standard conditions: Ip = 400 kA and B_T = 2.25 T. In addition to the **O**hmic **H**eating (OH) the plasma can be heated with two **N**eutral **B**eam **I**njections, parallel (NBI co) and opposite (NBI counter) to the direction of plasma current, with a maximum power of 1.5 MW respectively and with **I**on **C**yclotron **R**esonance **H**eating (ICRH) with a maximum power of 4 MW. In order to protect the metallic first wall and to reduce the metallic and oxygenic impurities, wall conditioning of TEXTOR-94 with low-Z materials are carried out (Carbonization, Boronization [Win96] and Siliconization [Win93]), in which limiters and walls are conditioned with corresponding gas mixtures. Fig. 5-1 shows an overview of TEXTOR-94 with its limiter systems, the extra heating systems and the Sniffer probe (between the toroidal field coils No. 1 and No. 16).

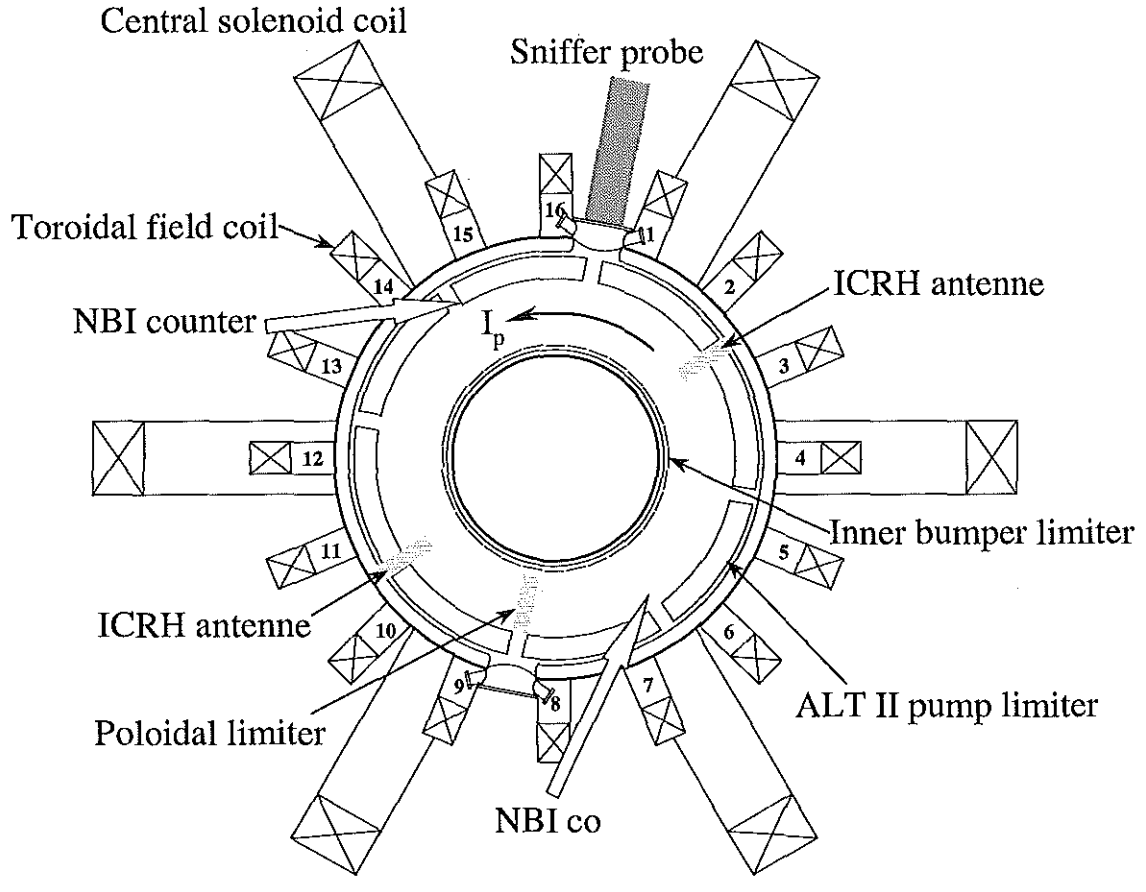

Figure 5-1 : TEXTOR-94

5.2 Sniffer Probe

5.2.1 Overview of the Sniffer probe

A schematic overview of the Sniffer probe is depicted in fig. 5-2. The Sniffer probe can be driven into the plasma horizontally from the low field side up to minor radius r = 0.44 m. If not commented in the text, the radial position of the Sniffer probe was at r = 0.49 which is 3 cm behind the **L**ast **C**losed **F**lux **S**urface. The Sniffer probe has an aperture in the ion side direction of TEXTOR-94 (see fig. 5-1). Ions moving along the magnetic field enter the aperture and are neutralised by impinging onto the graphite target in the middle of the probe head. Partial pressures of the neutralised gases can then be measured by **Q**uadruple **M**ass **S**pectrometer (QMS). Due to very high incident flux ($\Phi_{H,S} > 1\times10^{22}$ [$m^{-2}s^{-1}$], $\Phi_{Ne,S} > 1\times10^{21}$ [$m^{-2}s^{-1}$]) and low energy (< 1 keV), the graphite target is saturated with incident ions immediately after the beginning of a discharge and the reemission spectra can be regarded as incident ion flux with only a little error. The exposure of graphite sample was done during the discharge between 1 to 4 s after the beginning of the discharge, controlled by a shutter behind the aperture. The amount of retained atoms in the graphite target was measured by thermal desorption spectroscopy 100 sec after the discharge.

The basic arrangement of the Sniffer probe in TEXTOR-94 is already described by Philipps [Phi96]. Here we describe the main components of the Sniffer probe and the essential experimental procedures.

5.2.2 Experimental facilities

5.2.2.1 Probe head module

The probe can be driven, from the low field side, up to minor radius r = 0.44 m with a stepping motor (SIGMA, USA). Precise position control was done by UNIDEX and SONY (MAGNESCALE, LY-101, Japan) displaying system. All the measured (QMS, temperature, position and pressure) and control (heating ramp) signals are transferred via isolating amplifier (Serie GTN, Baur Elektronik) and optical fibres from TEXTOR bunker to diagnostic room, or vice versa.

Fig 5-2 shows the details of the probe which is composed of a graphite target, an aperture, a shutter and calorimeter. The probe body is made of the stainless steel tube with an outer diameter of 7.5 cm and the probe cap is made of isotropic fine grain graphite (EK98, Ringsdorff), fastened also by EK98 screw, in order to prevent the formation of metal impurities in the plasma.

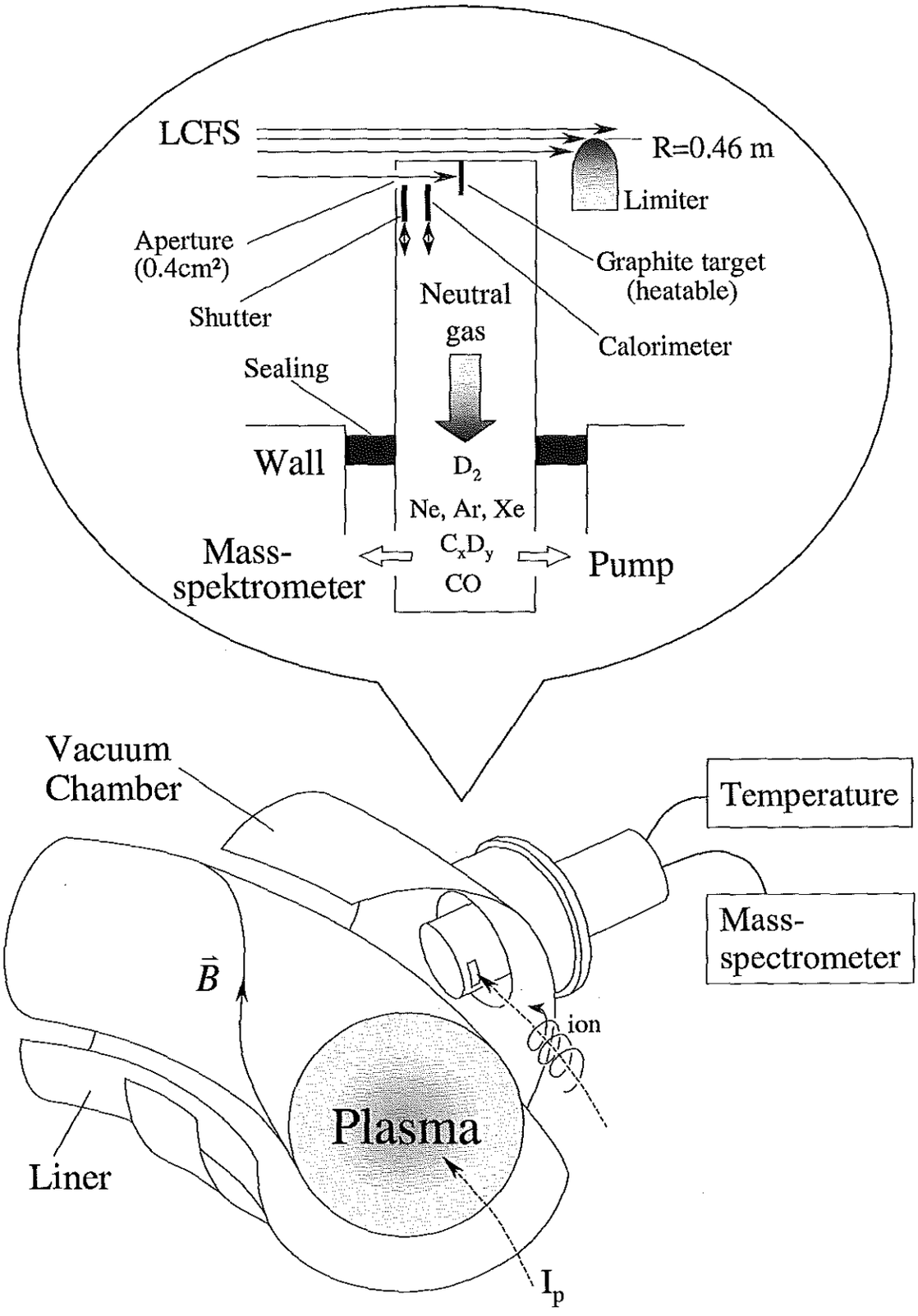

Figure 5-2 : Schematic diagram of the Sniffer probe

The target, located in the middle of the probe, has a dimension of 50×7×0.2 mm^3 and is also made of EK98. The target can also be biased up to – 200 V and the small saturation current can be measured from the voltage drop of known resistance. In this experiment however the sample was always at floating potential. For the thermal desorption spectroscopy the graphite target was heated up to 1900 K with linear current ramping (maximum current: ~ 50 A, NTN700, FUG), which is programmed by an automating processor of SIMATIC (S5-100U, Siemans). Since the target is encapsulated during the desorption, the in-situ measurement of the target temperature itself during the desorption was impossible. Therefore the steady state current value for each temperature was measured by a filament optical pyrometer and these data are taken for the temperature during the ramping period. Due to the high ramping rate of ~ 120 K/s, only approximate temperature can be estimated during the thermal desorption spectroscopy. Both ends of the target are clamped on two copper blocks, cooled separately by coaxially flowing air pressure, through which also the heating current flows. No technical problem was found in heating the target up to the maximum temperature.

A rectangular aperture, with the dimension of 4×10 mm^2, is machined in the probe cap and located 7 mm behind the top of the probe. The exposure during the discharge (t = 1 – 4 s) was controlled by a shutter, made of stainless steel, moved by air pressure. Though the shutter is not fully vacuum tight, by closing the shutter the unwanted noising effect of the plasma during the ramp up and down phase can be significantly reduced. The control signal of the shutter is programmed by an automating processor of SIMATIC (S5-100U, Siemans) which is triggered by the start signal of the TEXTOR discharge.

In order to measure the deposited energy, which is responsible for the temperature rise of the graphite sample during the discharge, a graphite (EK98) block (50×10×4 mm^3), which is movable with air pressure, is installed between the shutter and the target. Both ends are connected with thermocouple (NiCr-Ni) to measure the temperature rise of the graphite block. The measuring temperature ranges from 520 K to 870 K [Her98].

At a position of r > 0.47 m, no technical problem was found under the normal discharge conditions. At smaller minor radii, however, the power flux to the sample is sometimes so high as to cause mechanical failure of the system.

5.2.2.2 Vacuum system

The Sniffer probe experiments were performed in a ultra-high vacuum (UHV) facility (total volume of about 200 l) which was pumped by a 360 L/s turbo-molecular pump (Turbovac360, Leybold-Heraeus) and backed by a mechanical pump (Trivac, Leybold-Heraeus) (see fig. 5-3). The pressure was monitored, both near the probe head (M1, practically same as that of TEXTOR) and near the QMS (M2 - M4), via Bayard-Alpert type

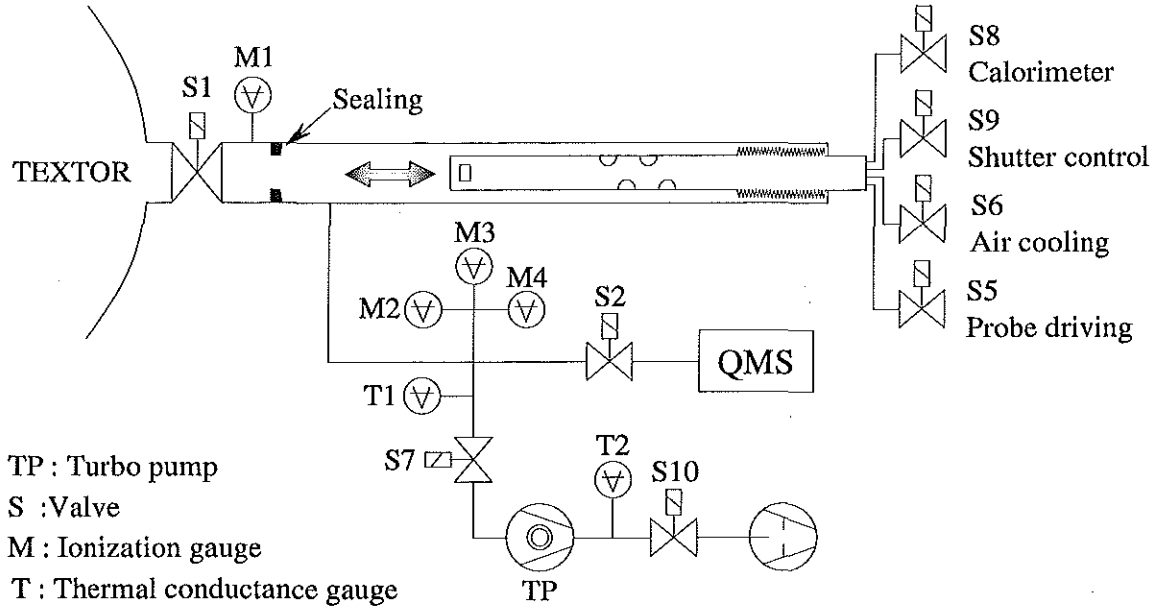

Figure 5-3 : Vacuum System of the Sniffer probe.

ionization gauges (IM210, Leybold-Heraeus) and thermal conductivity gauges (TR200, Leybold-Heraeus). The typical pressure of the QMS chamber is less than 1×10^{-4} Pa without plasma and reaches up to 1×10^{-3} Pa during the discharge, from which the flow in the Sniffer probe is considered to be molecular (P·d (= 1×10^{-5} mbar × 200 mm) << 0.133) [Laf98]. The effective vacuum conductance of the Sniffer probe can be measured from the pressure difference of TEXTOR ($P_{TEXTOR} = P_{Sniffer} \cdot (1 + S/L)$, where S : 340 l/s) and also calculated by the geometry [Ede86]. Both values are relatively in good agreement: L_{D_2} = 133 l/ with the probe head withdrawn and L_{D_2} = 11.8 l/s with the probe head driven into the plasma. Comparing the conductance of the tube (162 l/s) and the small conductance of the aperture (~ 12.5 l/s), as mentioned by Philipps et al. [Phi89], the possible backflux of the neutralised gas through the aperture back into the plasma is small in comparison with that to the QMS and thus can be neglected.

Since the QMS is located about 3 m apart from the aperture, the pressure rise measure by QMS has an unavoidable time delay. As shown in fig. 5-4, one can describe the time behaviour of the pressures of source and measuring chamber using a two chamber model.

The pressures of the two chambers can be described with two differential equations Eq. 5-1, and 5-2.

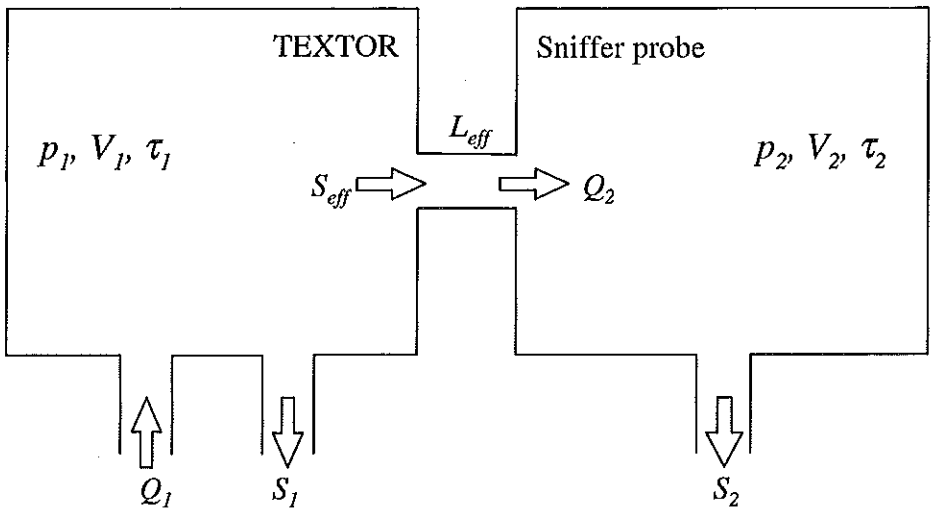

Figure 5-4 : Schematic diagram of the pressure balance in TEXTOR and in the Sniffer probe.

$$V_1 \cdot \frac{dp_1}{dt} = Q_1 - (S_{eff} + S_1) \cdot p_1 \tag{5-1}$$

$$V_2 \cdot \frac{dp_2}{dt} = Q_2 - S_2 \cdot p_2 \tag{5-2}$$

where $\frac{1}{S_{eff}} = \frac{1}{L_{eff}} + \frac{1}{S_2}$. Introducing the integration factor ($e^{t/\tau}$, where $\tau_1 = \frac{V_1}{S_{eff} + S_1}$) one can solve the Eq. 5-2 as following:

$$p_1(t) = \frac{1}{V_1} \cdot e^{-t/\tau_1} \{ \int_0^t e^{t/\tau_1} Q(t) dt + p_{1,t=0} \} . \tag{5-3}$$

Then by inserting Eq. 5-3 into Eq. 5-2 and from the fact that $Q_2 = L_{eff}(p_1 - p_2)$, one can derive the P_2:

$$p_2(t) = \frac{L_{eff}}{V_2} \cdot e^{-t/\tau_2} \{ \int_0^t e^{t/\tau_2} p_1(t) dt + p_{2,t=0} \} \tag{5-4}$$

where the integration factor $\tau_2 = \frac{V_2}{S_2}$. Fig. 5-5 shows the pressures of TEXTOR ($p_T \leftarrow p_1$) and Sniffer probe ($p_S \leftarrow p_2$) measured (solid line) at a gas test shot (#75544, with V_1: 17000 l, S_1: 16200 l/s, L_{eff}: 11.8 l/s, V_2: 200 l, S_2: 340 l/s)), and p_S calculated with Eq. 5-4 (dashed line). As shown, the calculated and measured pressures of the Sniffer probe are in good agreement and

has, due to the small L_{eff}, a time delay (Δt) of about 0.5 s. This time delay increases with increasing atomic mass. In order to describe the transient behaviour of the pressure in TEXTOR, this time delay should be taken into account. Due to the large pumping speed (340 l/s) relative to the Sniffer probe volume (200 l), p_S has practically the same pressure drop as that of p_T at larger times.

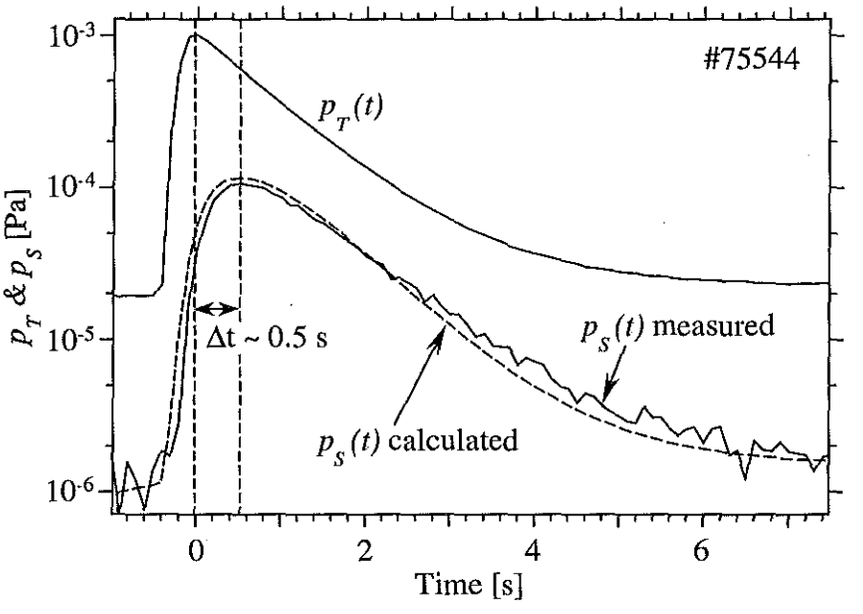

Figure 5-5 : Time evolution of the pressures in TEXTOR (p_T) and in the Sniffer probe (p_S) measured (solid line) at a gas test shot (#75544). (The dashed line is p_S calculated with Eq. 5-4).

5.2.2.3 Quadruple mass spectrometer (QMS) and its calibration

For the particle flux and the TDS measurements, a **Q**uadruple **M**ass **S**pectrometer (QMG112A, BALZERS) was used for the residual gas analysis, which is composed of an axial beam ion source and **S**econdary **E**lectron **M**ultiplier (SEV117, BALZERS). In order to prevent the magnetic perturbation of various TEXTOR field coils, the whole detecting head including ion source and the SEM is shielded by μ metal chamber.

Several methods have been used to calibrate the signals of the QMS: **first**, a gas test shot with a known amount of gas can be used to derive the pumping speed of the gas concerned. Comparing the amount of gas puffed and the integration of the QMS signal multiplied by the pumping speed, one can derive a calibration factor. **Second**, when the QMS chamber is filled with relatively pure gas at a constant pressure, one can derive the partial pressure of the gas using the multiplication factor of the ionization gauge for that gas. Comparing the partial

pressure and the QMS signal, one can derive a calculation factor. The calibration factors derived by the two methods above are in reasonable agreement and, though not always constant, do not change significantly for different calibrations. The ratios of the measured calibration factors for different gases are also in good agreement with that given by the manufacture [BalB96]. When the desired calibration factor was not available, the factor given by the manufacture has been.

5.2.3 Experimental procedures

5.2.3.1 Incident ion flux and thermal desorption spectroscopy

In order to expose the graphite target to the incident ion flux, the probe head was driven into the scrape off layer of the plasma. The usual radial position was at r = 0.49 m (3 cm behind the LCFS). Due to the sealing between the TEXTOR main chamber and Sniffer probe vacuum system (see fig. 5-3), the particles from the TEXTOR main chamber can enter the Sniffer probe only through the aperture (L_{eff} : 11.8 l/s for deuterium). A shutter behind the aperture was opened during the discharge (t = 1 – 4 s). Taking into account the time delay of the pressure in the Sniffer probe, the incident flux was taken from the value at t = 3 s, at which most flux signals are in the steady state phase. The measurement of the incident neon and argon fluxes during the discharges without impurity injection a small background was observed, when the former discharges are with impurity injection (*memory effect*). Since these signals are also surely neon and argon, they are considered as incident neon and argon signals.

Though most of the discharges analysed are D-D discharges, all the hydrogen isotopes (*m/e* = 2, 3, 4) were observed in fusion plasma due to the cracking and the interaction of atomic deuterium with hydrogen stored in the walls [Phi92]. In determining the hydrogen flux, all these hydrogen isotopes were taken, weighted with the relative sensitivity of QMS [BalB96], and summed together. If there is no other comment, this summation is taken as the total hydrogen (H_{tot}) flux. Since most of the shots are D-D discharges, the majority of H_{tot} is deuterium. It can reach up to 90 % of H_{tot} at discharges with high radiation level.

In every measurement of neon, since ^{20}Ne (*m/e* = 20) has a contribution of hydrocarbon (CD_4) as a background, ^{22}Ne (*m/e* = 22, natural abundance: 10 % of ^{20}Ne) was always used to determine the neon. It is experimentally proved in gas test shots that ^{20}Ne and $^{22}Ne\times10$ are in good agreement. The signal at *m/e* = 22 also has a background of CO_2^{++} (cracking of CO_2 (*m/e* = 44) created in the ionization chamber of the QMS). Though it is difficult to distinguish this background from ^{22}Ne, it can be clearly separated in the TDS due to the different temperature behaviour. The background is experimentally shown to be ~ 2 % of the CO_2^+ (*m/e* = 44) signal and subtracted from *m/e* = 22 signal during the discharge and for the TDS measurements.

For the detection of argon, the ^{40}Ar (m/e = 40) signal was taken since the contribution of other isotopes at this mass (~ 0.4 %) is negligible. Argon (m/e = 40) has also a background from C_3D_2 from the chemical erosion, which is closely correlated with the signals of C_3D_3 (m/e = 42) and C_2D_3 (m/e = 30). This background however is significant only during the ramp down of the plasma current I_p and is negligible during the discharge. Though at the discharges with very small incident argon flux (from the last shots) this background is comparable to the argon signal, at the discharges with argon injection however this background can be neglected.

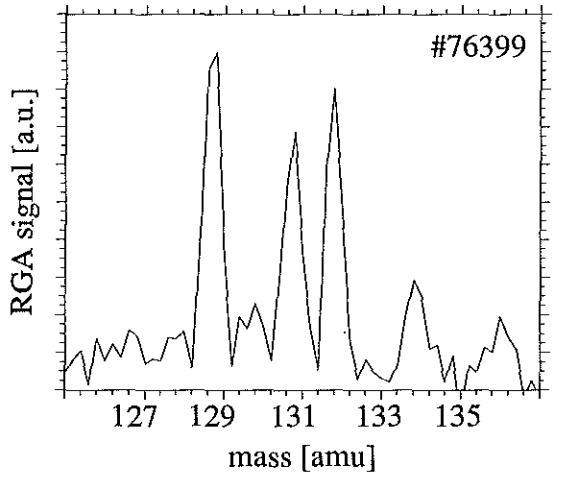

Figure 5-6 : Mass separated QMS mass spectrum signal of Xe

The detection of xenon was more difficult due to the very small amount of xenon injected into the plasma during the discharges. As shown in fig. 5-6, however, one could clearly measure the neutral xenon with the QMS (*mass scan mode*). It shows three major xenon peaks at M=129, M=131 and M=132, which is consistent with the natural abundance of the xenon isotopes {M129 (26.4%), M131 (21.2%), M132 (26.9%)} [BalB96].

Notwithstanding the high sensitivity of the mass spectrometer, there were some problems in measuring the time evolution of xenon during the discharge: with the rise of xenon (M129, M131, M132) signals, the background signals at surrounding masses (masses from 125 to 135) increases also in a similar manner. Thus it was impossible to distinguish a possible small rise of the xenon signal from the background with *spectrum point mode* (max. time resolution 1 ms). In order to distinguish therefore this small rise of xenon from the background, the *mass scan mode* was used, which however has a time resolution of ~ 50 ms (see fig. 6-30(b)). For this reason, xenon was detected only with bad time resolution (~ 50 ms) during the discharge. The retention of xenon could not be determined due to the reasons mentioned above.

5.2.3.2 Residual gas measurement after the discharge

The noble gases temporally retained in the walls during the discharge might be released after the end of the discharge. In order to measure this outgassing, the Sniffer probe QMS system has been used but with the probe head withdrawn. Thus the conductance is 163 l/s for deuterium. The outgassing signals are usually measured up to 150 s after the discharge.

Sometimes it is also measured until the beginning of the next shot. In this thesis the outgassings of argon and xenon were measured.

6. Results from Experiments in TEXTOR-94

This section is divided into three chapters for the three different inert gases Ne, Ar and Xe. Each chapter describes at first the global observations of the overall particle balance and the resulting effective wall pumping. Then experiments and results obtained with the Sniffer probe are described, which are compared with those from the global observations and from the ion beam experiments.

6.2 Experimental Results for Neon

Fig. 6-1(a) shows typical signals of a RI-mode discharge at TEXTOR-94 with feed-back controlled neon-injection (solid lines). Neon was injected at t = 1.46 s after the line averaged electron density (n_e, see 4.1.2) is nearly constant and under constant external heating of 1.2 MW NBI (**N**eutral **B**eam **I**njection) and of 1.35 MW ICRH (**I**on **C**yclotron **R**esonance **H**eating). Two discharges with (solid line, #68810) and without neon-injection (dashed line, #68812) but otherwise under the same plasma conditions (B_T = 2.25 T, I_p = 400 kA) require different external (deuterium) fuelling. The neon seeded discharge needs only a small external fuelling just after the neon-injection (no figure), whereas the discharge without neon-injection needs continuous gas feed in order to keep the desired density value. This is a typical behaviour of neon seeded RI-mode discharges compared with discharges without neon-injection. The different fuelling behaviour is also seen in the development of the line averaged density (n_e) which increases after neon-injection somewhat above the value preset by the feedback control system. This observation demonstrates again clearly that the ***neon-injection improves the particle confinement***, as already discussed more in detail in section 2.2. Fig. 6-1(a) shows also the increase of the total radiated power (P_{rad}) with neon-injection (solid line, #68810) compared to that without neon-injection (dashed line, #68812). The increase of P_{rad} with neon-injection is, as discussed in section 2.2, accompanied by ***the decrease of convective power load on the plasma-facing materials***.

Fig 6-1(b) shows more signals that are important to follow the neon-injection and its control: *NeVIII*, as described in 4.1.3, is the line radiation of Li-like neon. Under similar plasma conditions this signal can be assumed to be proportional to the total number of neon in the plasma. It is therefore used for the feedback control of the neon concentration in the plasma (see section 2.2). The rapid rise and the following saturation of the *NeVIII* signal shows that the desired concentration of neon in the plasma is achieved just about 100 ms after the start of the neon injection and stays then constant. $\Gamma_{ext,Ne}$ is the rate of the neon seeding

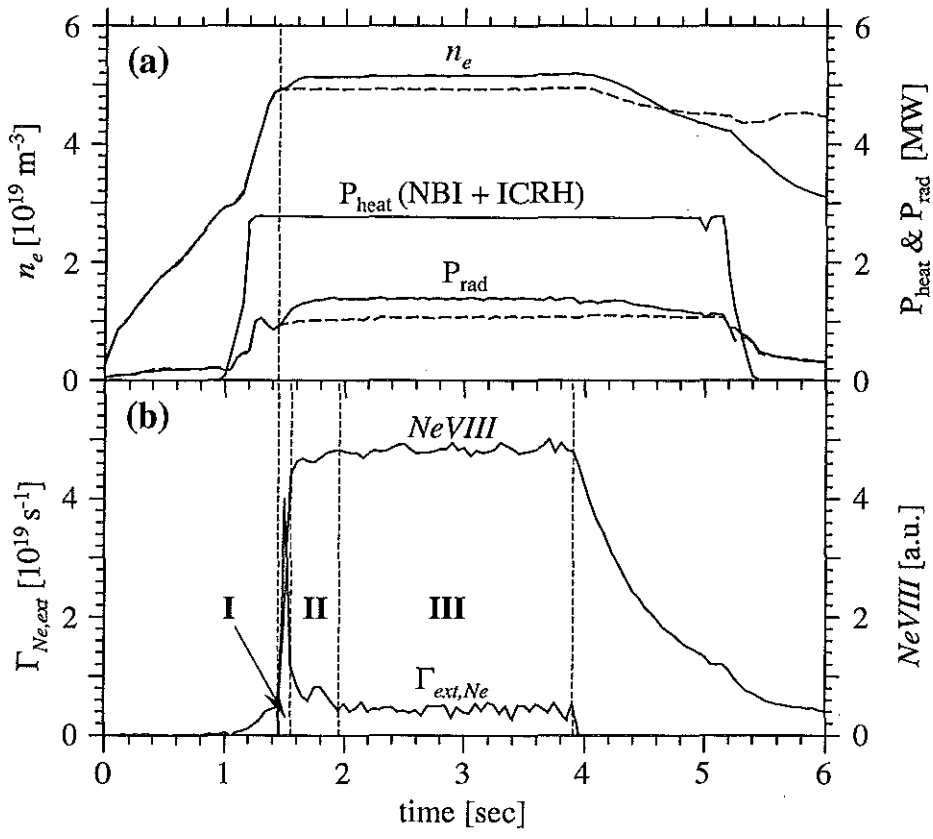

Figure 6-1 : Typical signals of TEXTOR-94 discharge (solid line: with neon-injection (#68810), dashed line: without neon-injection (#68812)) **(a)** line averaged electron density (n_e), heating power (P_{heat}), and total radiation power (P_{rad}), **(b)** external neon seeding rate ($\Gamma_{ext,Ne}$) and line radiation of Li-like neon ions (*NeVIII*).

through the fast gas injection system feed-back controlled by the *Ne-VIII* signal. The detailed analysis shows that the desired neon concentration in the plasma is achieved just after the beginning of neon-injection within about 100 ms (i.e. *NeVIII* constant). However the trace of the neon seeding rate ($\Gamma_{ext,Ne}$) shows that neon is further injected but with no change of the neon concentration in the plasma. Thus the neon-injection and recycling can be divided into three phases: in **phase I** (t = 1.46 – 1.56 s) the injected neon contributes to build up the desired neon concentration in the plasma and a part of it is pumped by other channels. In **phase II** (t = 1.56 – 1.96 s) neon is further injected with a decreasing injection rate but the neon concentration is already in steady state. This, in connection with the transient injection rate, can only be understood by assuming that neon is not only pumped out by ALT pumps but also retained in the walls (***wall pumping***). In **phase III** (t = 1.96 – 3.9 s) the neon-injection rate is constant and decreases to zero when the ALT pumps are closed. This shows that effective neon wall pumping in this phase is saturated and neon is only pumped out by the action of the ALT pumps.

6.2.1 Global observation

6.2.1.1 Total number of neon in the plasma

Fig. 6-2 compares the total electron density ($n_{e,tot}$), *NeVIII* and the external neon seeding rate ($\Gamma_{ext,Ne}$) for two discharges with neon injection under different ALT II pump conditions at its end phase of the neon-injection: in (a) all ALT II pumps are open (#68825) and in (b) all ALT II pumps are closed (#68835). While for the discharge #68825 plasma particles can be pumped out both by the ALT II pumps and by possible wall pumping, particles in discharge #68835 can only be pumped out by wall pumping. It should be mentioned here that the possible pumping of plasma particles by other pumps, called main pump in horizontal position, except the ALT pumps can be neglected. This can be deduced from the neutral gas pressure below 10^{-5} mbar measured in front of the main pump and its pumping speed of 2400 l/s. The resulting pumping rate of 2×10^{-3} mbar·l/s (= 5×10^{16} particles/s) is below 1 % of that of the ALT pumps and can thus be neglected.

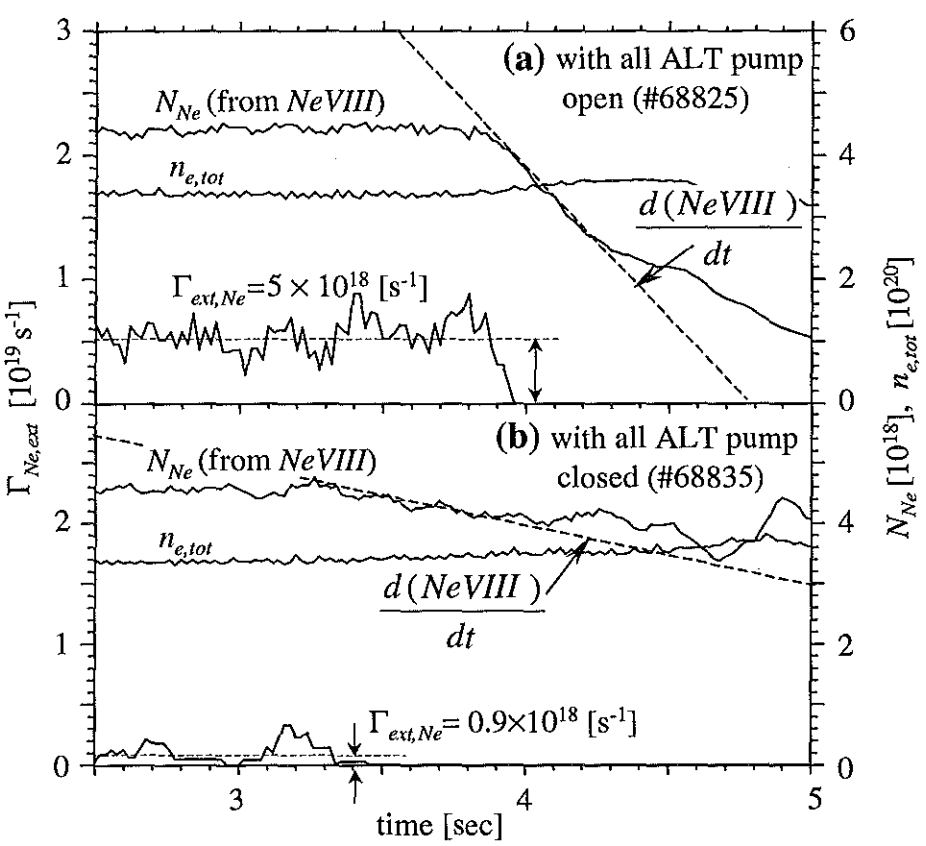

Figure 6-2 : Derivation of the total number of neon in the plasma (N_{Ne}) **(a)** with all ALT pumps open (#68825), **(b)** with all ALT pumps closed (#68835) (where, $n_{e,tot}$ is the total number of electron, $\Gamma_{ext,Ne}$: external neon seeding rate).

Fig. 6-2(b) shows that the neon concentration stays constant before the feedback controlled neon-injection is finished (t = 3.5 s) and that the external seeding rate of neon is far smaller than that in (a). The decrease of the neon signal is rather slow which shows the wall pumping is negligibly small in this phase. The comparison with the discharge with external pumping shows that the decrease of the neon signal after switching off the neon-injection is mainly due to the ALT pump rate. Since other plasma conditions are constant before and after the neon-injection, ***the total amount of neon in the plasma*** (N_{Ne}) can be deduced from the simple one dimensional particle balance equation [Ehr96]:

$$\frac{dN_{Ne}}{dt} = \Gamma_i - \Gamma_o = (\Gamma_{ext,Ne} + R_{Ne}\Gamma_o) - \Gamma_o \qquad (6\text{-}1)$$

where Γ_i and Γ_o are the overall incoming and outgoing neon fluxes and the incoming neon flux Γ_i is given by the summation of external fuelling rate ($\Gamma_{ext,Ne}$) and the recycling flux of neon ($R_{Ne}\Gamma_o$, where R_{Ne} is the recycling coefficient of neon). The outgoing flux of neon can also be described by the global particle confinement time of neon ($\tau_{p,Ne}$) as $\Gamma_o = \frac{N_{Ne}}{\tau_{p,Ne}}$ (see section 2.1.2). When this is introduced into Eq. (6-1),

$$\frac{dN_{Ne}}{dt} = \Gamma_{ext,Ne} - (1 - R_{Ne})\frac{N_{Ne}}{\tau_{p,Ne}} \qquad (6\text{-}2)$$

$$= \Gamma_{ext,Ne} - \frac{N_{Ne}}{\tau^*_{p,Ne}} \qquad (6\text{-}3)$$

where $\tau^*_{p,Ne}(=\frac{\tau_{p,Ne}}{1-R_{Ne}})$ is, as already explained in section 2.1.2, the effective particle confinement time of neon. Using the fact that '$\Gamma_{ext,Ne}$ *is zero*' just at the end of the neon-injection, ***one can derive*** $\tau^*_{p,Ne}$ from Eq. (6-3) by

$$\tau^*_{p,Ne} = -\frac{N_{Ne}}{\frac{dN_{Ne}}{dt}} = -\frac{NeVIII}{\frac{d(NeVIII)}{dt}}. \qquad (6\text{-}4)$$

The total number of neon in the plasma N_{Ne} during the stationary phase of the discharge ($\frac{dN_{Ne}}{dt} = 0$) can then be derived from Eq. (6-3) using the known fuelling rate $\Gamma_{ext,Ne}$, and $\tau^*_{p,Ne}$:

$$N_{Ne} = \tau^*_{p,Ne} \cdot \Gamma_{ext,Ne}. \qquad (6\text{-}5)$$

When the total number of neon in the plasma is derived, the *NeVIII* signal can be calibrated for the given discharge conditions and the temporal behaviour of the neon in the plasma can be evaluated. This is only allowed when the plasma conditions during the discharge do not vary much. The concentration of neon (with respect to the electron density) in the plasma ($c_{Ne} = N_{Ne}/n_{e,tot}$, $n_{e,tot}$: total number of electrons). Tab. 6-1 lists the measured and determined values γ, $\tau^*_{p,Ne}$, $\Gamma_{ext,Ne}$, $n_{e,tot}$, N_{Ne}, M_{Ne} ($= \frac{N_{Ne}}{NeVIII}$) and c_{Ne} for a series of RI mode discharges. These discharges were carried out under similar conditions: similar line averaged electron density (n_e = 5.8×10^{19} [m^{-3}]), radiation levels (γ ~ 0.85) and with the same heating power (P_{tot} ~ 2 MW). As can be seen, *N_{Ne} and c_{Ne} are relatively constant under various ALT pump conditions.* It is thus possible to find a standard relation between the *NeVIII* line radiation and the overall neon concentration for those conditions. In other words, ***N_{Ne} and c_{Ne}*** **can be derived** from a reference discharge when other plasma conditions are similar.

Number of ALT II opened	γ	$\tau^*_{p,Ne}$ [s]	$\Gamma_{ext,Ne}$ ×10^{18} [s^{-1}]	$n_{e,tot}$ ×10^{20}	N_{Ne} ×10^{18}	M_{Ne} ×10^{18}	c_{Ne} [%]
8 (all) (#68825)	0.85	0.91	5.0	3.38	4.55	1.65	1.30
5 (#68828)	0.84	1.23	3.5	3.46	4.31	1.54	1.25
3 (#68829)	0.87	1.35	3.0	3.48	4.05	1.46	1.16
1 (#68831)	0.90	4.17	1.3	3.42	5.40	1.95	1.58
0 (#68835)	0.85	5.64	0.9	3.38	5.10	1.80	1.51
Average				3.42	4.68	1.68	1.36

Table 6-1 : Total number of neon in plasma (N_{Ne}), neon concentration ($c_{Ne} = N_{Ne}/n_{e,tot}$) and calibration factor of *NeVIII* ($M_{Ne} = \frac{N_{Ne}}{NeVIII}$) (where, γ : radiation level (= P_{rad}/P_{tot}), $\tau^*_{p,Ne}$: effective confinement time, $\Gamma_{ext,Ne}$: external neon seeding rate, $n_{e,tot}$: total number of electron in plasma).

Fig. 6-3 shows the total number of neon atoms in the plasma (N_{Ne}) derived by Eq. (6-5) and the neon concentration (c_{Ne}) for various densities n_e and radiation levels γ. The absolute value of N_{Ne} is relatively in good agreement with that estimated from the average neon density n_{Ne} of all neon ionization states calculated by the self-consistent 1-D impurity transport code RITM (i.e. total number of neon in TEXTOR (= 6×10^{18}) obtained by multiplying average n_{Ne} (=3.5×10^{17} m^{-3} calculated by RITM [Unt95] at n_e = 4.5×10^{19} m^{-3} and γ = 0.85, see fig. 2-5) with TEXTOR volume (17 m^3)).

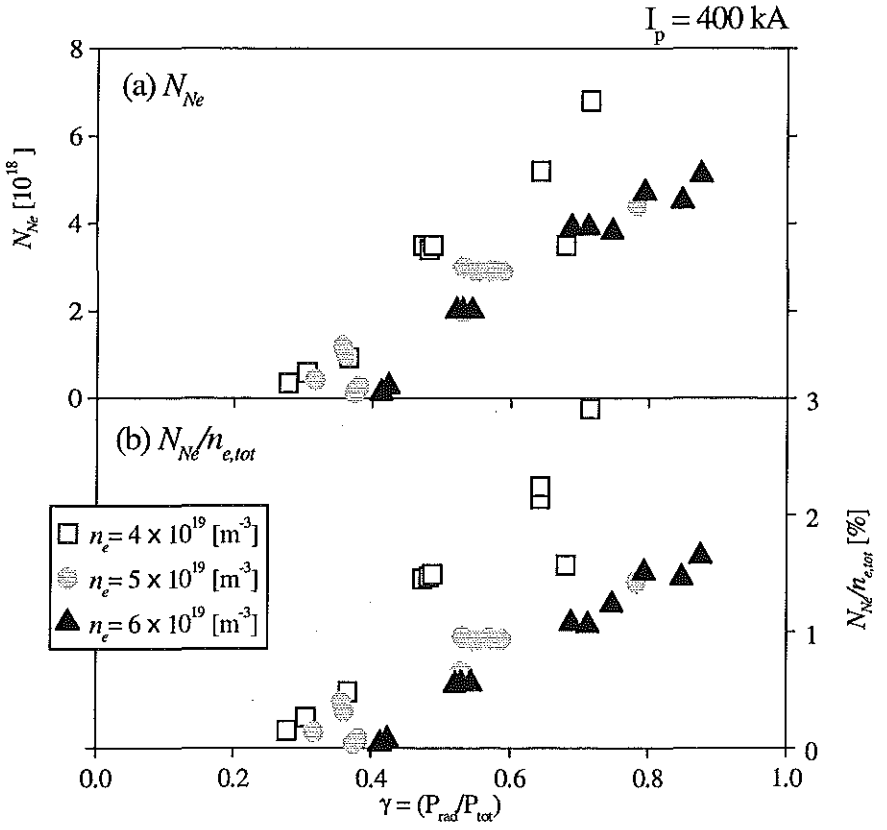

Figure 6-3 : **(a)** Total number of neon (N_{Ne}) in the TEXTOR plasma and **(b)** its concentration c_{Ne} (= $N_{Ne}/n_{e,tot}$) as a function of γ for different n_e.

At first, one can see that N_{Ne} and c_{Ne} increase with increasing γ since more neon is seeded at higher γ. Fig. 6-3(a) shows also that ***N_{Ne} increases with decreasing n_e for the same radiation level γ.*** This is due to the fact that with decreasing density the plasma temperature T_e, increases since the same heating power is distributed to less particles [Tok92,Sch98]. As a consequence, the total amount of radiated power per released or seeded impurity, the so called *radiation potential* (E_{rad}), decreases (see fig. 2-4) [Tok92]. Thus more neon is needed to achieve the same impurity radiation. This behaviour is even more pronounced for the neon concentration as shown in Fig. 6-3(b). The data on the overall neon concentration derived in this way will be compared with those by other diagnostics in the following section. The dependence of N_{Ne} and c_{Ne} on n_e and γ will be compared with measurements obtained by Sniffer probe in section 6.1.2.1.

6.2.1.2 Effective particle confinement time of neon

With the help of the temporal behaviour of the absolute values of N_{Ne} determined from the measured *NeVIII* and the calibration factor M_{Ne} the **time behaviour of the effective particle confinement time of neon** $\tau^*_{p,Ne}$, from Eq. 6-3, can be obtained as follows:

$$\tau^*_{p,Ne}(t) = \frac{N_{Ne}}{\Gamma_{Ne,ext} - \frac{dN_{Ne}}{dt}}. \qquad (6\text{-}6)$$

Fig. 6-4 shows $\tau^*_{p,Ne}(t)$ derived by Eq. (6-6) for the same discharge shown in fig. 6-1 (#68810 with neon-injection).

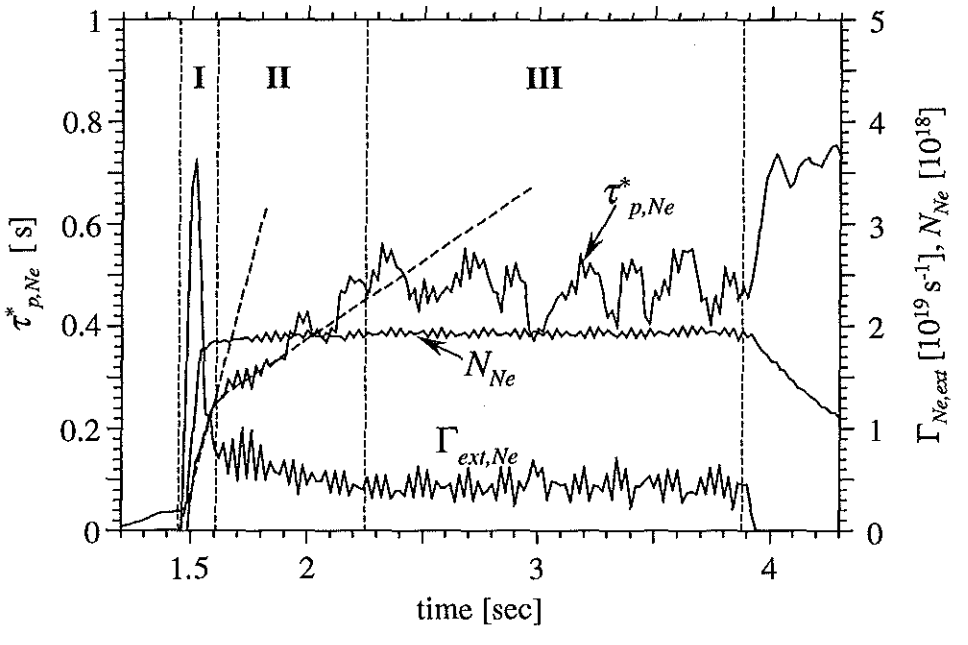

Figure 6-4 : Time behaviour of neon $\tau^*_{p,Ne}$, where N_{Ne}: total number of neon in plasma, $\Gamma_{ext,Ne}$: external neon seeding rate.

Similar as for the external fuelling rate $\Gamma_{ext,Ne}$ in fig 6-1, the time evolution of $\tau^*_{p,Ne}(t)$ can be divided into three different phases. In **phase I,** which lasts about 100 ms, $\tau^*_{p,Ne}$ ***increases very rapidly linearly with time***. In this time interval the external neon gas feed builds up the neon concentration in the plasma. The slower rise of effective particle confinement in this phase implies that more neon is seeded compared to what is observed in the plasma. This requires that some of neon seeded is missing somewhere else. This is most probably due to

the wall absorption that might be enhanced in this phase due to the localised neon seeding. On the other hand, in this phase the neon distributes inside the plasma volume that requires some time, therefore the neon content in the plasma (N_{Ne}) evaluated from *NeVIII* signal might be underestimated. This would mean on the other hand that more neon might be present in lower ionization states, which might be reasonable to assume for this transient time. Due to the same arguments the pumping of neon by the ALT II limiter during this phase, which is assumed to be proportional to the *NeVIII* signal, might also be underestimated. In **phase II** the neon concentration in the plasma has already been built up. $\tau^*_{p,Ne}$ ***increases with a smaller slope than in phase I*** and is saturated in about 0.7 s (#68810). Taking into account that the plasma parameters and also ALT pumping do not change during this phase, the increase of $\tau^*_{p,Ne}$ in this phase can only reflect the temporal behaviour of the effective wall pumping, that means the wall pumping is saturated in a time scale of about (~ 0.7 s). In **phase III**, $\tau^*_{p,Ne}$ ***is constant, i.e. the wall pumping is saturated and the recycling is nearly unity.*** The neon pumping is completely determined by the ALT pump efficiency.

6.2.1.3 Effective wall pumping and global retention of neon

Separating the ALT pumping rate (P_{ALT}) and the effective wall pumping (P^*_{wall}), the one dimensional particle balance equation Eq. (6-1) can be written as

$$\frac{dN_{Ne}}{dt} = \Gamma_i - \Gamma_o \tag{6-7}$$

$$= (\Gamma_{ext,Ne} + R_{Ne}\Gamma_o) - (\Gamma_{wall} + P_{ALT})$$

$$= \Gamma_{ext,Ne} - P^*_{wall} - P_{ALT} \tag{6-8}$$

where Γ_{wall} is outgoing flux to the wall and dN_{Ne}/dt will be called P_{plasma} in this work. Using the fact that P_{ALT} is proportional to N_{Ne}, P^*_{wall} can be described as a function of time:

$$P^*_{wall}(t) = \Gamma_{ext,Ne} - P_{ALT} - \frac{dN_{Ne}}{dt} \tag{6-9}$$

$$= \Gamma_{ext,Ne} - C_{Ne} NeVIII - M_{Ne} \frac{dNeVIII}{dt} \tag{6-10}$$

where C_{Ne} can be derived from ratio of $\frac{\Gamma_{ext,Ne}}{NeVIII}$ in the steady state phase of a reference discharge and M_{Ne} is the calibration factor of *NeVIII* to determine N_{Ne} as described in the previous section.

Fig. 6-5 shows quantitatively how P^*_{wall}, P_{ALT} and P_{plasma} vary, which was assumed in the previous section, as a function of time under different ALT pump conditions: (a), (c) with all ALT pumps open and (b), (d) with all ALT pumps closed. Fig. 6-5(a), (b) show the pumping rates of P^*_{wall}, P_{ALT} and P_{plasma}, and fig. 6-5(c), (d) show the integrations of them. The dip at ($2 < t < 2.5$ s) in Fig. 6-5(a) is due to the helium injection, which is not important here and can be neglected in this consideration.

In phase I of fig. 6-5(a) and (b), it is of no doubt that most of seeded neon builds up the neon concentration in the plasma (P_{plasma}). The external pumping by the ALT II limiter (P_{ALT}), even with all ALT pumps opened, plays in this phase only a minor role. The wall sink (P^*_{wall}), as discussed in the previous section, increases rapidly with the increasing neon concentration in the plasma and plays in this region, though small, an increasing role. The integral curves, which represents the absolute amount of neon in the plasma, in fig. 6-5(c) and (d) show this behaviour even more clearly: ***most neon seeded is contributed to build up the neon concentration in plasma***, which amounts to ~ 4×10^{18} and is independent of ALT pump

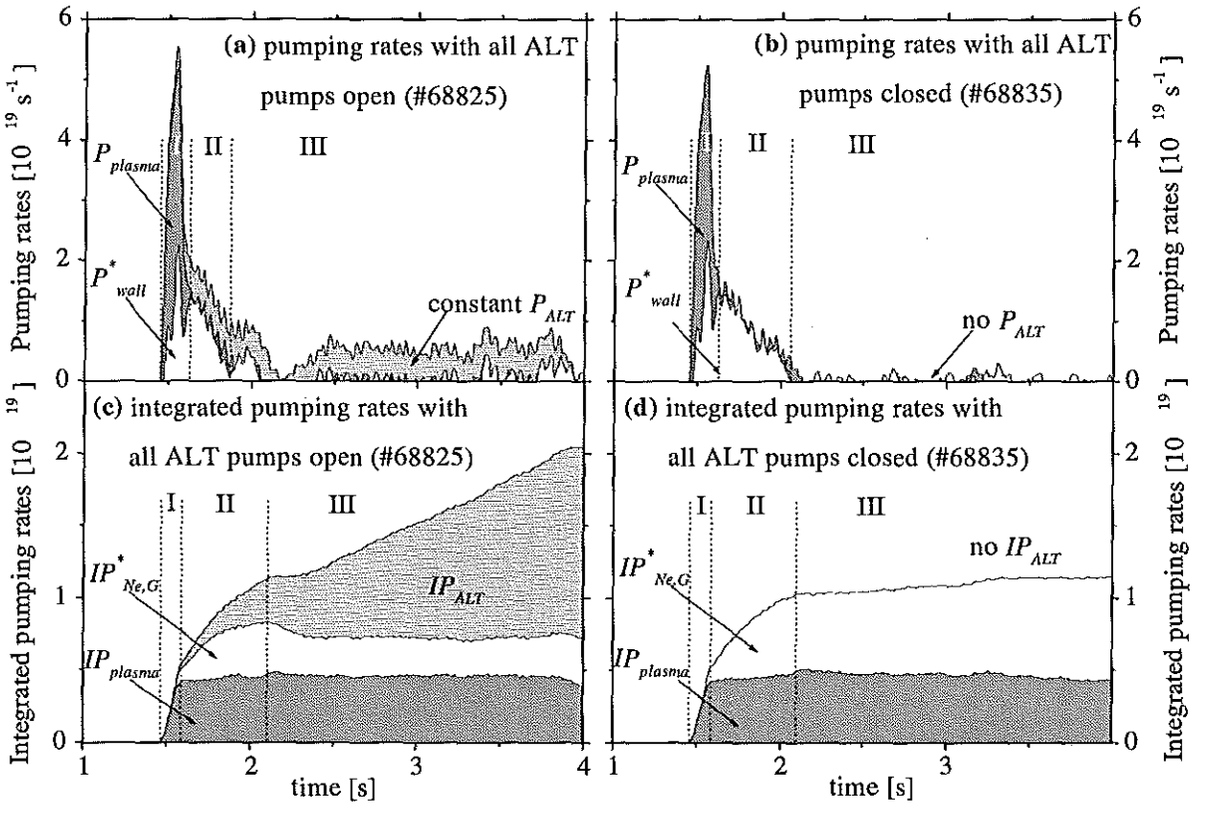

Figure 6-5 : Comparison of dynamic pumping behaviour of neon under different ALT pumping conditions (**top:** pumping rates (plasma pumping rate (P_{plasma}), ALT pumping rate (P_{ALT}) and effective wall pumping rate (P^*_{wall})), **bottom:** total amount of pumped neon, i.e. integrations of each pumping rate) ((**a**),(**c**) with all ALT pumps open and (**b**),(**d**) with all ALT pumps closed).

conditions. **In phase II**, the contribution of P_{plasma} is zero since the neon concentration in plasma is already saturated. P_{ALT} has, as shown in fig. 6-5(a), saturated at the end of the phase I and is constant during the rest of neon-injection period (phase II and III). This is also seen in Fig. 6-5(c) from the constant rise of IP_{ALT} (the plateau at $2 < t < 2.5$ is due to additional He-injection and should be neglected). The wall pumping P^*_{wall} reaches it's maximum after about 100 ms and decreases then to zero after about half a second, implying the saturation of neon retention in the wall. Fig. 6-5(c), (d) shows the ***saturation of the neon wall pumping rate*** P^*_{wall}, and its integral amounts to about ~ 3.6×10^{18}. In **phase III**, the neon is pumped out only by the ALT pumping. This can be seen most clearly from the fact that there is little or practically no pumping when all ALT pumps are closed (see fig. 6-5(b), (d)).

Fig. 6-6(a) shows the dependence of the integration of P^*_{wall} ($IP^*_{wall} = IP^*_{Ne,G}$) on n_e and γ: $IP^*_{Ne,G}$ ***decreases with increasing*** n_e ***and with decreasing*** γ. This is analogous to the behaviour of N_{Ne} in fig. 6-3(a), however the decrease of $IP^*_{Ne,G}$ with increasing n_e is much greater than that of N_{Ne}. Fig. 6-6 (b) shows it more clearly for the discharges with comparable γ ~ 0.5: while IP_{plasma} and IP_{ALT} decrease 2 - 4 times with n_e from 4 to 6×10^{19} m^{-3}, $IP^*_{Ne,G}$ ***decreases by more than a factor of 10***. This can be explained by two aspects: at **first**, since the energy of neon ions decreases with increasing n_e [Sch98,Unt98], the retention coefficient of neon decreases. **Secondly**, N_{Ne} decreases with the increase of n_e, as shown in Fig. 6-3(b), in

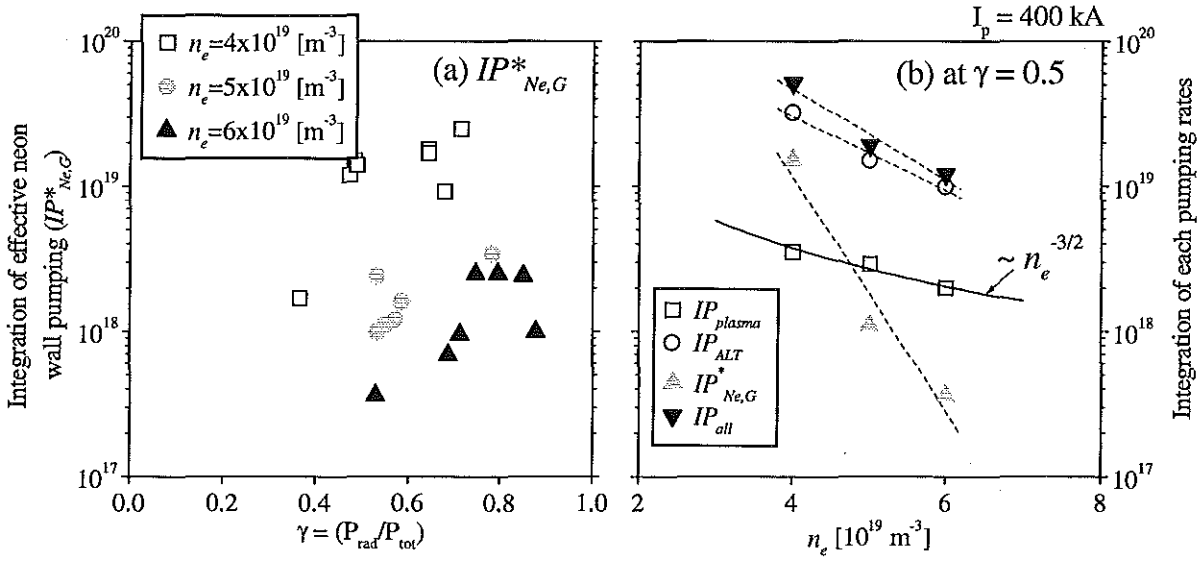

Figure 6-6 : **(a)** Integration of effective wall pumping rates ($IP^*_{Ne,G}$) under various $\bar{n}_e$ and γ, **(b)** dependence of the integrated pumping rates (IP_{plasma}, IP_{ALT}, $IP^*_{Ne,G}$ and IP_{all}) on the averaged electron density (n_e) for similar radiation levels γ (~ 0.5) (dashed lines in (b) are just guiding lines).

addition the hydrogen flux to the walls increases also with increasing n_e, which results in a **increase of the *'ion induced release of neon'*** by hydrogen ions. Synergistically, these two effects lead to a drastic decrease of the neon wall pumping $IP^*_{Ne,G}$ with increasing n_e. It should be noted here that the variation of the ALT pump conditions does not influence $IP^*_{Ne,G}$. Assuming that the total impurity density does not change significantly, the total density of impurity is proportional to $n_e^{-3/2}$ [Tok94], which is relatively in good agreement with the total number of neon in plasma (IP_{plasma}) (fig. 6-6(b)). Assuming that most of the neon retention occurs in the ALT II limiter and dividing the total amount of neon retention ($IP^*_{Ne,G}$) by the surface area of the total ALT II limiter (3.5 m^2), the retention density of neon ($R_{Ne,G}$) is obtained. The dependence of $R_{Ne,G}$ on n_e and γ will be compared with the results of Sniffer probe experiment in section 6.1.2.2.

6.2.1.4 Memory effect

When the former discharges are with neon-injection, a small background of neon is observed in the plasma even without neon-injection. The remaining neon in the first walls, which is not fully released after the former discharge, is released by the energetic ion impact during the discharge. The same behaviour is also observed by the Sniffer probe.

Fig. 6-7(b) (magnified from fig. 6-7(a)) shows the evolution of the neon background in the plasma before the neon-injection during repetitive neon-injection discharges. *Just after a glow discharge in helium or also after a disruption, the background neon signal is very low*, as seen from the curve ① (#78976 : two former discharges are disruptions). After a discharge with neon-injection, the background neon signal in the plasma (*NeVIII*) is well above that without previous neon-injection. Furthermore *the background of neon increases, as the discharges with neon-injection are repeated*: as seen on the traces ② - ⑤ of the *NeVIII* signal (curve ② (#78970 : after many neon discharges but only one former discharge is without neon-injection), ③ (#78971: *two* former discharges are with neon-injection), ④ (#78972 : *three* former discharges are with neon-injection), ⑤ (#78973 : *four* former discharges are with neon-injection). It is however not yet clear and should be investigated in more detail whether this background further increases or is saturated at a certain value. From the Eq. 6-5 the background neon curve ② amounts to 1×10^{17} and reaches about 2 % of the neon during the neon-injection of 5×10^{18} (see ② in fig 6-7(a), #78970 (n_e = 5.8×10^{19} m^{-3}, P_{tot} = 3 MW, γ = 0.7)). It is observed that the neon background increases, when the additional heating is increased (NBI and ICRH) (see fig. 6-7(b)). This is due to the enhanced ion energy of plasma particles hitting the wall components.

The memory effect can also be shown by analysing the neon seeding rate. Just after a glow discharge or a disruption more neon is seeded (2.6×10^{20}, #78967) than after discharges

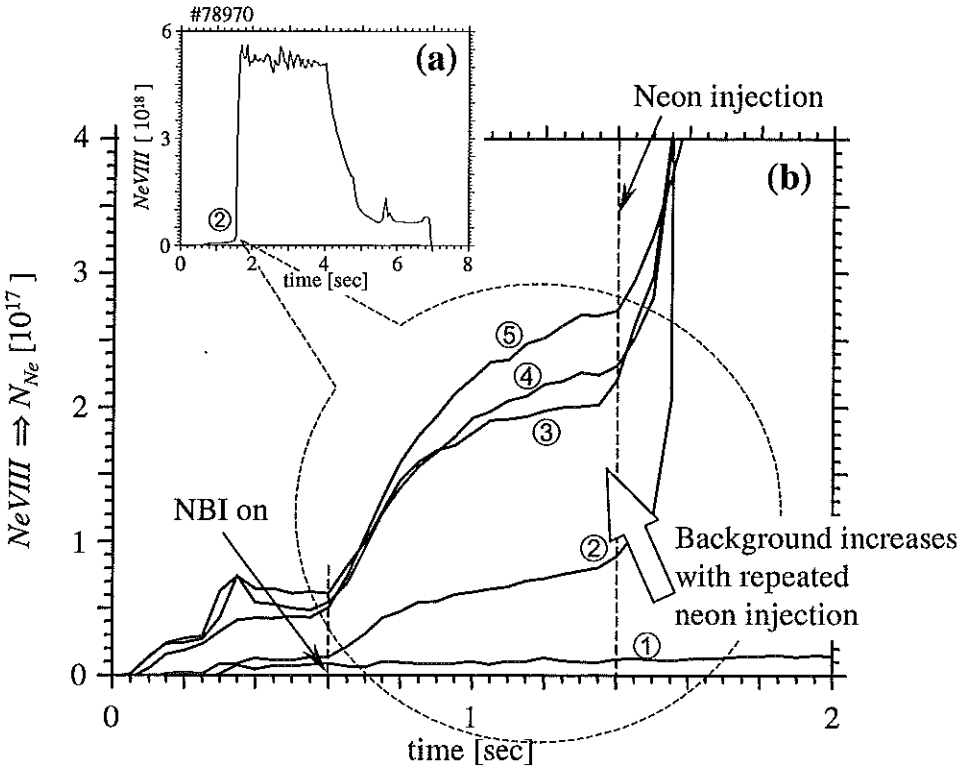

Figure 6-7 : Memory effect observed in the start phase of discharges **(a)** *NeVIII* in great time scale with neon-injection at t = 1.4 s, **(b)** in smaller time scale: ① (#78976 : after two disruptions), ② (#78970 : after many neon shots but *one* former shot is without neon injection), ③ (#78971 : *two* former shots are with neon injection), ④ (#78972 : *three* former shots are with neon injection), ⑤ (#78973 : *four* former shots are with neon injection).

with neon-injection (2×10^{20}, #78966) but otherwise under the same conditions ($n_e = 5.8\times10^{19}$ m^{-3}, $P_{tot} = 3$ MW, $\gamma = 0.7$). It has been found that this discrepancy is due to the different neon seeding rates only during the early phase (~ 600 ms) of the neon-injection (#78967 : 4.7×10^{20} s^{-1}, #78966 : 2.7×10^{20} s^{-1}), and the neon seeding rates are same during the rest of injection period. Granting that the amount of neon in the plasma, thus also ALT pumping, of two discharges are identical; this discrepancy above can only imply the different wall pumping rates due to the different conditions of pre-discharges.

6.2.2 *Sniffer probe measurement*

The global recycling and retention behaviour of neon derived in the previous sections are only based on phenomena averaged over all the wall and limiter areas. It is therefore desirable to analyse the retention of neon under well defined flux and surface conditions and to compare those data with the global observations. In this section, experiments done with the Sniffer probe will be described which were performed under well defined impinging neon and hydrogen fluxes. The experimental set-up of Sniffer probe has already been described in section 4.2.

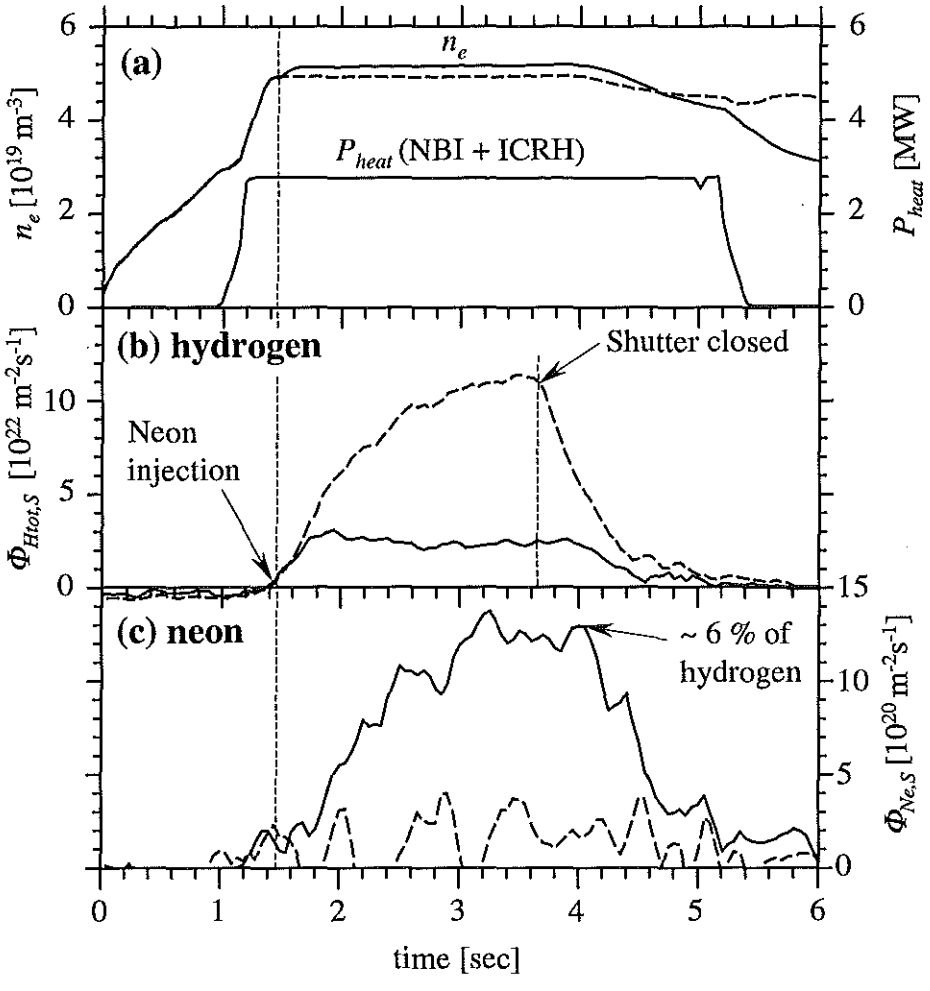

Figure 6-8 : Typical signals of TEXTOR-94 discharge (same discharges as in fig. 6-1; solid line: with neon-injection (#68810), dashed line: without neon-injection (#68812)) and ion fluxes measured by the Sniffer probe: **(a)** line averaged electron density (n_e), heating power (P_{heat}), **(b)** hydrogen flux ($\Phi_{Htot,S}$) and **(c)** neon flux ($\Phi_{Ne,S}$).

Fig. 6-8 shows some typical TEXTOR signals during RI-mode discharges (see 4.2.1) and the corresponding hydrogen and neon fluxes measured by the Sniffer probe. In this series of discharges the position of Sniffer probe was at r = 0.49 m, i.e. 0.03 m behind the LCFS. In order to point out the effect of neon seeding, each signals are depicted with (solid line) and without (dashed line) neon seeding otherwise under identical discharge conditions. One of the most striking observations is that ***with the injection of neon*** (at t = 1.46 s) ***the hydrogen flux*** ($\Phi_{Htot,S}$) ***decreases significantly***. Despite a valid increase of the line averaged electron density n_e in fig 6-8(a), a similar decrease of the hydrogen flux is observed on the ALT limiter (r = 0.46 m) as well as on the poloidal limiters (r = 0.49 m) by means of H_α emission spectroscopy. The flux ratio of hydrogen and neon measured by Sniffer probe reaches about 6 % for this discharge (#68810) and can reach up to 30 % at low n_e and high γ (see fig 6-10(c)). This will be more discussed in the following section.

The figure shows also a sudden decrease of $\Phi_{Htot,S}$ and $\Phi_{Ne,S}$ at t = 3.5 s, which is due to the closing of the shutter behind the aperture of the Sniffer probe. This allows a time-controlled exposure of the graphite sample to the impinging hydrogen and neon (see 4.2.2). The neon flux, as shown in fig. 6-8(c), has some background when the former discharges are with neon-injection. This ***'memory effect'*** has already been discussed in the previous section.

The amount of retained particles in the graphite sample of the Sniffer probe was measured by **T**hermal **D**esorption **S**pectroscopy (TDS, see 4.1.3). Fig. 6-9 shows examples of the desorption spectra of neon and hydrogen measured in the residual gas by the mass spectrometer. The sample was heated by direct current up to the temperature of about 1900 K with a ramp rate of ~ 120 K/s. The hydrogen release shown in this figure is, as explained in 4.2.3.1, the summation of all hydrogen isotopes (m/e = 2, 3, 4). Fig. 6-9(a) shows that less hydrogen is retained with neon-injection compared with the discharge without neon. This is due to the decreased hydrogen flux, as shown in fig. 6-8(b), with neon-injection. The hydrogen release shows a broad desorption spectrum with a maximum temperature at about 1400 K. This is comparable to earlier measurements in the Sniffer probe [Phi87] and also to results in other literature, e.g. maximum temperature at about 1000 K (heating rate : ~ 7 K/s) by Hansali et al. [Han90]. The ratio of the impinging hydrogen fluence to the desorbed and thus retained hydrogen ranges from ~ 15 % at low n_e (4×10^{19} m^{-3}) to ~ 3 % at high n_e (6×10^{19} m^{-3}). This is mainly due to the increased hydrogen fluence at higher density (the exposure time is always identical) and also partly due to the increased particle energy at lower plasma density [Sch98,Unt98]. The retention ratio and the absolute amount of hydrogen retention are in good agreement with model calculation of TRIM [Wam81] and will be discussed in 6.3.3 in more detail. The desorption of neon occurs at lower temperature than that of hydrogen and is very similar to that of hydrocarbons (methane) and CO. The maximum temperature is at about 1200K, which is much higher than that observed in the ion beam experiments (780 K, heating rate 11.5 K/s) in 3.1.2 due to the much higher heating rate in the Sniffer probe experiments (~ 120 K/s).

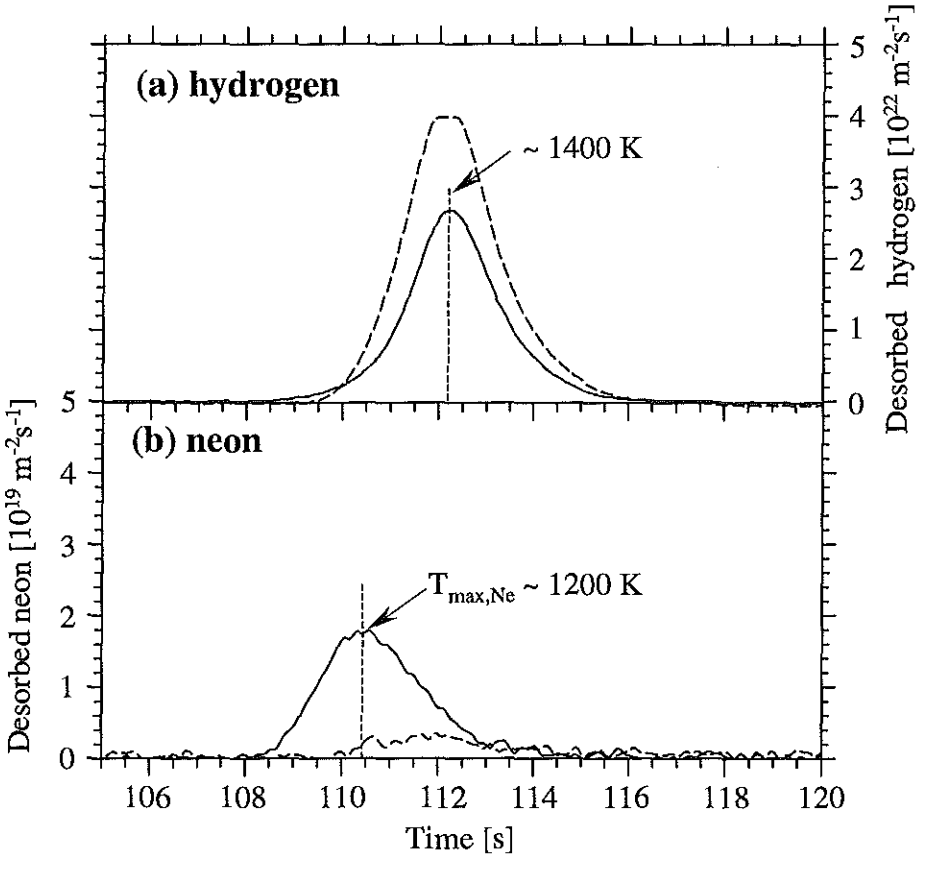

Figure 6-9 : Thermal Desorption Spectroscopy signals of hydrogen and neon from the Sniffer probe samples exposed to TEXTOR plasma for ~ 3 s (solid line: with neon-injection (#68769), dashed line: without neon-injection (#68771)): **(a)** desorbed hydrogen and **(b)** desorbed neon.

6.2.2.1 Neon and hydrogen ion fluxes and neon concentration in the scrape off layer

The incident ion fluxes of neon and hydrogen measured by the Sniffer probe in the steady state phase of the discharge are shown in fig. 6-10. The incident neon flux ($\Phi_{Ne,S}$) increases with increasing γ and decreasing n_e, which is in accordance with the behaviour of N_{Ne} in 6.1.1.1. The hydrogen flux ($\Phi_{Htot,S}$) in fig. 6-10(b) decreases with increasing γ. As discussed e.g. by Weschenfelder et al. [WesB97], this is both due to the increasing dilution of the edge plasma by neon and particle confinement from the decrease of the edge electron temperature ($T_{e,edge}$). Fig. 6-10(c) shows the behaviour of the ratio of neon and hydrogen flux ($\Phi_{Ne,S}/\Phi_{Htot,S}$). At the highest densities (6×10^{19} m^{-3}) this flux ratio is about 5% but at low n_e (4×10^{19} m^{-3}) it reaches up to 30 % at high radiation levels γ.

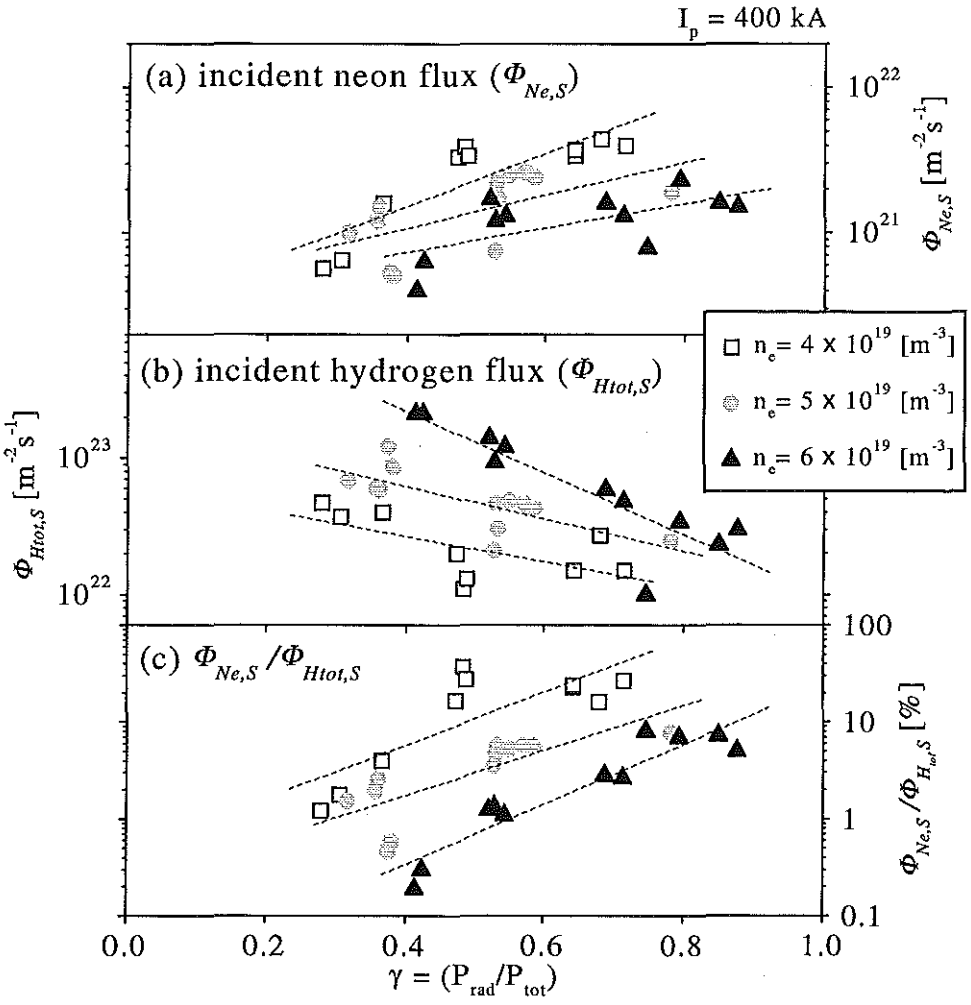

Figure 6-10 : (**a**) Incident ion flux of neon ($\Phi_{Ne,S}$), (**b**) hydrogen ($\Phi_{Htot,S}$) measured by Snifferprobe (R = 0.49 m) and (**c**) flux ratio them ($\Phi_{Ne,S}/\Phi_{Htot,S}$) under various n_e and γ.

From the flux ratios measured in the Sniffer probe the neon concentration at the plasma edge ($c_{Ne,S} = n_{Ne}/n_{e,tot}$) can be estimated: **first**, granting that the velocities of impurities are similar to the ion sound velocity of deuterium due to the friction forces in the scrape off layer, the neon flux ratio $\Phi_{Ne,S}/\Phi_{D,S}$ can be regarded as the density ratio (n_{Ne}/n_D) [Tok94,Unt97]. **Second**, multiplying this ratio by the deuterium concentration ($c_D = n_D/n_{e,tot}$) measured by emission spectroscopy at the ALT II limiter (at r = 0.46 m) [WesB97,Unt97], the neon concentration at the plasma edge ($c_{Ne,S}$) can be deduced. In fig. 6-11 the neon concentrations determined in this way are compared with results of other methods: $c_{Ne,LIM}$ is the neon concentrations evaluated from emission spectroscopy at poloidal limiter (at r = 0.49 m), $c_{Ne,G}$ is the global neon concentration, averaged over the TEXTOR plasma evaluated from the calibrated *NeVIII* signal described in 6.1.1.1 and $c_{Ne,CXRS}$ is the neon concentration at the plasma centre obtained by charge exchange recombination spectroscopy (CXRS) [Jas99]. All

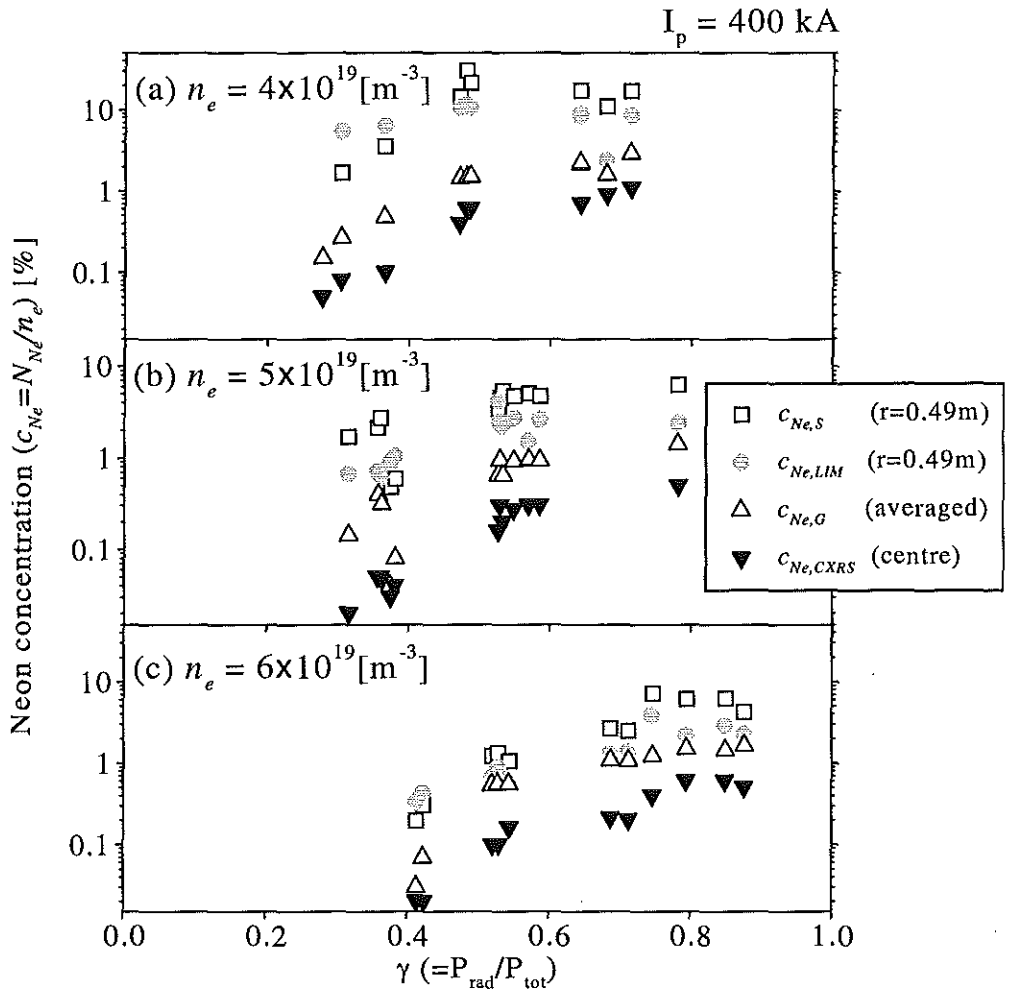

Figure 6-11 : Comparison of neon concentrations c_{Ne} (= $n_{Ne}/n_{e,tot}$) in the plasma measured by different methods and positions for different n_e ($c_{Ne,S}$: by the Sniffer probe, $c_{Ne,LIM}$: from the emission spectroscopy at poloidal limiter, $c_{Ne,CXRS}$: by the charge exchange recombination spectroscopy and $c_{Ne,G}$: by the global neon concentrations) : **(a)** $n_e = 4\times10^{19}$ m^{-3}, **(b)** $n_e = 5\times10^{19}$ m^{-3} and **(c)** $n_e = 6\times10^{19}$ m^{-3}.

data in fig. 6-11 are taken from the identical discharges. As can be seen, the neon concentrations $c_{Ne,S}$ and $c_{Ne,LIM}$ at the same radial position are reasonably in good agreement. By the way the neon concentration at the plasma boundary is much higher than that at the plasma centre. This indicates that the radial concentration profile of neon is hollow-like. This is also deduced from a detailed analysis of CXRS measurements which shows that the neon concentration at r = 0.25 m is greater than that at the centre of plasma [Jas99].

6.2.2.2 Retention of neon in graphite sample in the Sniffer probe and comparison with global observations

A EK98 graphite sample in the Sniffer probe was exposed to SOL plasma. After the discharge the retained neon was determined by thermal desorption spectroscopy. Fig. 6-12 shows the amount of incident neon fluence together with the retained neon at various $\overline{n}_e$ and γ. The incident neon fluences range from 10^{21} to 10^{22} m^{-2} and the amount of retained neon ($R_{Ne,S}$) ranges from 10^{18} to 10^{20} m^{-2}. While the incident neon fluence shows the expected dependence on n_e, i.e. similar to the overall amount of neon in the plasma (N_{Ne} in fig. 6-3(b)); the amount of retained neon shows a large scattering. No clear systematics can be found in these data. The retention ratios of neon shown in fig. 6-12(c) behave in a similarly non-systematic way and are typically much less than 1 %.

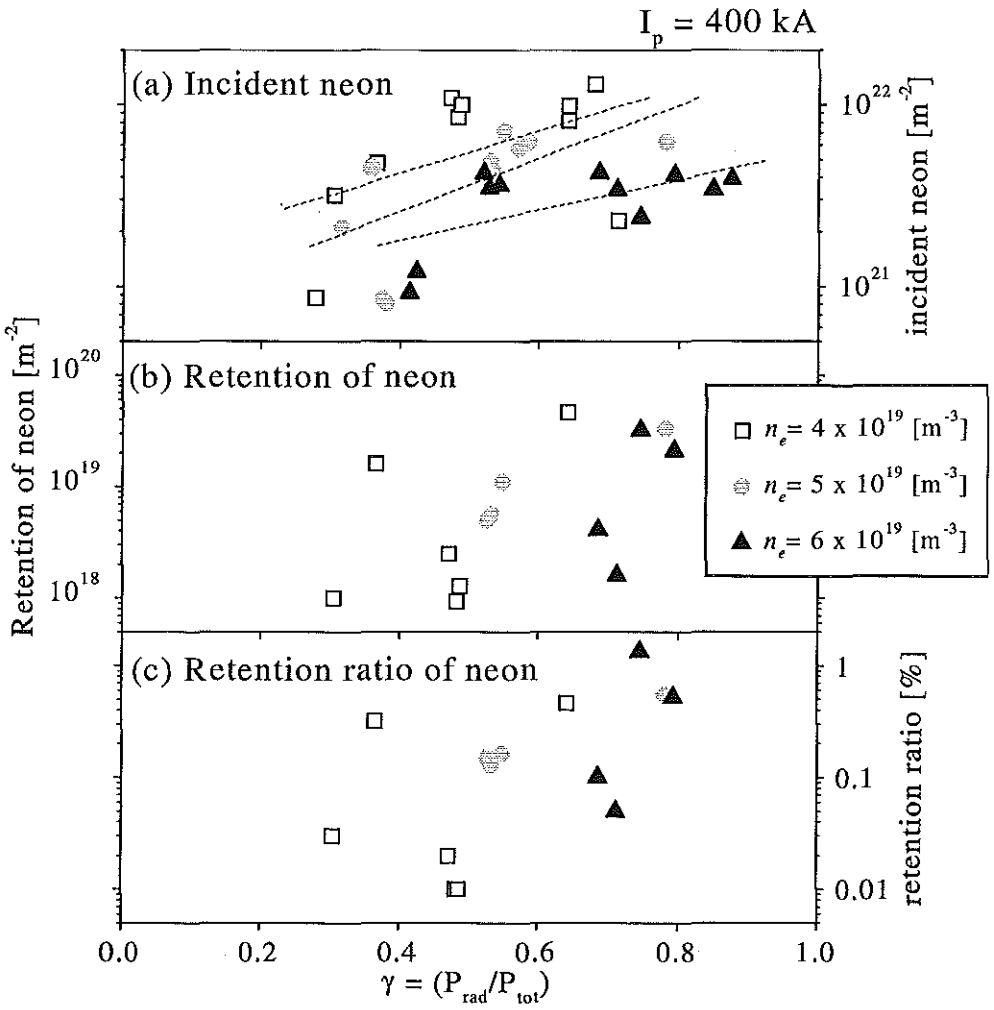

Figure 6-12 : **(a)** Number of incident neon during the discharge, **(b)** number of retained neon in graphite and **(c)** retention ration of neon under various n_e.

There are many discharges at which no retention of neon in graphite sample could be measured despite a significant flux of impinging neon during the discharge. The most probable reason for this behaviour is the rise of the sample temperature in the Sniffer probe at the end of some discharges probably due to unusual interferences. As an example, fig. 6-13(a) shows a usual discharge with neon-injection: during the discharge one can clearly see the neon ion flux together with CO formed by oxygen. After closing the shutter in front of the target, the signals decrease sharply. After the discharge neon is desorbed during the thermal desorption process (Fig. 6-13(a)). The desorption of CO occurs slightly at a higher temperature and shows two well separated peaks: first one is from the oxygen bonded to carbon and the second one is from the oxygen more strongly bonded to boron, oxygen released from these bonds reacts with carbon and leave the substrate as CO. This CO

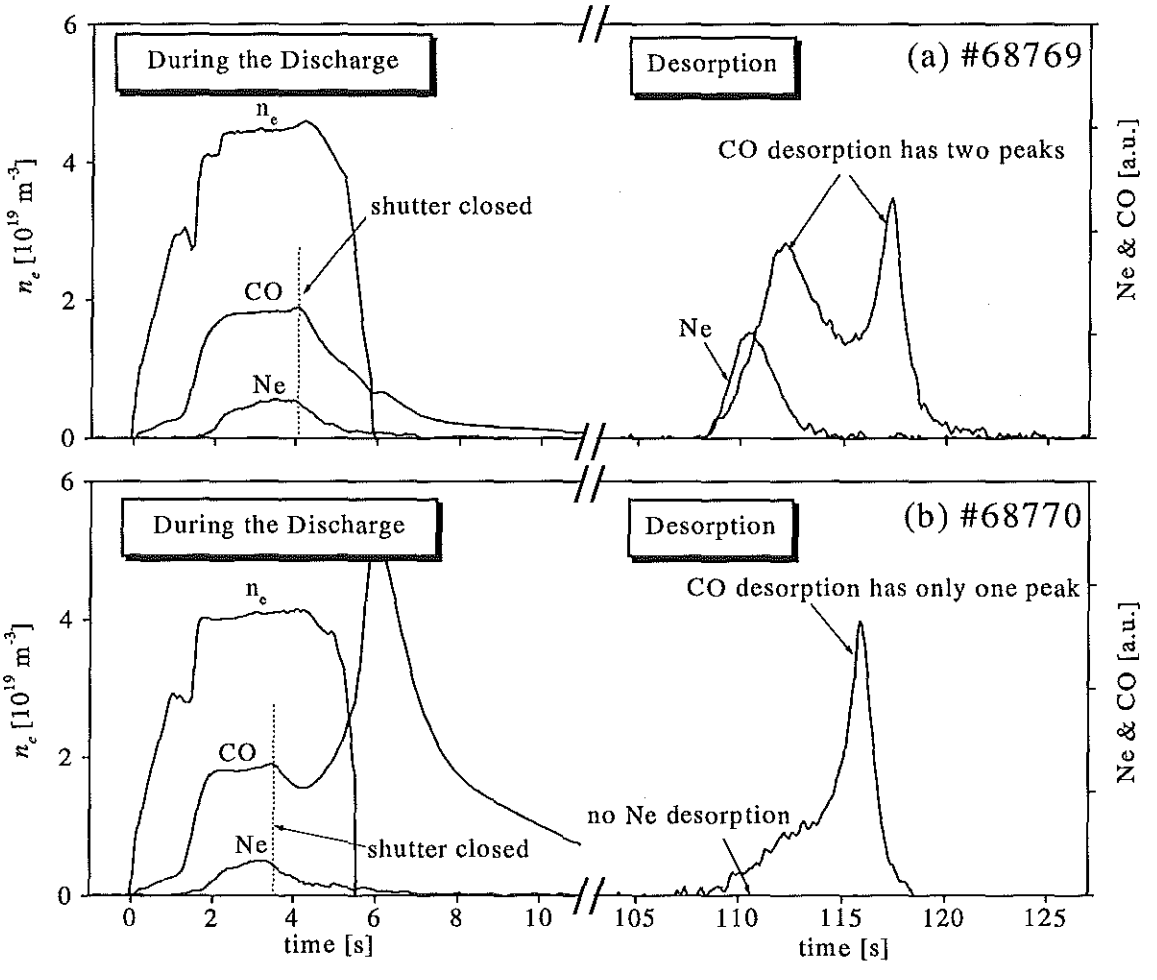

Figure 6-13 : Mass spectrometer signals of Ne and CO in the Sniffer probe during the discharge and subsequent thermal desorption in two shots with neon-injection under same condition: **(a)** usual case (one can measure thermal desorption of neon) **(b)** unusual case (at the end of discharge probe temperature rises abruptly and thermal desorption of neon is not measurable).

desorption has been discussed detailed by Refke et al. [Ref94]. If the desorption of CO in Fig. 6-13(b) is compared with that of (a), one can see that the first CO desorption peak has disappeared, indicating that most of the oxygen weakly bonded to carbon is already released at the end of discharge (see the rise of CO at the end of discharge in fig. 6-13(b)). This absence of the CO desorption falls together with the absence of neon desorption. It seems therefore reasonable to suppose that most of the neon retained in the graphite is already released at the end of the discharge. Thus, only such neon retentions are compiled where a neon (or the first CO peak) peak appears in the desorption spectra.

In Fig. 6-14, the retention density of neon in graphite sample measured by Sniffer probe ($R_{Ne,S}$) are compared with that by global observation ($R_{Ne,G}$). While at low n_e two results are relatively in good agreement, *at higher n_e the results from Sniffer probe* ($R_{Ne,S}$ ~10^{18} m^{-2}) is up to *one order of magnitude greater* than that from the global observation ($R_{Ne,G}$ ~10^{17} m^{-2}). One can suggest two explanations for this discrepancy: **first**, the graphite target in the *Sniffer probe* is placed *perpendicular to the magnetic field, ALT II limiter* is practically *parallel* to the magnetic field. The decrease of retention ratio with increasing incident angle is well known from the Monte Carlo calculation of TRIM. **Second,** since ALT II limiter (r = 0.46 m) is usually placed nearer to the plasma than Sniffer probe (r = 0.49 m), *the temperature of ALT II limiter (~ 600 K) is higher than that of Sniffer probe (< 500 K).* Therefore the retention ratio of neon in graphite in ALT II limiter is smaller than that of Sniffer probe. Ion beam experiment is supporting this assumption: observing fig. 4-4, the desorption of neon starts at

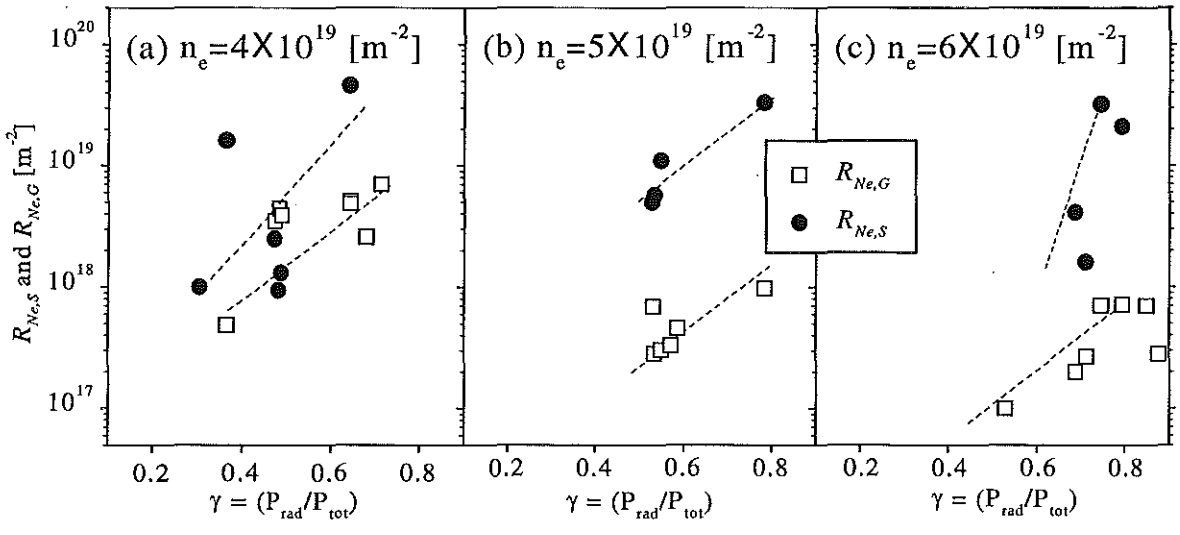

Figure 6-14 : Comparison of neon retention densities in graphite measured by global observations ($R_{Ne,G}$) and in the sample of the Sniffer probe ($R_{Ne,S}$) for different electron density n_e: **(a)** $n_e = 4\times10^{19}$ m^{-3}, **(b)** $n_e = 5\times10^{19}$ m^{-3} and **(c)** $n_e = 6\times10^{19}$ m^{-3}.

about 500 K and the retention of the irradiation 600 K is much smaller than that at 500 K due to the simultaneous reemission during the irradiation.

6.2.2.3 Comparison with the ion beam experiments

It is of great interest to compare the result of the ion beam experiments with that in the Sniffer probe and of the global observations on neon recycling and retention. Fig. 6-15 shows that the retention densities of neon measured in the Sniffer probe are more than one order of magnitude smaller than those by ion beam experiment.

In order to explain this discrepancy, we should take into account the different irradiation situations: while in ion beam experiment clean graphite probes were irradiated with pure neon ions, the majority of the impinging ions in the TEXTOR experiments were hydrogen ions (see fig. 6-10(c)). The effect of the simultaneous exposure of graphite with neon and hydrogen on the retention of neon has been investigated by Brosset et al. [Bro97]. Graphite was exposed to either a pure neon plasma, a mixed hydrogen and neon plasma or a hydrogen plasma after a exposure to a pure neon plasma. Under the latter two conditions the amount of desorbed neon was about one order of magnitude smaller than after the pure neon exposure. The authors of [Bro97] explain this behaviour that the main peak of neon desorption is from the formation of neon bubbles formed in graphite bulk, which do not form when the graphite is exposed to a

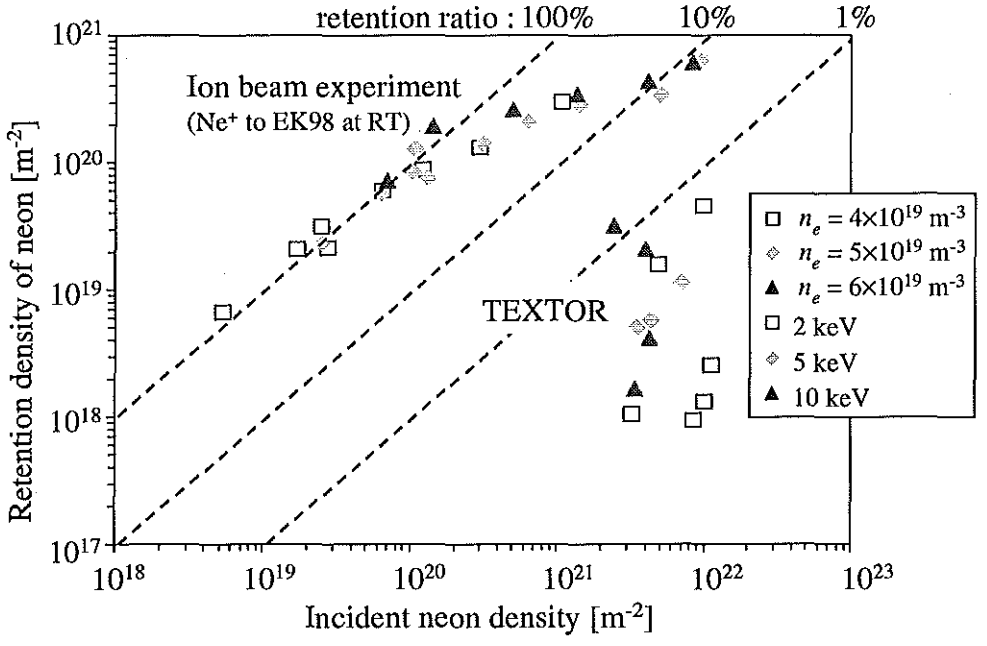

Figure 6-15 : Comparison of neon retention in graphite (ion beam experiment and Sniffer probe): ion beam experiment with 3 different ion energy (2, 5, 10 keV) and Sniffer probe at different n_e.

hydrogen plasma due to the *opening of the bubbles by hydrogen ion irradiation*. Bubble formation has been observed after irradiation of helium in many experiments [Ali95,Che96], which is very similar to that of neon in [Bro97]. However, the bubble formation of neon in graphite has not been directly measured and this "model" is thus very speculative.

6.2.3 Summary of the neon experiments in TEXTOR-94

From the overall balance of neon seeding and pumping, ***a new method to derive the absolute amount of neon in the plasma was developed***. From this particle balance ***the temporal behaviour of the effective particle confinement time and the absolute amount of dynamic retention of neon in the walls was deduced***. **In the first phase** of the neon-injection (~ 100 ms), the majority of the neon seeded contributes to build-up the neon concentration in the plasma (***plasma pumping***), although wall pumping begins to play a role. **In the second phase**, which lasts in TEXTOR about 600 ms, the neon concentration in the plasma is already in the steady state phase, but the ***wall pumping*** plays still an important role. It decreases however to zero due to the saturation of the neon retention in the walls. This wall pumping exceeds in this phase the neon pumping by the ALT pump limiter. This neon exhaust by the ALT pumps stays constant over the neon-injection phase (for constant density and radiation level) and is the only neon sink **for the rest of the neon seeding**. The outgassing of neon after the discharge is, though small, clearly to measure in the rasidual gas. A detailed investigation, which is not included in this thesis, should be done. The retention of neon in the walls can be seen from the fact that neon is released from the walls in the first discharge without neon seeding after discharges with neon seeding. This ***'memory effect'***, however, can only be seen for one or two discharges.

The absolute amount of neon and hydrogen ion fluxes were measured by the Sniffer probe and the amount of neon and hydrogen ***retention*** in the graphite probe was measured by thermal desorption spectroscopy. The hydrogen fluxes decreases significantly when neon is injected and the ***neon to hydrogen flux ratio*** extends from about 5 % at the high plasma densities (6×10^{19} m^{-3}) ***up to 30 %*** at low density (4×10^{19} m^{-3}). Large neon concentrations in the plasma edge are also observed by other methods (e.g. spectroscopy at the plasma edge). The comparison of the edge neon concentration with the overall neon concentration deduced by the particle balance and the central neon concentration measured by CRXS shows that radial profile of the ***neon concentration must be hollow-like. The retention density of neon measured with Sniffer probe is largely scattered***, which is most probably due to uncontrolled temperature excursions of the graphite probes by which part of the retained neon is already desorbed during the discharge. The available data however show that the absolute amount of neon retention can be about one order of magnitude larger than that deduced from global observations on neon recycling and retention and averaged over the surface area of the ALT limiter. ***But the retention of neon in graphite measured in the Sniffer probe is up to two***

order of magnitude smaller than that measured in ion beam experiment with pure neon ions and extrapolated to the conditions at the plasma edge. This difference is most probably due to ion induced release of neon by the majority of the hydrogen ions which impinge always simultaneously with the neon ions on the walls in a fusion experiment. The same behaviour has also been seen in other experiments comparing the neon retention in the walls in low energy pure neon plasma and in hydrogen-neon mixed plasmas.

6.3 Experimental Results for Argon

Argon was injected with feedback control in order to study the feasibility of argon as radiating element in TEXTOR-94. The amount of argon seeded was typically a factor of two smaller compared with that of neon. The plasma conditions were very similar to those of the RI-mode discharges with neon-injection [Ong97]. Fig. 6-16(a) shows typical signals of an RI-mode discharge with argon injection. Argon was injected at t = 1.44 s after the line averaged electron density n_e is nearly constant and under constant external heating of 1.06 MW NBI and of 1.44 MW ICRH. In comparison with the RI-mode discharges with neon-injection (see fig. 6-1), similar phenomena are observed: comparing the two discharges with (solid line, #70301) and without argon-injection (dashed line, #70302) but otherwise under the same plasma conditions (B_T = 2.23 T, I_p = 424 kA, P_{tot} = 2.8 MW), the argon seeded discharges requires little external hydrogen fuelling just after the argon-injection, whereas the discharge without argon-injection needs continuous gas feed in order to keep the desired density value.

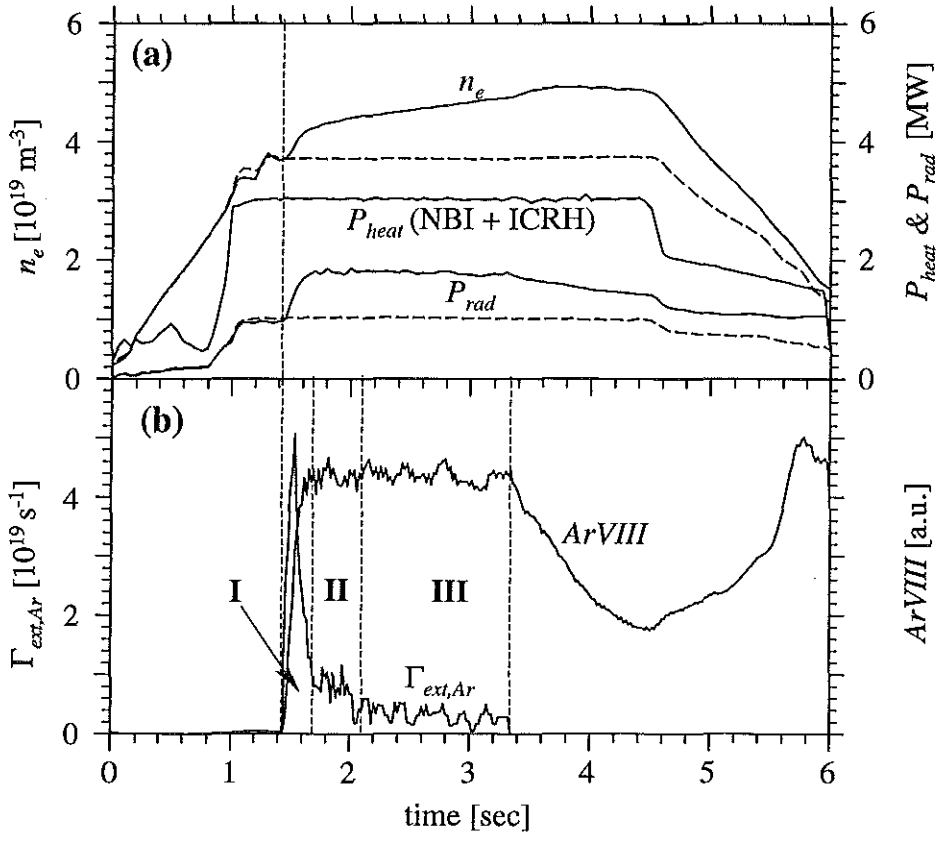

Figure 6-16 : Typical signals of TEXTOR-94 discharge (solid line: with argon injection (#70301), dashed line: without argon injection (#70302)) **(a)** line averaged electron density (n_e), total heating power (P_{tot}), and total radiation power (P_{rad}), **(b)** external argon seeding rate ($\Gamma_{ext,Ar}$) and line radiation of Na-like argon ions (*ArVIII*).

The improvement of the particle confinement with argon injection is indicated from the increase of n_e above the preset value. Fig. 6-16(a) demonstrates also ***the increase of the radiation (P_{rad})***, which leads to the decrease of the convective power on the plasma-facing components.

Fig. 6-16(b) shows the temporal behaviour of the line radiation of Na-like argon *ArVIII* together with the seeding rate of argon $\Gamma_{ext,Ar}$. The ArVIII signal can be assumed to be proportional to the total number of argon in the plasma under similar plasma density and temperature conditions, and is thus also used for the feedback control of the argon concentration in the plasma. Fig 6-16(b) shows a rapid rise of argon seeding rate followed by a steady state phase of the signal. It shows that the desired concentration of argon in the plasma is achieved ~ 300 ms after the argon-injection and stays then constant. This is somewhat slower than that of neon (~ 100 ms). Similar as the case of neon, $\Gamma_{ext,Ar}$ argon is further injected into the plasma despite the saturation of the argon concentration in plasma. Thus the argon injection and recycling can be divided into three phases: in **phase I** (t = 1.44 – 1.7 s), *most of the injected argon contributes to build up the desired argon concentration in the plasma* and a part of it is pumped by external pumps and the walls. In **phase II** (t = 1.7 – 2.1 s), argon is further injected but with a decreasing injection rate with no change of the argon concentration in the plasma. This can only be understood assuming that the majority of the argon is retained in the walls (***wall pumping***) during this phase. In **phase III** (t = 2.1 – 3.4 s) the argon injection rate $\Gamma_{ext,Ar}$ is nearly constant, with a rate, which is about 40 % of the neon seeding rate under similar conditions (see fig. 4-1(b)). From the steady state behaviour of the argon injection it can be reasonably assumed that the pumping in this phase is dominated by the ALT pumps.

6.3.1 Global observation

6.3.1.1 Total amount of argon in the plasma

Fig. 6-17 shows the total number of electrons ($n_{e,tot}$), the *ArVIII* signal and the external argon seeding rate ($\Gamma_{ext,Ar}$) at the end phases of the argon seeding under conditions with 7 ALT pumps open. Since the plasma conditions are nearly constant before and after the end of the argon injection, a one-dimensional particle balance equation ***delivers the total amount of argon in the plasma (N_{Ar})***:

$$\frac{dN_{Ar}}{dt} = \Gamma_i - \Gamma_o = (\Gamma_{ext,Ar} + R_{Ar}\Gamma_o) - \Gamma_o \qquad (6\text{-}11)$$

where Γ_i and Γ_o are the overall amount of incoming and outgoing argon fluxes. The incoming argon flux is given by the summation of external argon seeding rate $\Gamma_{ext,Ar}$ and the

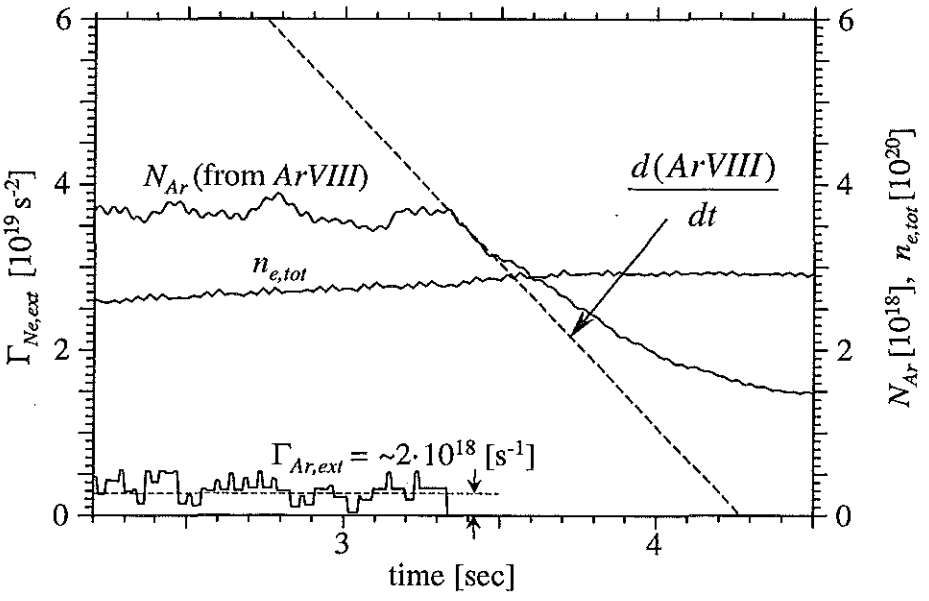

Figure 6-17 : Derivation of the amount of argon in the plasma (N_{Ar}) with 7 ALT pumps open (#70301) ($n_{e,tot}$: total number of electrons, $\Gamma_{Ar,ext}$: external argon seeding rate).

recycling flux of argon ($R_{Ar}\Gamma_o$, where R_{Ar} is the recycling coefficient of argon). Using the argon particle confinement time $\tau_{p,Ar}(=\frac{N_{Ar}}{\Gamma_o})$ and the effective confinement time $\tau^*_{p,Ar}(=\frac{\tau_{p,Ar}}{1-R_{Ar}})$ into Eq. (6-11), in the same way as in Eq. (6-2) – (6-4), the total number of argon N_{Ar} in the stationary phase of the discharge is given by the argon seeding rate $\Gamma_{ext,Ar}$ and the effective particle confinement time $\tau^*_{p,Ar}$ from Eq. (6-12),

$$\tau^*_{p,Ar} = -\frac{N_{Ar}}{\frac{dN_{Ar}}{dt}} = -\frac{ArVIII}{\frac{d(ArVIII)}{dt}} \qquad (6\text{-}12)$$

$$N_{Ar} = \tau^*_{p,Ar} \cdot \Gamma_{ext,Ar}. \qquad (6\text{-}13)$$

When the plasma conditions do not vary much, the *ArVIII* signal can be calibrated with this procedure and the temporal behaviour of the amount of argon in the plasma can be evaluated. (The calibration factor, e.g., $M_{Ar} = \frac{N_{Ar}}{ArVIII} = 9.57\times10^{17}$, for #78230 - #78335). The concentration of argon in the plasma ($c_{Ar,G} = N_{Ar}/n_{e,tot}$) is then derived from the total number of electrons ($n_{e,tot}$).

Fig. 6-18 compares the amount the argon seeded, the total number of argon in the plasma N_{Ar} and the its concentration $c_{Ar,G}$ with those for neon for comparable plasma conditions (n_e = 5×10^{19} m^{-3}, and I_p = 400 kA, see 4.2.1.1). It is remarkable that, **the total amount of argon and the concentration, derived in this way, are similar to those of neon**. Taking into account that the argon seeded is smaller than that of neon for the same radiation level γ in (a), this results show that the effective argon confinement time is larger. This will be quantitatively discussed in the following section in more detail.

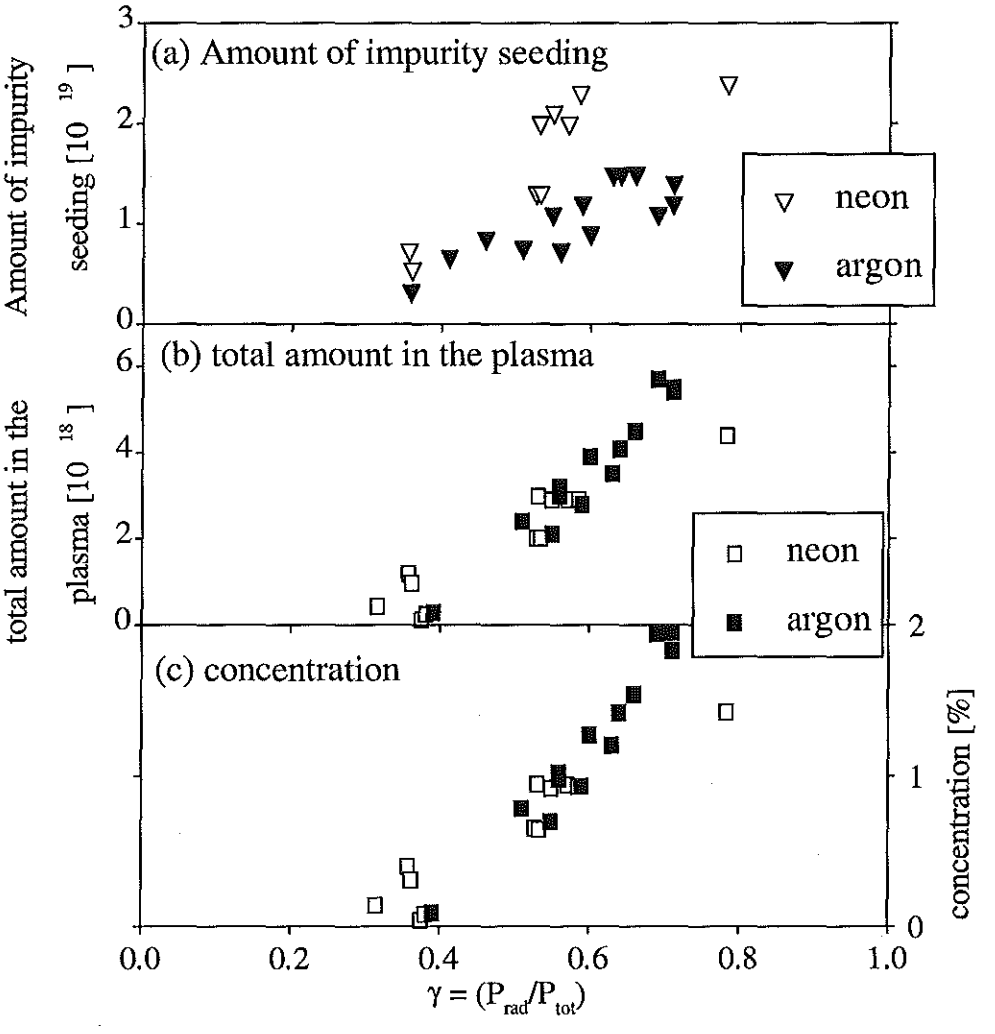

Figure 6-18 : Comparison of neon and argon for same plasma conditions (n_e = 5×10^{19} m^{-3} and I_p = 400 kA): **(a)** the amount of neon and argon seeding, **(b)** the total number of neon (N_{Ne}) and argon (N_{Ar}) in the total volume of TEXTOR plasma and **(c)** concentrations of neon ($c_{Ne} = N_{Ne}/n_{e,tot}$) and argon ($c_{Ar} = N_{Ar}/n_{e,tot}$).

It is interesting that, as I_p increases N_{Ar} and c_{Ar} slightly decreases for the same radiation level despite the larger argon seeding (no figure). This implies a decreasing effective particle confinement time of argon. This behaviour is thus opposite from that of deuterium for which

the particle confinement time usually increase with increasing plasma current. The change of the pumping behaviour of argon with increasing I_p, will be further discussed in 4.3.3.2.

6.3.1.2 Effective wall pumping and global retention of argon

In the same way as described is in 6.1.1.3, a one dimensional particle balance equation for argon Eq. (6-11) can be written assuming a ALT pumping rate (P_{ALT}) and an effective wall pumping rate (P^*_{wall}) for argon:

$$\frac{dN_{Ar}}{dt} = (\Gamma_{ext,Ar} + R_{Ar}\Gamma_o) - (\Gamma_{wall} + P_{ALT}) \tag{6-14}$$

$$= \Gamma_{ext,Ar} - P^*_{wall} - P_{ALT} \tag{6-15}$$

Using the total amount of argon N_A derived in Eq. (6-13) and taking into account that P_{ALT} is proportional to N_{Ar}, P^*_{wall} can be described as a function of time

$$P^*_{wall}(t) = \Gamma_{ext,Ar} - C_{Ar} ArVIII - M_{Ar} \frac{dArVIII}{dt} \tag{6-16}$$

where C_{Ar} is now derived from the ratio of $\frac{\Gamma_{ext,Ar}}{ArVIII}$ in steady state phase and M_{Ar} is the calibration factor of *ArVIII* as derived in the previous section.

Fig. 6-19 shows quantitatively the developments of the different pumping rates of P_{plasma}, P^*_{wall} and P_{ALT} as a function of time with 7 ALT pumps open (a) and in (b) the integrated amount of them. Similar to neon, **in phase I** of fig. 6-19(a) ***most of the argon seeded contribute to build the argon concentration in the plasma (P_{plasma}).*** The integral curves in Fig. 6-19(b) show that the number of argon in plasma amounts to ~ 3.5×10^{18}, which is similar to that of neon for comparable discharge conditions. It takes ~ 200 ms till the argon is built up. This time is much longer that the time needed for the argon to be transport into the plasma centre and is due to the feedback controlled ramp up of the argon line radiation. The external pumping by the ALT II limiter (P_{ALT}), can be assumed to be proportional to N_{Ar} and has already some influence. The wall pumping (P^*_{wall}), increases rapidly with increasing argon concentration and plays an increasing role. **In phase II**, the contribution of the plasma as sink for the argon P_{plasma} is zero since the argon concentration in the plasma is already saturated. The pumping by the ALT pump limiter P_{ALT} is constant during the rest of the argon-injection period (phase II and III). The wall pumping P^*_{wall} reaches it's maximum after about 200 ms and decreases then to zero after about half a second, implying the saturation of argon retention

in the wall. This is demonstrated also in Fig. 6-19(b) which shows the integrated amount of pumped argon. The ***saturation of the argon wall pumping rate*** P^*_{wall} can be seen and the saturation value represents the absolute amount of retained argon, which amounts to about 7×10^{18}. This is about a factor of two larger than that of a comparable neon discharge (~ 4×10^{18}, see fig. 6-5(c)). Taking into account that the amount of argon injection is about half of that of argon, the retention ratio of argon is much larger than that of neon. This will be further discussed in fig. 6-19. In **phase III**, it is assumed that ***argon is pumped out only by the ALT pumping***. This assumption is strongly suggested from Fig. 6-19(b) which shows that the wall pumping and the plasma fuelling IP^*_{wall} and IP_{plasma} have saturated and only the ALT pumps act as a sink for the argon.

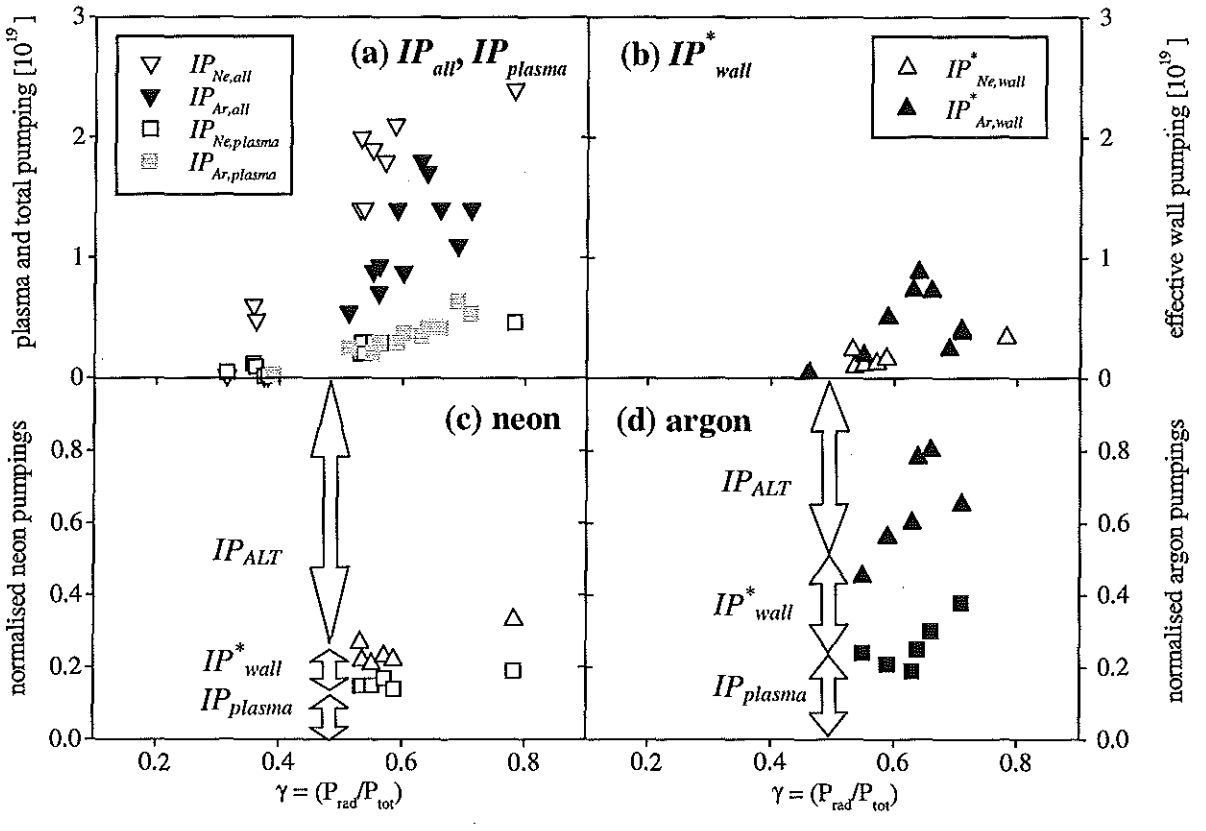

Figure 6-19 : Comparison of the pumping behaviours of neon and argon **(a)** plasma pumping (IP_{plasma}) and total pumping (IP_{all}), **(b)** effective wall pumping (IP^*_{wall}), **(c)** normalised pumpings of neon and **(d)** argon.

Fig. 6-19 compares the amount of neon and argon in the plasma (P_{plasma}) and the effective wall pumping (P^*_{wall}) of argon and neon under similar discharge conditions. In fig. 6-19(a) the number of argon inside the plasma ($IP_{plasma,Ar}$), same as N_{Ar} in fig. 6-18(b), is similar to that of neon ($IP_{plasma,Ne}$). The amount of argon pumped by walls $IP^*_{wall,Ar}$ in (b) is larger than that of

neon ($IP^{*}_{wall,Ne}$). By normalising the integrated loss channels for the injected neon and argon at the end of the injection phase, as shown in fig. 6-19(c),(d), in can be better understood. For neon, (c), over 70 % of neon is pumped by ALT pumping and the remaining rest (up to 30 %) fuels the plasma or is pumped out by the walls. For neon the plasma pumping is slightly larger than the wall pumping which amounts only to about 15 % at maximum. For the argon case in fig. 6-19(d) however, the ALT pumping reaches only 20 – 50 % of the total seeding and 50 to 80 % of the argon seeded is in the plasma or pumped out by the walls. The wall pumping is larger than the plasma pumping and reaches up to 55 % of total loss rate. This fraction of wall pumping is thus much greater than in the case of neon. As for the neon case, the retention of argon is influenced by simultaneously incident hydrogen (*ion-induced release*). Recollecting that the retention ratio of argon measured in the ion beam experiments is smaller than that of neon, it can be speculated that the ion-induced release of argon by hydrogen ions is, due to the higher mass of argon, less effective. This will be discussed in connection with the Sniffer probe experiments in more detail.

The normalised values of the argon content in the plasma (IP_{plasma}), wall (IP^{*}_{wall}) and the amount pumped by the external pumps (IP_{ALT}) in fig. 6-19(d) show that 20 to 25 % of seeded argon stays in the plasma during the discharge. And about half of the argon seeded is pumped out by the walls (IP^{*}_{wall}) during the discharge. The remaining rest of the argon is pumped out by ALT pumping during the discharge. If we add the argon in the plasma and the wall, the maximum amount of argon, which can be measured after the end of the discharge, is given (***outgassing***). This value varies between 50 to 80 % of the total amount of argon seeded. This is much greater than that of neon (20 – 30 %, see fig. 6-19(c)). Table 6-2 summarises the contributions of the different loss channels of argon and the amount of the maximum possible outgassing for different γ. This will be compared with that measured from the outgassing in TEXTOR in the following section.

γ	low γ (~ 0.5)			high γ (~ 0.8)		
Normalised integrated pumping rates	IP_{plasma}	IP^{*}_{wall}	IP_{ALT}	IP_{plasma}	IP^{*}_{wall}	IP_{ALT}
During the discharge	20 %	30 %	50 %	25 %	55 %	20 %
Possible maximum outgassing	↘ ↙ **50 %**			↘ ↙ **80 %**		

Table 6-2 : Contribution of each pumping channels during the discharge and the possible maximum outgassing of argon after the discharge for different radiation level γ (n_e = 5×10^{19} m^{-3}, P_{tot} = 2.5 MW and I_p = 400 kA).

Assuming that the argon is retained in the ALT II limiter and dividing the total amount of argon retention (IP^{*}_{wall}) by the surface area of the total ALT-II limiter (3.5 m^2), the retention density of argon ($R_{Ar,G}$) is obtained. The dependence of $R_{Ar,G}$ on n_e and γ will be compared with the results of the Sniffer probe experiment in the following section.

6.3.1.3 Outgassing of argon after discharge

Fig. 6-20(a) shows the typical time evolution of the argon and hydrogenic partial pressure (HD: m/e = 3) after the discharge measured by a quadruple mass spectrometer. Both the hydrogenic pressure and the argon partial pressure rise sharply after the end of the discharge. As already discussed, this pressure rise is due to the continuous outgassing of hydrogen and

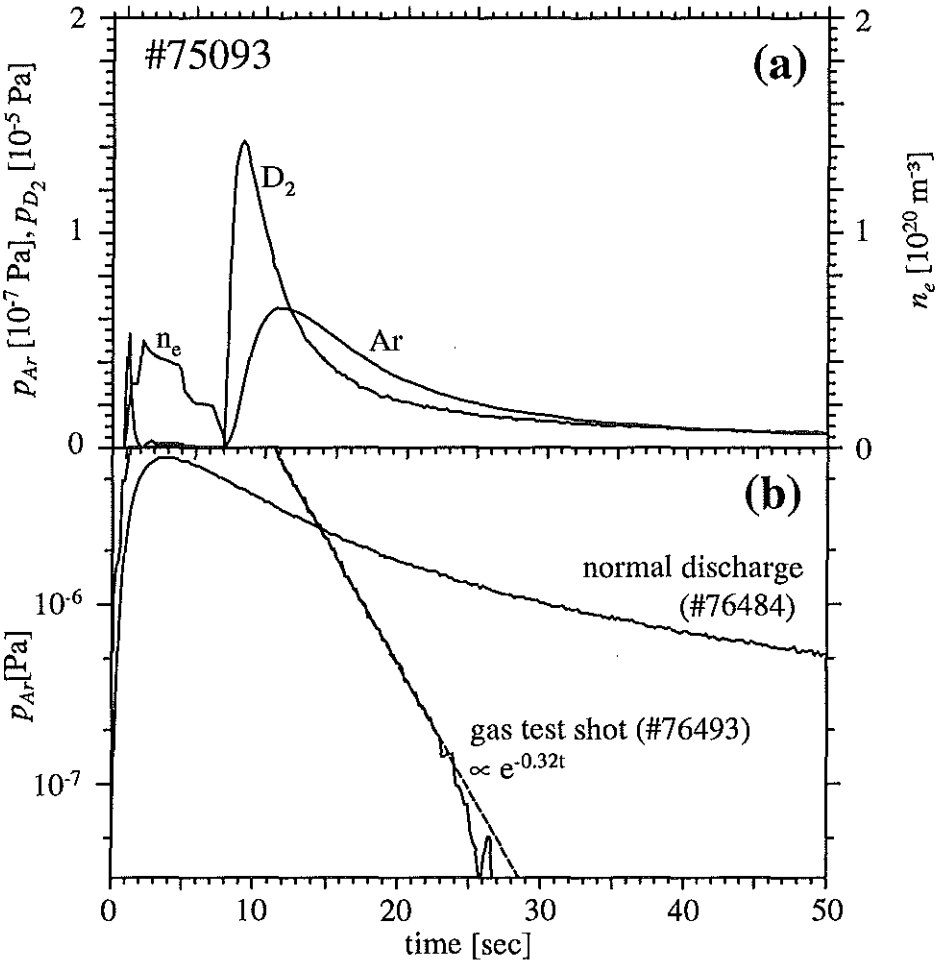

Figure 6-20 : **(a)** Typical time evolution of argon (p_{Ar}) and deuterium (p_{D_2}) partial pressure after RI-mode TEXTOR discharge (#76484) with argon injection and **(b)** comparison of the argon partial pressure (p_{Ar}) after a normal discharge (#78484) and after a gas test shot (#76493).

argon from the walls: with the termination of the plasma, the ionization of the outgassed neutrals by the plasma (*plasma pumping*) and the effective wall pumping cease and the neutrals can fill the TEXTOR volume resulting in the sharp rise of the neutral gas pressure. As can be seen directly in fig. 6-20(a), argon has a much longer outgassing tail than the hydrogen. Fig. 6-20(b) shows the time dependencies of the argon partial pressures after a discharge with argon injection (#76484, NBI = 1.48 MW, $\gamma = 0.42$) and a gas test shot with argon injection (#76493). As expected, the argon partial pressure after the gas test shot follows an exponential function ($\propto e^{-0.32t}$), from which the pumping speed for argon was derived: 5.4 m^3/sec (7 ALT-II pumps, main TEXTOR turbo pump and one neural beam injection duct open). After the discharge (#76484) with argon injection, however, a remarkably slower decay of the argon partial pressure is observed.

Considering the lower recycling ratio of argon (than neon) during the discharge and the slowly decaying partial pressure of argon after the discharge mentioned above, it is reasonable to assume that argon seeded is stored in the walls and then continuously released after the end of discharge with a slow release rate. In order to analyse the slowly decaying release rate of argon in more detail, the release rates of argon as a function of time have been derived from the partial pressure of argon (p_{Ar}) and the pumping power of TEXTOR for argon

$$Q_{Ar}(t) = \{\frac{dp_{Ar}(t)}{dt} \cdot V + p_{Ar}(t) \cdot S_{Ar}\} \cdot \frac{1}{RT} \qquad (6\text{-}17)$$

where V is the TEXTOR volume (= 17 m^3), S_{Ar} is the pumping speed of TEXTOR for argon (= 5.4 m^3/s) and $\frac{1}{RT} = \frac{273}{T_w} 2.64 \cdot 10^{20}$ $Pa^{-1}m^{-3}$. Fig. 6-21 shows the release rate of argon after a discharge with argon injection (#76484) in a log-log plot versus time. As can be seen, the release rate of argon can be fitted very well with a power law: $Q_{Ar}(t) \propto t^{-1.1}$. Though in fig. 6-21 the release rate is plotted only until t = 50 sec, this power law has been measured from the beginning of the outgassing till the beginning of next shot 300 sec. It is also relatively independent of the plasma conditions like the density or the quantity of argon seeding. Basically, the temporal behaviour of the release rate contains information about the physical mechanism of the outgassing processes [Doy82]. A possible explanation for the release process of argon will be given with that of xenon in 6.3.1.2.

The absolute amount of argon outgassing (#76484) has been evaluated by calibrating the mass spectrometer against the integral of the argon outgassing after the gas test shot (#76493). The amount of argon outgassed after the discharge, integrated from the end of the discharge till the start of the next discharge, was found to be 56 % of the amount of argon seeded (#76484, NBI = 1.48 MW, $\gamma = 0.42$). The outgassing of argon (56 %) is in reasonable agreement with the 50 % expected in the previous section for low γ (see table 6-2). This

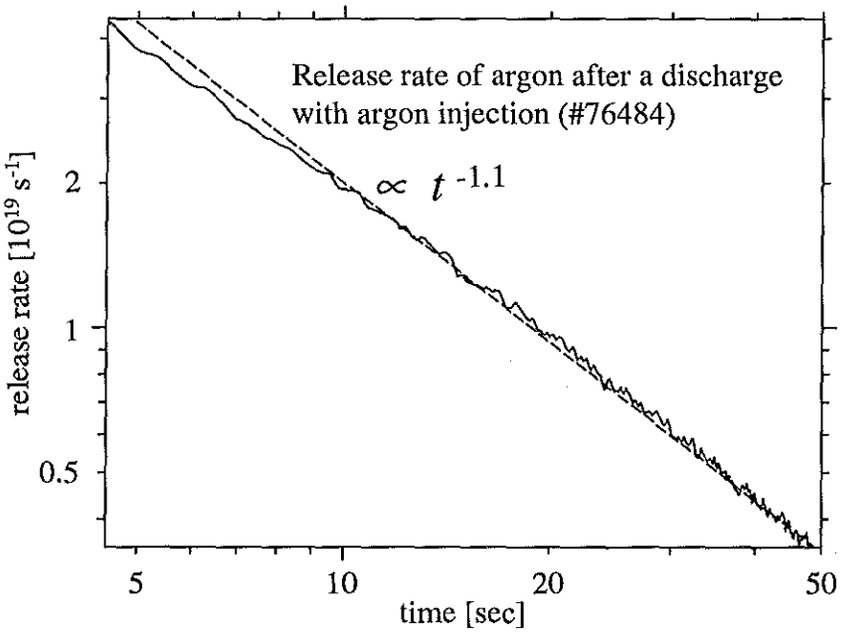

Figure 6-21 : Time evolution of the release rate of argon after a discharge with argon injection (#76484) (in log-log scale).

means, in other words, that most of the argon retained during the discharge in the walls is released slowly in between the discharge. Not all of the retained argon is released in this manner, which is seen from the fact that argon can be seen in the plasma, due to the particle induced release, with no argon injection but following a discharge with argon injection.

6.3.2 Sniffer probe measurement

The retention of argon from the global observation has been compared with that under better-defined incident ion flux and surface conditions in the Sniffer probe. This section compares the global observations with experiments done with the Sniffer probe and from ion beam experiments.

Fig. 6-22 shows some typical TEXTOR signals during RI-mode discharges and the corresponding hydrogen and argon fluxes measured by the Sniffer probe. In this series of discharges the position of Sniffer probe was at the same position as used for the neon experiments (r = 0.49 m, 3 cm behind the LCFS). In order to illustrate the effect of the argon seeding, each signal is shown with (solid line) and without (dashed line) argon seeding but

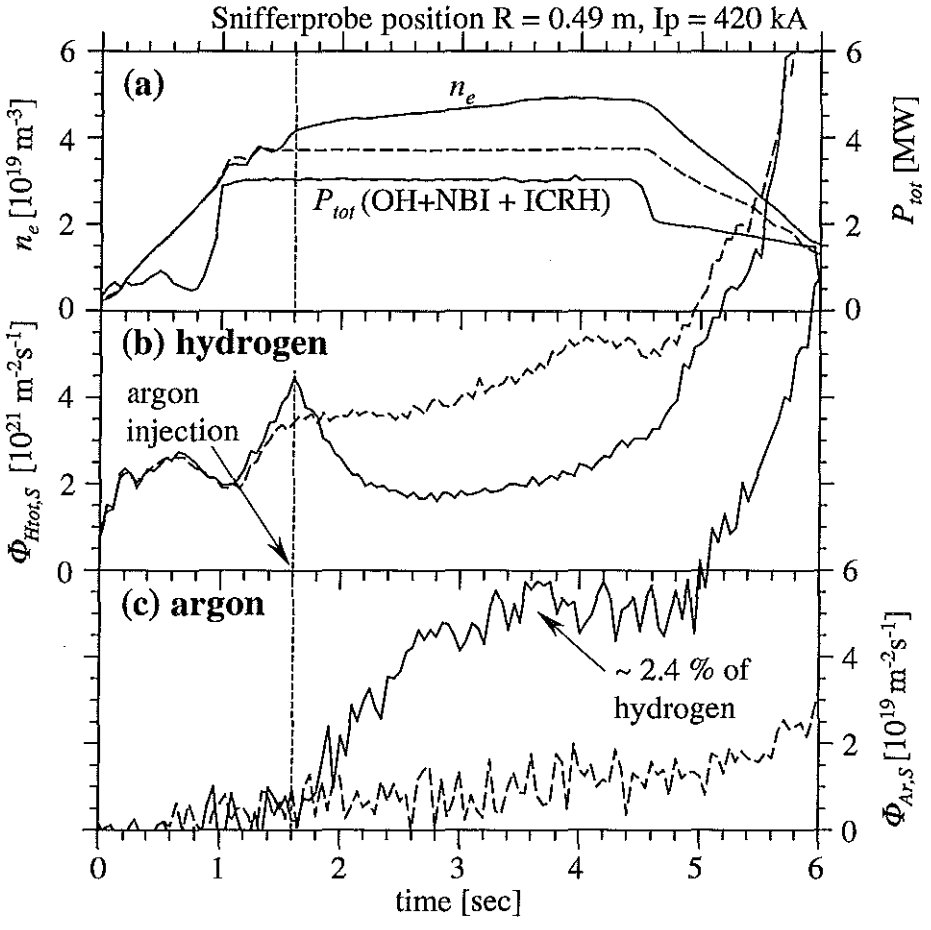

Figure 6-22 : Typical signals of TEXTOR-94 discharge (same discharges as in fig. 6-16; solid line: with neon (#70301, $\gamma = 0.63$), dashed line: without neon (#70302, $\gamma = 0.37$)) and ion fluxes measured by Sniffer probe: **(a)** line averaged electron density (n_e), heating power (P_{tot}), **(b)** hydrogen flux ($\Phi_{Htot,S}$) and **(c)** argon flux ($\Phi_{Ar,S}$).

under otherwise identical discharge conditions. Similar as observed for neon *the hydrogen flux ($\Phi_{Hlot,S}$) decreases significantly with the injection of argon* (at t = 1.6 s) despite a clear increase of the line averaged electron density n_e. This is, as already explained in 6.1.2.1, partly due to the dilution of the edge plasma and partly due to an increase of the particle confinement time due to the decrease of the edge electron temperature ($T_{e,edge}$). A similar decrease of the hydrogen flux is also observed on the ALT limiter (r = 0.46 m) by means of H_α emission spectroscopy. The flux ratio of hydrogen and argon in the flat top phase of the discharge measured by Sniffer probe reaches ~ 2 % for this discharge (#68810). Different from the neon experiments, the shutter behind the aperture of Sniffer probe in this series of discharges was always open during the discharges. Therefore there is no abrupt decrease of fluxes as in fig. 6-8. The increase of all fluxes at the end of the discharge is due to the decreasing particle confinement with decreasing plasma current. As was discussed for neon in 6.1.1.4, a ***'memory effect'*** for argon can be also observed by the Sniffer probe.

The amount of retained particles in the graphite probe of the Sniffer probe was measured by thermal desorption spectroscopy (see 2.1.1.6). Fig. 6-23 shows examples of the desorption

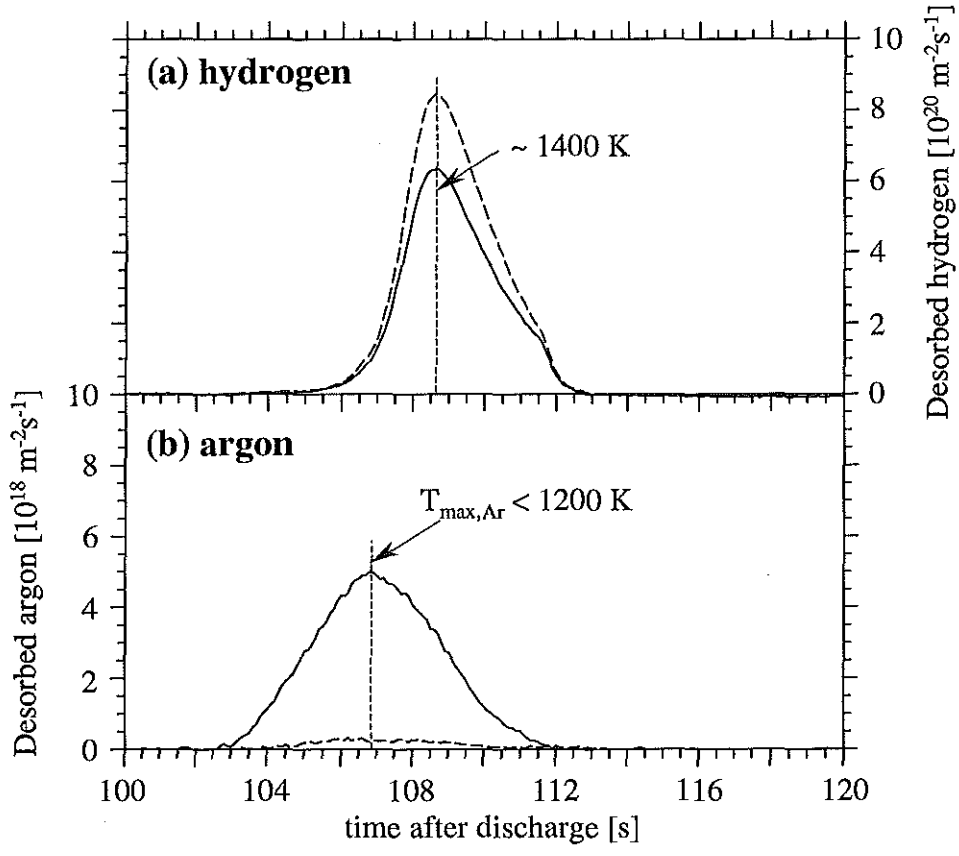

Figure 6-23 : Thermal Desorption Spectroscopy signals of hydrogen and argon from the Sniffer probe samples exposed to TEXTOR plasma for ~ 3 s (solid line: with argon injection (#70323), dashed line: without argon injection (#70322)): **(a)** desorbed hydrogen and **(b)** desorbed argon.

spectra of argon and hydrogen measured by the mass spectrometer. The sample was heated by direct current flow up to the temperature of about 1900 K with a ramp rate of ~ 120 K/s. The hydrogen release shown in this figure is obtained by the summation of all hydrogen isotopes (*m/e* = 2, 3, 4). The hydrogen release shows a broad temperature dependence with the maximum temperature at about ~1400 K. The desorption of argon occurs at a somewhat higher temperature than that of neon and has a broader temperature dependence. This is consistent to ion beam experiments (4.2.1) and other measurements [Cho93].

Fig. 6-23(a) shows also that less hydrogen is retained in a shot with argon injection compared with that without argon. This is due to the decreased amount of incident hydrogen with argon injection. We do not see any other effect of the argon or neon impurity seeding on the hydrogen retention behaviour. The atomic thermal helium beam diagnostic shows that the plasma edge temperatures ranges between T_e = 20 and 80 eV [Bri98,Sch98] and taking into account that $kT_i \sim 2 \cdot kT_e$ (see 2.1), the incident hydrogen energy onto the graphite target is estimated to 150 – 400 eV from Eq. 2-2 [Sta86]. Comparing the retention density of hydrogen measured by the Sniffer probe with that of deuterium with a Maxwellian velocity distribution incident on carbon calculated by TRIM [Wam81] in fig. 6-24, one sees that the measured hydrogen retention density would correspond to ion energies of (400 – 3200 eV). Part of the

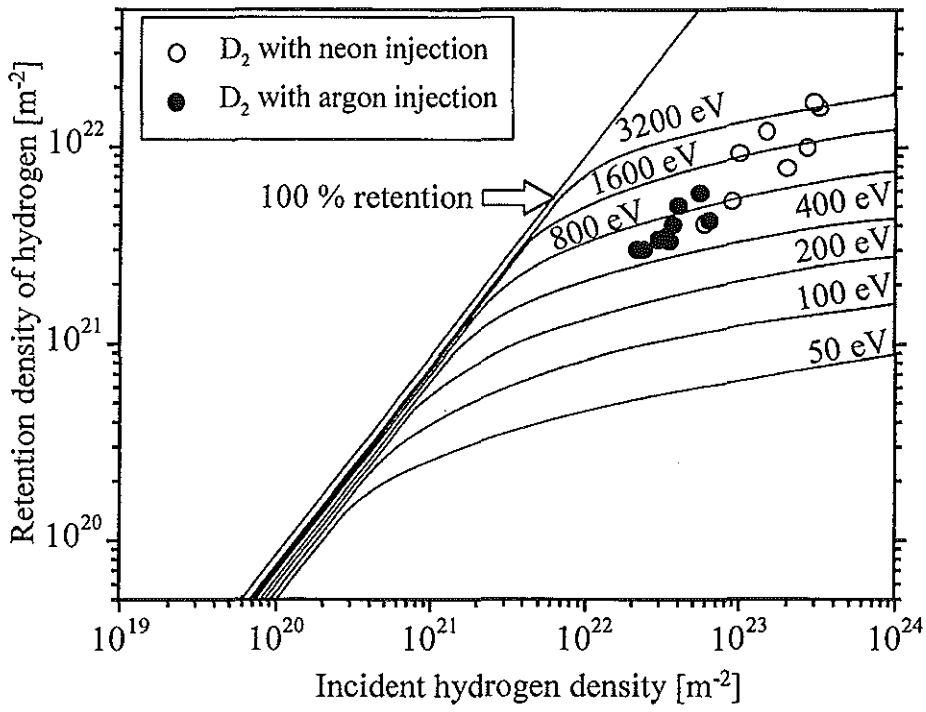

Figure 6-24 : Comparison of hydrogen retention density measured by Snifferprobe (circles) with that calculated by TRIM (solid line: deuterium with a maxwellian distribution incident on carbon by W. R. Wampler et al. [Wam81]).

high hydrogen retention in the carbon probe of the Sniffer probe compared with the TRIM-code estimations originates from the deposition of carbon and boron impurities onto the target.

6.3.2.1 Comparison of argon and neon

Fig. 6-25 compares some of the results of Sniffer probe measurements for neon and argon for comparable plasma conditions (n_e = 5×10^{19} m^{-3}, and I_p = 400 kA). Fig. 6-25(a) shows the ratio of impinging neon and argon to the impinging hydrogen flux. The neon flux ratios at the position of the Sniffer probe (r = 0.49 m) are significantly larger than that of argon. It should be noted, however, that we observe at the measuring position of the Sniffer probe a significantly lower hydrogen flux (factor of five) for discharges with argon injection compared with the neon injection conditions. This behaviour is not fully understood but results in the strong change of the absolute fluxes of neon and argon in the Sniffer probe for similar conditions. In order to avoid this influence, we compare thus relative flux ratios of

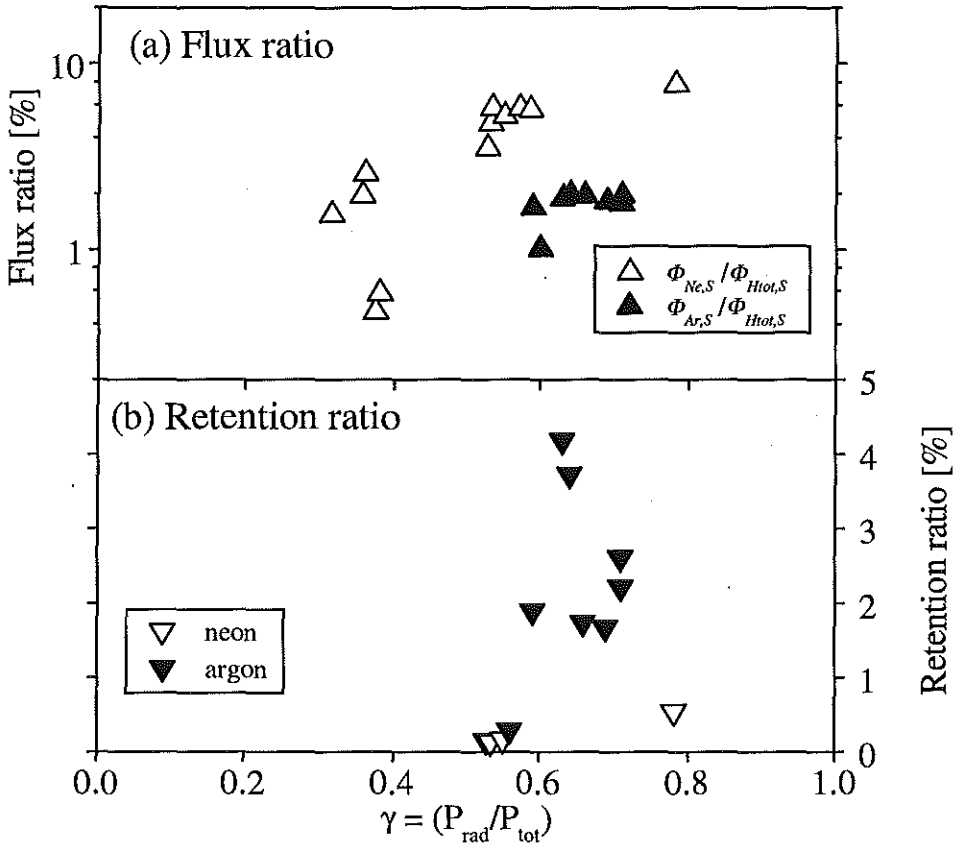

Figure 6-25 : Comparison of neon and argon experiment measured by the Sniffer probe (n_e = 5×10^{19} m^{-3}, and I_p = 400 kA): **(a)** flux ratios of neon and argon to hydrogen ($\Phi_{Ne,S}/\Phi_{Htot,S}$, $\Phi_{Ar,S}/\Phi_{Htot,S}$) and **(d)** retention ratios of neon and argon.

neon and argon to hydrogen. Fig. 6-25(b) compares the retention ratios of retained to the incident amount of neon and argon. As discussed in section 6.2.1.1, argon is retained much more effectively than neon.

6.3.2.2 Plasma current dependence and comparison with global observations

Fig. 6-26 shows the incident argon and hydrogen fluxes, their concentration and the retention density of argon measured by Sniffer probe for the different plasma currents I_p. With increasing plasma current, both the argon and hydrogen fluxes decrease significantly. It

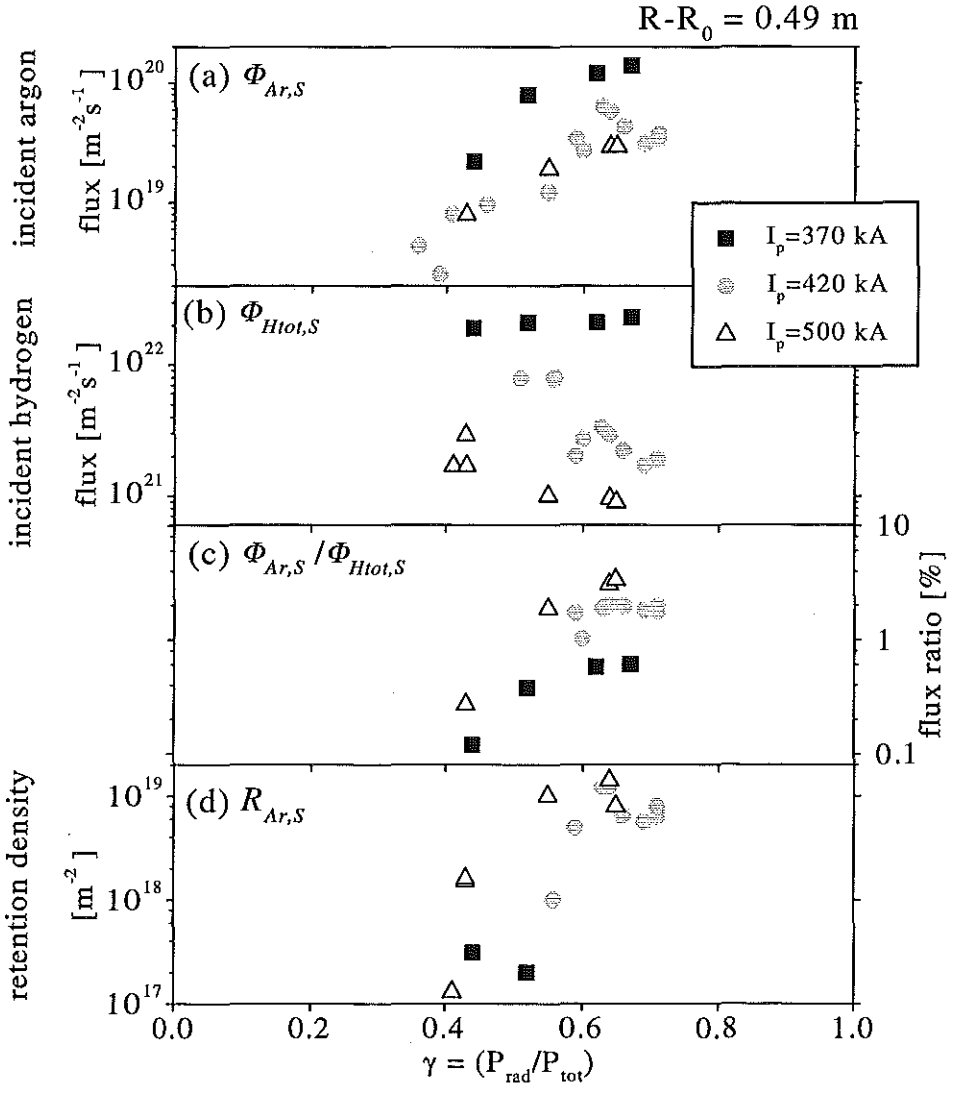

Figure 6-26 : Plasma current I_p dependence of **(a)** incident argon flux ($\Phi_{Ar,S}$), **(b)** incident hydrogen flux ($\Phi_{Htot,S}$) with argon injection, **(c)** flux ratios of argon to hydrogen ($\Phi_{Ar,S}/\Phi_{Htot,S}$) and **(d)** retention density of argon ($R_{Ar,S}$) in graphite measured by the Sniffer probe ($n_e = 5\times10^{19}$ m^{-3}).

should be noted, however, that the decrease of the hydrogen flux with increasing I_p is much greater than that of argon (~ factor 10). The decrease of the hydrogen flux ($\Phi_{Htot,S}$) is, at first, due to the improvement of confinement with increasing I_p, which is measured also by other diagnostic techniques such as the He-beam diagnostics. As a result of the different hydrogen and argon flux behaviour, the ***ratio of incident argon and hydrogen fluxes*** ($\Phi_{Ar,S}/\Phi_{Htot,S}$), as shown in fig. 6-26(c), increases with increasing I_p. As a consequence the ion-induced release of argon by the simultaneous impact of hydrogen decreases. This is believed to be the reason why the retention density of argon increases with increasing in I_p in fig. 6-26(d) despite the decrease of the incident argon flux

Fig. 6-27 compares the retention densities of argon measured by Sniffer probe ($R_{Ar,S}$) with those by global observation ($R_{Ar,G}$) for the different plasma currents I_p. The retention density measured by Sniffer probe ($R_{Ar,S}$) is somewhat larger than that by global observation ($R_{Ar,G}$). A plausible explanation of this discrepancy is already given in 6.1.2.2.

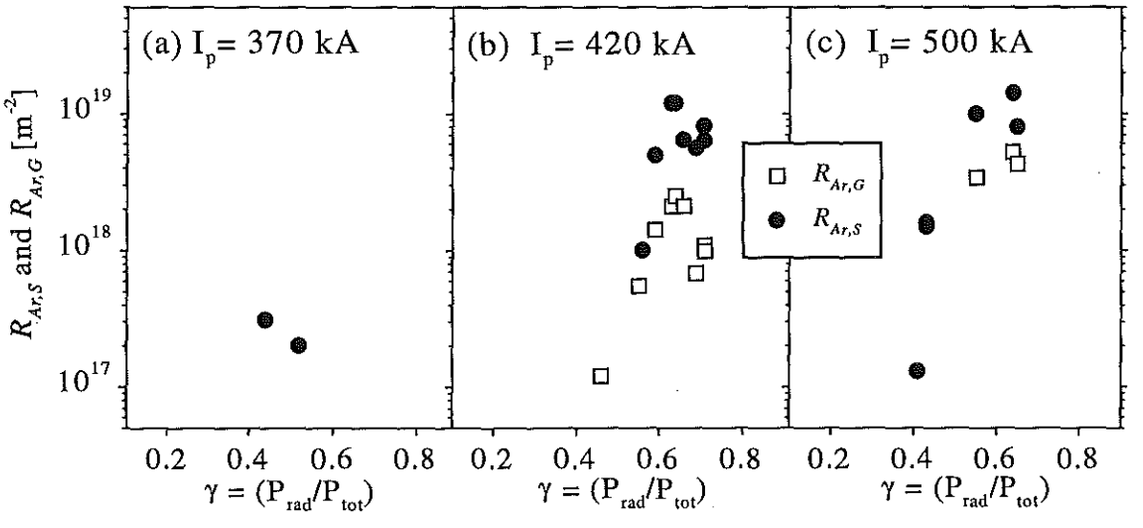

Figure 6-27 : Comparison of argon retention density in graphite measured by global observation ($R_{Ar,G}$) and in the sample of the Sniffer probe ($R_{Ar,S}$) for different plasma current I_p: **(a)** I_p = 370 kA, **(b)** I_p = 420 kA and **(c)** I_p = 500 kA.

6.3.2.3 Comparison with the ion beam experiments

It is of great interest to compare the results of TEXTOR experiments with those obtained in the ion beam experiment. Fig. 6-28 shows that the retention densities of argon measured by Sniffer probe are smaller than those obtained by the ion beam experiments. The same general behaviour is already observed for the neon experiments and can be explained by ***the influence of the ion-induced release of argon due to the simultaneously incident hydrogen ions***. The

discrepancy however is much less than that of neon and the retention ratio of argon (up to several %) is about one order of magnitude greater than that of neon (see fig. 6-25(b)). A possible explanation is that the ion-induced release of argon by hydrogen is less effective due to the higher mass of argon. However, for the case of higher plasma current I_p, the retention density measured in the Sniffer probe is only slightly smaller than that from the ion beam experiments. Taking into account the smaller energy of the argon ions in the plasma edge of TEXTOR compared with the ion beam experiment, the retention density of argon at higher I_p (= 500 kA) is only slightly smaller as expected from ion beam data.

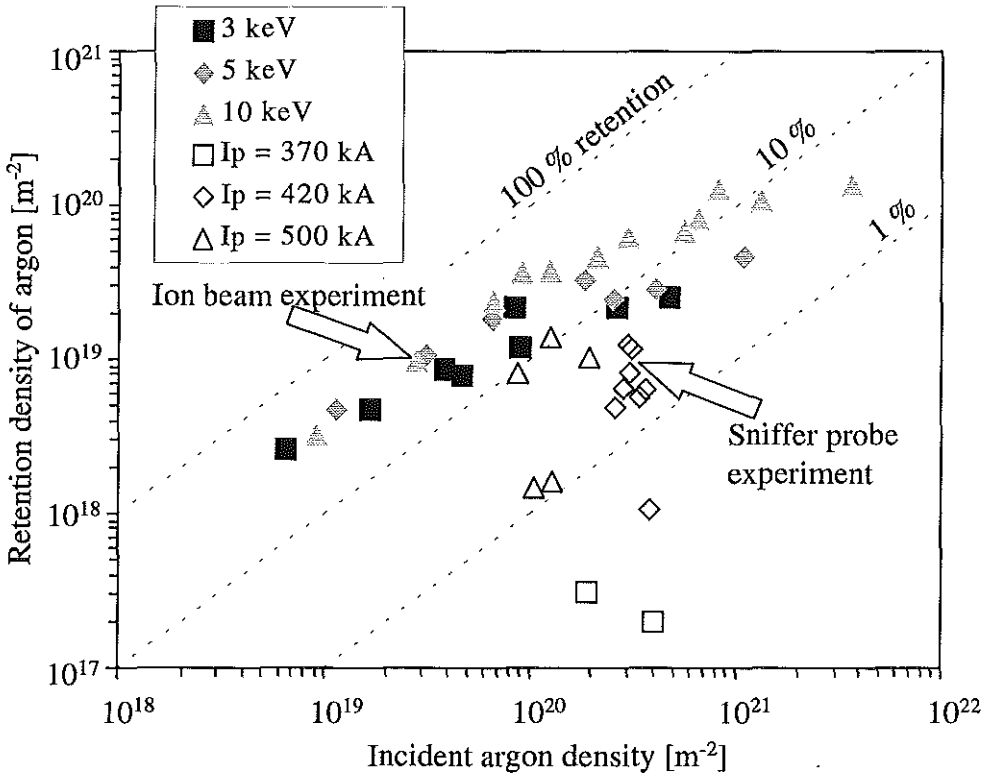

Figure 6-28 : Comparison of the retention density of argon in graphite measured by the Sniffer probe (open symbols probe) and in ion beam experiments (filled symbols).

6.3.3 Summary of the argon experiments in TEXTOR-94

From the overall balance of argon seeding and the effective particle confinement time, ***the absolute amount of argon in the plasma was derived.*** In order to achieve the same radiation level as for neon about half of the amount of argon is seeded. However the total amount of argon in the plasma is similar to that of neon. From the particle balance equation ***the temporal behaviour of the dynamic retention of argon in the walls is deduced.*** **In the**

first phase of the argon-injection (~ 200 ms) the majority of the argon seeded contributes to build-up the argon concentration in the plasma. The absolute amount of this plasma fuelling is similar to that of neon. **In the second phase,** which lasts in TEXTOR about 700 ms, the argon concentration in the plasma is already in the steady state phase, but the wall pumping plays still an important role. It decreases however to zero due to the saturation of the argon retention in the walls, which reaches up to 55 % of seeded argon. **In the third phase**, the pumping by the external ALT pump dominates which stays constant over the most argon injection phase (for constant density and radiation level). The outgassing of argon after the discharge slowly decays with a release rate $\propto t^{-1.1}$. The amount of released argon (56 % of seeded argon) is in relatively good agreement with that derived from the global dynamic retention (~ 50 %).

The absolute amount of argon and hydrogen ion fluxes at the position of the Sniffer probe were measured and the amount of argon and hydrogen retention in the graphite probe was measured by thermal desorption spectroscopy. The retention densities of hydrogen are somewhat larger than estimated from TRIM code calculations but in general agreement. The incident argon flux in the SOL is far smaller than that of neon. Due to the steepening of the radial hydrogen fluxes with increasing I_p, the absolute retention density of argon, despite smaller argon seeding, increases. The retention density of argon is somewhat larger than that deduced from global observation. ***The retention density of argon measured by the Sniffer probe is smaller than that measured in ion beam experiments*** with pure argon ions and extrapolated to the conditions at the plasma edge. This difference is most probably due to ion induced release of argon by the simultaneously incident hydrogen ions. This effect is, however, smaller than that for neon due to the larger mass number.

6.4 Experimental Results for Xenon

Small amounts of xenon were puffed in discharges with improved energy confinement. The main aim of the experiments was to study the transport of high-Z impurities in the plasma and its possible accumulation behaviour in the plasma core under RI mode conditions. The analysis of the recycling behaviour of xenon on the plasma facing surfaces was a by-product of these experiments. In order to prevent disruptions due to large radiation losses from xenon and possible accumulation, the overall quantity of xenon seeded was only in the order of 10^{17}, which is significantly smaller compared with that of Ne (~ 2×10^{19}) or Ar (~ 1×10^{19}). Single pulses of xenon were seeded by a fast gas injection system since the feed back control of xenon injection was not possible due to the small amounts of xenon injection [Ber97].

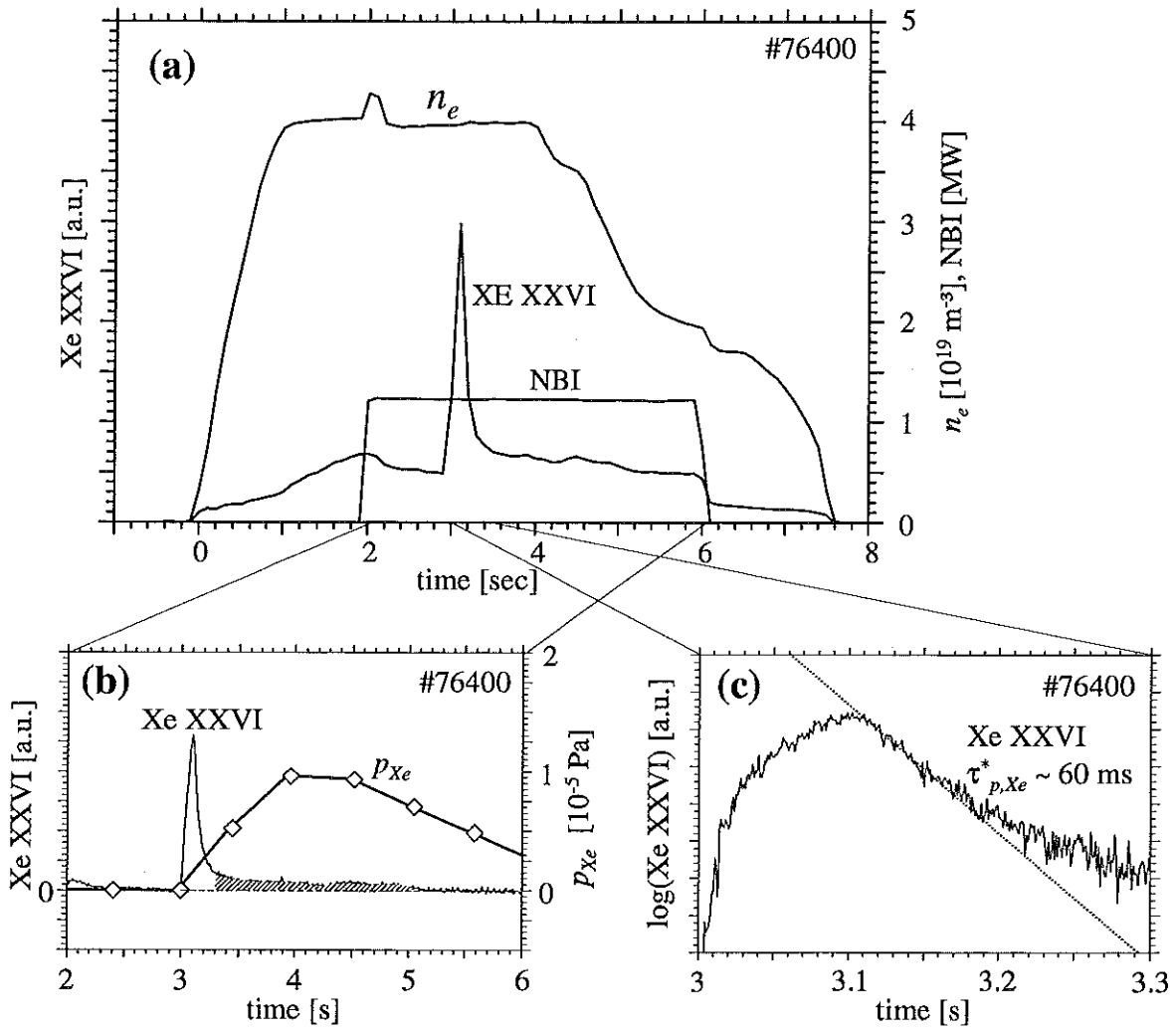

Figure 6-29 : (a) Typical signals of a RI-mode TEXTOR shot with xenon injection (#76400) (electron density n_e, NBI heating power, spectral line radiation of Xe XXVI, (b) Xe XXVI and xenon partial pressure p_{Xe} (both background subtracted) in linear scale, (c) Xe XXVI in semi-log scale.

Fig. 6-29(a) shows the general features of the xenon injection by displaying the line average density (n_e), the duration of the neutral beam injection and the temporal behaviour of Xe XXVI emission line measured spectroscopically by a viewing line trough the plasma. A xenon pulse was injected at t = 2 s causing a fast rise of the Xe XXVI line radiation which decays then rather fast. Fig. 6-29(b) shows the temporal behaviour of the neutral xenon partial pressure during the gas injection. The measurable pressure of neutral xenon, about 10^{-5} Pa, is very small, which is smaller than 0.1 % of the hydrogen neutral pressure during the discharge. As already discussed in 5.2.3.1, the time resolution of the mass spectroscopic system for such heavy masses is bad and thus does not allow a clear analysis of the fast temporal behaviour of the xenon neutral gas pressure during the discharge. The time behaviour of the xenon outgassing after the discharge however, as it will discussed later, can be measured very well with the mass spectrometer.

6.4.1 Global observation

6.4.1.1 Recycling of xenon during the discharge

As can be seen in fig. 6-29(b), the spectroscopic signal of the Xe XXVI line (λ = 17.4 nm, time resolution 1 msec, measured by a gracing incident monochrometer [Ber97]) shows a very fast decay of xenon after its injection. The spectrometer measures a highly ionized xenon state emitted from the centre of the plasma. Fig. 6-29(c) shows the decay in a semilogarithmic plot, from which one can deduce an effective confinement time ($\tau^*_{p,Xe}$) of ~ 60 msec. This is in good agreement with that evaluated by Bertschinger et al. [Ber97] ($\tau^*_{p,Xe}$: 40 - 80 msec) in which the effective particle confinement of xenon in TEXTOR discharges with different plasma conditions has been investigated in more detail.

Fig 6-29(b) shows clearly that the wall pumping of xenon is very effective: about 0.5 sec after the Xe-injection, Xe XXVI levels off to a small value, which is however somewhat greater than that before the Xe-injection (see shadowed area). This is a valid sign of xenon recycling during the discharge. Taking into account that the measured effective particle confinement times of xenon ($\tau^*_{p,Xe}$ ~ 60 ms) are similar to that of the hydrogenic particle confinement time [Unt97], the recycling coefficient of xenon at the wall is in the order of 0.5 or lower.

6.4.1.2 Outgassing of xenon after the discharge

Fig. 6-30(a) shows the typical time evolution of the xenon and hydrogenic partial pressure (HD : m/e = 3) after the discharge measured by mass spectrometer. Both the hydrogenic pressure and the xenon partial pressure rise sharply after the end of the discharge. This pressure rise is, as already discussed in 6.2.1.3, due to the continuous outgassing of hydrogen and xenon from the walls: with the termination of the plasma, the ionization of the outgassed neutrals by the plasma (*plasma pumping*) ceases, and the neutrals can fill the TEXTOR volume resulting in the sharp rise of the neutral pressure. As shown in fig. 6-30(a), xenon has a much longer outgassing tail than that of the hydrogen. Fig. 6-30(b) shows the time dependencies of the xenon partial pressures after a discharge with xenon injection

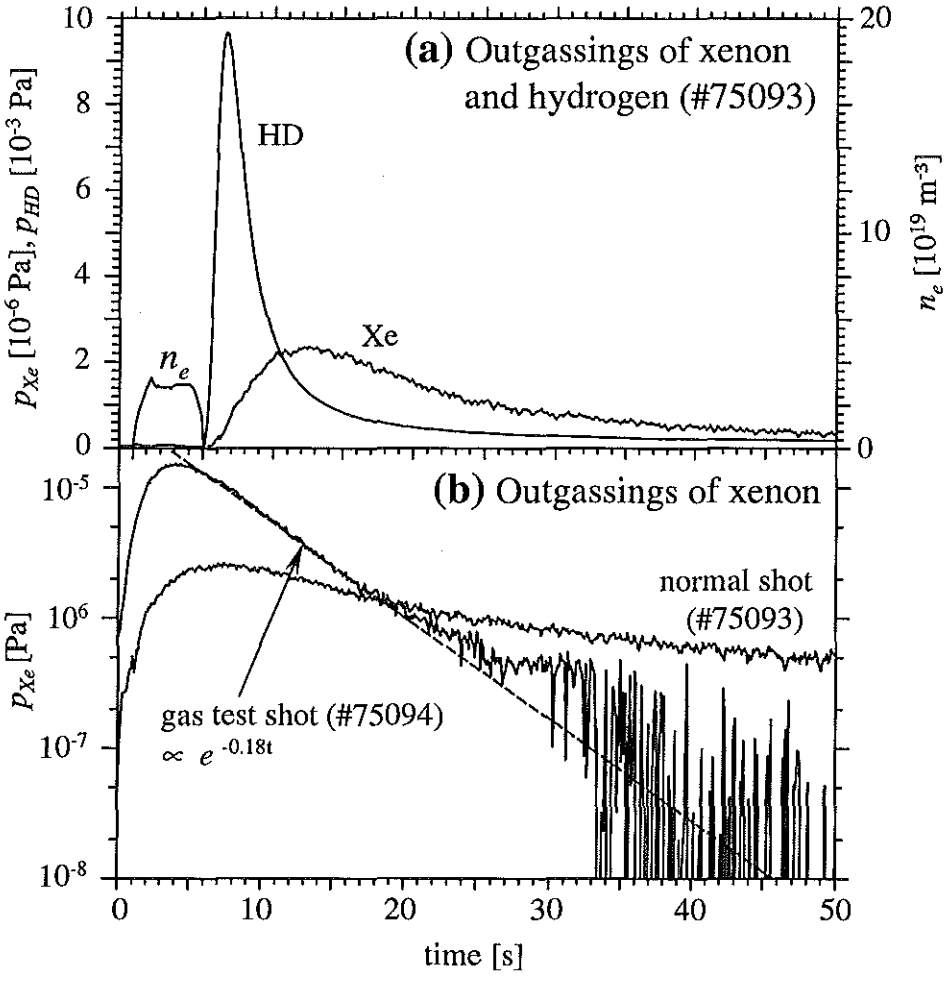

Figure 6-30 : **(a)** Typical time evolution of Xe and HD outgassing after a TEXTOR discharge (#75093) with xenon injection **(b)** comparison of the xenon partial pressure (p_{Xe}) with same xenon seeding (after a normal shot (#75093) and at a gas test shot (#75094)).

(#75093) and a gas test shot (#75094). As expected, the xenon partial pressure after the gas test shot follows an exponential function ($\propto e^{-0.18t}$), from which the pumping speed for xenon is derived (S_{Xe} = 3.4 m^3/s for 6 ALT-II pumps, main TEXTOR turbo pump, one NI-duct open). After the xenon injection during the discharge however, one finds a remarkably slower decay of the xenon partial pressure. Considering the low recycling ratio of xenon during the discharge and this slowly decaying release rate after the discharge, one can conclude that xenon is retained in the wall during the discharge and then released slowly during the rest of the discharge and after the discharge from the walls with a slow release rate.

In order to analyse the slowly decaying release rate of xenon in more detail, the release rates of xenon as a function of time have been derived from the measured partial pressure of xenon at each shot. In the same way as argon in 6.3.1.3, the release rate is obtained from the partial pressure (p_{Xe}):

$$Q_{Xe}(t) = \{\frac{dp_{Xe}(t)}{dt} \cdot V + p_{Xe}(t) \cdot S_{Xe}\} \cdot \frac{1}{RT} \text{ [1/sec]} \qquad (6\text{-}18)$$

where V is the TEXTOR volume (= 17 m^3), S_{Xe} is the pumping speed of TEXTOR for xenon derived above and $\frac{1}{RT} = \frac{273}{T_w} 2.64 \cdot 10^{20}$ Pa^{-1}m^{-3}. Fig. 6-31 shows the release rate of xenon evaluated from the xenon partial pressure in a log-log plot versus time. Though in fig. 6-31 the release rate is only plotted until t = 50 s, this power law is valid from the beginning of the

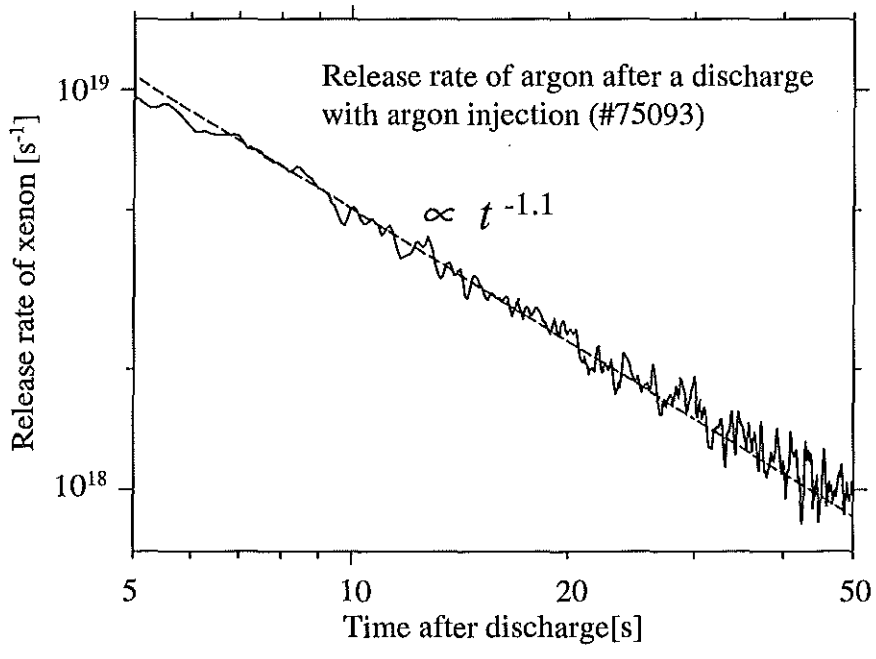

Figure 6-31 : Time evolution of the release rate of xenon after a discharge with xenon injection (#75093) (log-log scale).

outgassing till the beginning of next shot (~ 300 s). It is also relatively independent of the plasma conditions like the density or the quantity of xenon seeding. As can be seen, the release rate of xenon can be fitted very well with a power law of $Q_{Xe}(t) \propto t^{-1.1}$, which is just same as that of argon (see fig. 6-22).

Basically, the temporal behaviour of the release rate explains the physical process which determines the outgassing behaviour. As discussed by Philipps et al. [Phi92], the release can be in general determined by either detrapping from trap sites, diffusion processes, or by recombination. Since xenon and argon exist as a monatom, recombination can not be the mechanism concerned in this case. A simple thermally activated detrapping of xenon from a special type of trap site should results in an exponential behaviour of the outgassing with time, as can be seen in fig. 6-31, which is obviously not the case. A diffusion limited release from the erosion dominated region should approach to a $t^{-1.5}$ release rate in a log-log plot of the release rate for times after the end of discharge, which is a too fast decrease to explain our case alone. By the way a diffusion limited release from the deposition dominated region follows a time dependence of $t^{-0.5}$ for a fairly long time period. Taking into account the negligibly small diffusion coefficient of xenon in graphite and the deposition of carbon layer is observed in the tokamak walls, it could be carefully assumed that both two latter diffusion limited releases play reasonable roles in our case. As a result, the measured release behaviour can not be understood as any single physical process like detrapping or diffusion but, as discussed by Philipps et al. [Phi92], as a result of the combination of different processes.

The absolute amount of xenon outgassing has been evaluated by calibrating the mass spectrometer against the integral of the xenon outgassing after the gas test shot ($\int Q_{GT,Xe}(t)$). By comparing the integral of the xenon outgassing after a discharge with xenon injection (#75093, $\gamma \sim 0.32$), one finds that the amount of outgassing reaches 56 % of injected xenon. Taking into account that the amount of xenon in the plasma was very small, most of the outgassing of xenon is regarded to be released from the walls. Then recollecting that the retention of argon the walls ranges 30 ($\gamma \sim 0.5$) – 55 % ($\gamma \sim 0.8$) of argon seeded and that the radiation level of this discharge (#75093, $\gamma \sim 0.32$) was very low, it is considered the retention of xenon (~ 56 % of xenon seeded) is much larger than that of argon.

6.4.2 Summary of the xenon experiments in TEXTOR-94

Small amounts of xenon puffed during the discharge disappears from the plasma very fast with an effective particle confinement time of ~ 60 ms. They are thus pumped out effectively during the discharge, implying a low recycling due to the effective wall pumping. After the xenon retention in the wall is saturated, xenon is slowly released from the wall. This results in a small Xe-signal during the rest of the discharge and the sharp rise of neutral xenon partial

pressure at the end of the discharges. The retained xenon is released with a low release rate which can be well described with a power law ($\propto t^{-1.1}$). About half of the seeded xenon was released after the end of discharge as outgassing, which is similar to that of argon. Taking into account the low recycling ratio of xenon, most of outgassed xenon is considered to be released from the walls. The retention of xenon in the walls (> 56 %) is larger than that of argon (up to 50 %) for the similar plasma condition.

Observing the discharges with different amount of xenon injection, the amount of outgassing was in good agreement with the amount of xenon injection. However an increase of outgassing ratio after repeated discharges with same amount of xenon injection, i.e. saturation of xenon retention in the wall, was not to measure since the plasma conditions were not identical during this series of discharges. Though the valid memory effect was found in discharges with xenon injection, a fine systematic, as was by neon and argon, was not found.

7. Summary

A comprehensive study of the retention and recycling of noble gases (Ne, Ar and Xe) has been performed both in an ion beam apparatus and in TEXTOR-94.

In section 4 (ion beam experiment), irradiations of neon and argon with different ion energies (2 – 10 keV) onto graphite (EK98) are described. In the early phase of the irradiation, the reemission yields rise and are saturated to unity after a certain incident ion fluence (saturation fluence). This behaviour is similar for neon and argon. The saturation fluence increases with increasing ion energy, however the saturation fluence of neon is larger than that of argon. Both neon and argon are desorbed thermally from the graphite. *The desorption processes of both neon and argon are first order ones.* The desorption spectra of argon is broader than that of neon and the maximum temperature (850 K) is somewhat higher than that of neon (780 K). From the maximum temperature the binding energies of neon and argon are derived as 2.06 eV and 2.35 eV respectively. For the case of neon, almost 100 % of incident neon are retained in the early phase and after that the retention of neon decreases slowly until it is saturated. The retention of argon, which never reaches 100 % even at lower fluence, is also saturated after a certain fluence. ***In ion beam experiments the amount of retained neon is larger than that of argon for the same incident fluence.*** The saturation retention of neon and argon are almost independent of the ion energy and the saturation concentration of neon (Ne/C = 0.15 for 10 keV Ne^+ up to Ne/C = 0.55 for 2 keV Ne^+) is larger than that of argon (Ar/C = 0.06 for 10 keV Ar^+ up to Ar/C = 0.18 for 3 keV Ar^+) for comparable ion energies.

The dependence of the reemission and desorption characteristic on the sample temperature was investigated for neon and argon. As the sample temperature increases, more neon and argon are reemitted during the irradiation. At 1200 K practically all the incident neon and argon are immediately reemitted. Accordingly, the amount of desorbed neon and argon decreases with increasing sample temperature and above 1200 K no desorption was observed. The desorption spectra are shifted toward higher temperatures with increasing sample temperature. What is remarkable, though not yet understood, is that the desorption spectra which is not within the envelope of that at room temperature but shifted beyond it.

Ion induced release of neon was simulated by irradiating the neon-saturated graphite with 2 keV D_2^+ ions. No significant ion induced release of neon was observed. For a more accurate simulation of this effect, lower energies of both ions and a much higher fluence of deuterium ion might be needed. The diffusion of neon and argon were investigated in an identical way. Both neon and argon show no sign of a significant diffusion at room temperature. Argon shows no diffusion even at elevated temperatures of 600 and 800 K.

In section 6 (TEXTOR experiment), the retention and recycling characteristics of neon, argon and xenon are described investigated via indirect (global observation and outgassing) and direct measurement (Sniffer probe).

In section 6.1, ***it was possible to derive the absolute amount of neon in the plasma***, from the overall balance of neon seeding and pumping. From the particle balance equation ***the temporal behaviour of the absolute amount of dynamic retention of neon in the walls was deduced.*** In the first phase of the neon-injection (~ 100 ms), the majority of the neon seeded contributes to build-up the neon concentration in the plasma (*plasma pumping*). In the second phase, which lasts in TEXTOR about 600 ms, the *wall pumping* plays a major role. It decreases however to zero within one discharge due to the saturation of the neon retention in the walls. The neon exhaust by the ALT pumps stays constant over the neon injection phase (for constant density and radiation level) and is the only neon sink for the rest of the neon seeding. The retention of neon in the walls can also be seen from the fact that neon is released from the walls in discharges without neon seeding after a series of discharges with neon seeding. (***memory effect***).

The absolute amount of neon and hydrogen ion fluxes in the scrape off layer during the discharges was measured by the Sniffer probe and the amount of neon and hydrogen retention in the graphite sample was measured by thermal desorption spectroscopy in the Sniffer probe after the discharge. The hydrogen fluxes decreases significantly when neon is injected and the neon to hydrogen flux ratio at high radiation levels ($\gamma \sim 0.8$) extends from about 5 % at the high plasma densities (6×10^{19} m^{-3}) up to 30 % at low density (4×10^{19} m^{-3}). The comparison of the neon concentrations deduced from different measurements, i.e. different radial position, indicates that the radial profile of the ***neon concentration must be hollow-like***. The retention of neon in graphite measured in the Sniffer probe is up to two order of magnitudes smaller than that measured in ion beam experiment with pure neon ions and extrapolated to the conditions at the plasma edge. This difference is most probably due to the ion induced release of neon by the majority of the hydrogen ions which always impinge simultaneously with the neon ions on the walls in a fusion experiment.

In section 6.2, the absolute amount of argon in the plasma was derived, from the overall balance of argon seeding and pumping. In order to achieve the same radiation level as in the neon case ***only half of the amount of argon was needed. However the total amount of argon in the plasma was similar to that of neon***. From the particle balance equation the temporal behaviour of the absolute amount of dynamic retention of argon in the walls is deduced. The overall temporal behaviour of the retention of argon is similar to that of neon. In the first phase of the argon-injection (~ 200 ms), the majority of the argon seeded contributes to build-up the argon concentration in the plasma. The absolute amount of this ***plasma pumping, i.e. the amount of argon in plasma, is similar to that of neon***. This indicates a different radial

profile of argon. In the second phase, which lasts about 700 ms in TEXTOR, the wall pumping plays an important role. It decreases however to zero due to the saturation of the argon retention in the walls, which reaches up to 55 % of seeded argon. In the third phase, ALT pumping is the only argon sink, which stays constant over most of the argon injection phase (for constant density and radiation level)

Comparing the results of the global observation of argon with those of neon, the contribution of wall pumping of argon is much greater than that of neon. This can be explained by the less effective ion induced release of argon by hydrogen due to the heavier mass of argon. From the outgassing of argon after the discharge, a slowly decaying release rate of argon ($\propto t^{-1.1}$) is derived and ***the amount of released argon*** (56 % of seeded argon) is relatively ***in accordance with that deduced from the dynamic retention*** of argon in graphite (~ 50 %).

In the same way as neon, the absolute amount of argon and hydrogen ion fluxes were measured by the Sniffer probe and the amount of argon and hydrogen retention in graphite was measured by thermal desorption spectroscopy. The retention densities of hydrogen in discharges with neon and argon injection are relatively in accordance with that calculated by the TRIM code calculation. This shows that the retention of hydrogen is practically not affected by the injection of neon or argon. Though the ratio of argon to hydrogen flux is smaller than that of neon, the retention ratio of argon is larger than that of neon. This is explained again by a less effective ion induced release of argon by hydrogen, due to the higher atomic mass of argon compared with neon. Due to the decrease of the hydrogen flux in the scrape off layer with increasing plasma current, the retention density of argon, despite smaller argon seeding, increases with increasing plasma current. ***The retention density of argon in graphite measured in the Sniffer probe is smaller than that measured in the ion beam experiments*** with pure argon ions. This difference, most probably due to ion induced release of argon by the simultaneously incident hydrogen ions, is however smaller than that of neon.

In section 6.3, it is described that a small amount of xenon puffed during a discharge disappears from the plasma very fast with an effective particle confinement time of ~ 60 ms, implying a *low recycling due to the effective wall pumping*. From the outgassing after the discharge, the amount of retained xenon was estimated. Taking into account the very small amount of xenon in the plasma, up to half of the xenon injected are retained in the walls. This is somewhat larger than that of argon. The retained xenon is then released by low release rate with a power law ($\propto t^{-1.1}$), which is exactly same as that of argon. Though it should be further investigated, the slope of the release rates indicates that the release of argon and xenon have to be explained by a combination of different processes.

Up to now there are two investigations concerning the retention of noble gases in graphite with divergent results. Choi et al. [Cho93] have investigated the retention of noble gases (He, Ne and Ar) in graphite (single crystal graphite) irradiated with low energy (10 – 600 eV) ion beams. They found that the retention density of neon in graphite at its saturation (~ 1×10^{19} m^{-2}) is greater than that of argon (~ 5×10^{18} m^{-2}) and that the retention densities at saturation are almost independent of the ion energy both for neon and argon. In the ion beam experiment of this thesis (2 – 10 keV Ne^+ and Ar^+), similar tendencies were measured up to higher fluence (~ 1×10^{22} m^{-2}). However, in this thesis the retention densities of neon in graphite (EK98) at saturation (~ 4×10^{20} m^{-2} for neon and ~ 1×10^{20} m^{-2} for argon) are greater than those measured by Choi et al.. A difference in both experiments is the density of the graphite. In this thesis EK98 (ρ = 1.86 g/cm^3) was used compared with the single crystal graphite (HOPG, ρ = 2.2 g/cm^3) in Choi et al.. It is however not systematically investigated whether the density determines the saturation retention or not.

Brosset et al. [Bro97] have investigated the effect of the simultaneous exposure of graphite with neon and hydrogen on the retention of neon in graphite (also fine grain graphite (5890PT) , Le Carbon Lorraine, ρ = 1.8 g/cm^3 [Del87]) with a DC glow discharge (T_e ~ 15 eV). Graphite was exposed to three different plasmas: (a) a pure neon plasma, (b) a mixed hydrogen and neon plasma (nearly 1:1) and (c) a hydrogen plasma after a exposure to a pure neon plasma. First, the saturation retention of pure neon exposure at a high fluence of 6×10^{22} m^{-2} is 9×10^{21} m^{-2}, which is more than one order of magnitude larger than that of the ion beam experiments (~ 4×10^{20} m^{-2}) in this thesis. The reason for this discrepancy can not be explained by the difference of the graphite density since the density of the graphite used in [Bro97] is practically same as that used in this thesis. Second, under the latter two conditions ((b),(c)), the amount of desorbed neon was about one order of magnitude smaller than that after the pure neon exposure. In this thesis the retention of neon in graphite exposed to TEXTOR plasmas was found to be more than one order of magnitude smaller than that measured in ion beam experiments. A plausible reason why in our experiments the difference between ion beam experiments and TEXTOR experiments is larger than in [Bro97] is that in TEXTOR the hydrogen fluence is more than one order of magnitude greater than that of neon, while both fluences of neon and hydrogen were same in [Bro97].

References

[Ali95] V. Kh. Alimov, B.M. U.Scherzer et al., J. Appl. Phys. **78(1)**, 137 (1995).

[Bal84] D.A. Baldwin, N. Shamir et al., Surf. Sci. **141**, 617 (1984).

[BalB86] "Partialdruckmessung in der Vakuumtechnik", Balzers (1996).

[Ber97] C. Bertschinger et al., Controlled Fusion and Plasma Physics, Proc. 24th Eur. Conf. (Berchtesgarden 1997), vol. 21A (Petit Lancy: European Physical Society) part IV, p.1709.

[Bri98] M. Brix, Forschungszentrum Jülich, Jülich, Germany, private communication.

[Bro97] C. Brosset, J. Bardon et al., J. Nucl. Mater. **241-243**, 1093 (1997).

[Che96] V.N. Chernikov, W. Kesternich et al., J. Nucl. Mater. **227**, 157 (1996).

[Cho93] W. Choi, C. Kim et al., Surf. Sci. **281**, 323 (1993).

[Cum90] J. Cummings et al., "Power radiated from ITER and CIT by impurities", Princeton Plasma Physics Laboratory Report, PPPL-2702 (1990).

[Del79] W. Delle, K. Koizlik, H. Nickel; in "Graphitische Werkstoffe für den Einsatz in Kernreaktoren", Verlag Karl Thiemig, München (1979), pp. 69.

[Del87] W. Delle, J. Linke, H. Nickel; in "Comparison of high purity fine grain graphites from different supplies with regard to physical, mechanicla and thermal properties", Forschungszentrum Jülich Special Report, Jül-Spez-401, (1987).

[Doy80] B. Doyle, W.R. Wampler et al., J. Nucl. Mater. **93 & 94**, 551 (1980).

[Doy82] B. Doyle, J. Nucl. Mater. **111 & 112**, 628 (1982).

[Eck96] W. Eckstein, V. Philipps, in "Physical Processes of the Interaction of Fusion Plasmas with Solids", (W.O. Hofer, J. Roth, eds.), Academic Press, San Diego (1996), pp. 93.

[Eck98] W. Eckstein, "Sputtering, Reflection and Range Values for Plasma Edge Codes", Max-Plank-Institut für Plasmaphysik Report, IPP 9/117 (1998).

[Ede86] C. Edelmann, in "Vakuumtechnik", VEB Fachbuchverlag, Leipzig (1986), pp. 66.

[Ehr96] J.K. Ehrenberg, in "Physical Processes of the Interaction of Fusion Plasmas with Solids", ed., W.O. Hofer, J. Roth, Academic Press, San Diego (1996), pp. 35.

[Goe89] D.M, Goebel, R.W. Conn et al., J. Nucl. Mater. **162-164**, 115 (1989).

[Gum90] B. Gumhalter, M. Milun et al., in "Selected Studies of Adsorption on metal and semiconductor surfaces", WEKA-Druck, Linnich (1990), pp. 10.

[Han90] G. Hansali, J.P. Biberian et al., J. Nucl. Mater. **171**, 395 (1990).

[Her98] Heraeus, "Grundwerte der Thermospannungen in mV nach DIN 43710".

[Jas99] R. Jaspers, Forschungszentrum Jülich, Jülich, Germany, private communication.

[Jen77] R.V. Jensen and D.E. Post, in "Atomic Data and Nuclear Data Tables", Vol. 20, No. 5 (1977).

[Laf98] J.M. Lafferty, in "Foundations of vacuum science and technology", John Wiley & Sons, New York, (1998), pp. 81.

[Lin61] J. Lindhard, M. Scharff, Phys. Rev., **124**, 647 (1961).

[Mes96] A. M. Messiaen, J. Ongena et al., Phys. Rev. Lett. **77**, 2487 (1996).

[Möl86] W. Möller, J. Roth, in "Physics of Plasma-Wall-Interactions in Controlled Fusion", (D. E. Post and, R. Behrish, eds.), p. 439, NATO ASI series, series B: Physics Vol. 131, Plenum, New York/London (1986).

[Ong97] J. Ongena, R.V. Bundy et al., Controlled Fusion and Plasma Physics, Proc. 24th Eur. Conf. (Berchtesgarden 1997), vol. 21A (Petit Lancy: European Physical Society) part IV, 1693.

[Phi87] V. Philipps, E. Vietzke et al., J. Nucl. Mater. **145-147**, 292 (1987).

[Phi89] V. Philipps, E. Vietzke et al., J. Nucl. Mater. **162-164**, 550 (1989).

[Phi91] V. Philipps, E. Vietzke et al., J. Nucl. Mater. **179-181**, 25 (1991).

[Phi92] V. Philipps, J. Ehrenberg, J. Vac. Sci. Technol. **A 11(2)**, 437 (1992).

[Phi96] V. Philipps, A. Pospieszczyk et al., Phys. Scr., **T64**, 71 (1996).

[Phi98] V. Philipps, Trans. of Fus. Techn., **33**, 261 (1998).

[Rap96] J. Rapp, Ph.D. Thesis, Univ. Wuppertal, Forschungszentrum Jülich Report, Jül-3172 (1996).

[Red62] P.A. Redhead, Vacuum, **12**, 203 (1962).

[Ref94] A. Refke, Ph.D. Thesis, Univ. Düsseldorf, Forschungszentrum Jülich Report, Jül-2995 (1994).

[Rei98] D. Reiter, Trans. of Fus. Techn., **33**, 249 (1998).

[Rot83] J. Roth, in "Sputtering by Particle Bombardment II", (R. Behrisch, eds.), Springer-Verlag, Berlin/Heidelberg (1983), pp. 91.

[Rub96] M. Rubel, Royal Institute of Technology, Stockholm, Sweden, private communication.

[Sam89] U. Samm, P. Bogen, J. Nucl. Mater., **162-164**, 24 (1989).

[Sam93] U. Samm, G. Bertschinger et al., Plasma Phys. Control. Fusion, **35**, B167 (1993).

[Sam98] U. Samm, Trans. of Fus. Techn., **33**, 273 (1998).

[Sch98] B. Schweer, M. Brix et al., 13th International Conference on Plasma Surface Interaction in Controlled Fusion Devices, San Diego (1998), in press.

[Sig69] P. Sigmund, Phys. Rev. **184**, 2, 383 (1969).

[Sob81] I.I. Sobelman et al., in "Excitation of Atoms and Broadening of Spectral Lines", Springer, Berlin (1981).

[Sta86] P. Stangeby, in "Physics of Plasma-Wall-Interactions in Controlled Fusion", (D. E. Post and, R. Behrish, eds.), p. 41, NATO ASI series, series B: Physics Vol. 131, Plenum, New York/London (1986).

[Sum79] H.P. Summers, R. W. P. McWhirter, J. Phys. **B12**, 2387 (1979).

[Tok92] M. Tokar, "One dimensional modelling of a tokamak edge plasma under conditions of strong impurity radiation", Forschungszentrum Jülich Report, Jül-2988, (1992).

[Tok94] M. Tokar, Nucl. Fusion, **34** (6), 853, (1994).

[Unt95] B. Unterberg, Ph.D. Thesis, Univ. Bochum, Forschungszentrum Jülich Report, Jül-3036 (1995).

[Unt97] B. Unterberg, A.M. Messiaen et al., Plasma Phys. Control. Fusion, **39**, B189 (1997).

[Unt98] B. Unterberg, M. Brix et al., 13th International Conference on Plasma Surface Interaction in Controlled Fusion Devices, San Diego (1998), in press.

[Unt99] B. Unterberg, Forschungszentrum Jülich, Jülich, Germany, private communication.

[Val77] L. Valyi, in "Atom and ion sources", John Wiley & Sons, London (1977), pp. 315.

[Vie82] E. Vietzke, K. Flaskamp et al., J. Nucl. Mater. **111 & 112**, 763 (1982).

[Wam81] W.R. Wampler, D.K. Brice, J. Nucl. Mater. **102**, 304 (1981).

[Wes87] J. Wesson, in "Tokamak" , Oxford University press, Oxford (1987), p. 8.

[WesB87] F. Weschenfelder et al., Controlled Fusion and Plasma Physics, Proc. 24th Eur. Conf. (Berchtesgarden 1997), vol. 21A (Petit Lancy: European Physical Society) part IV, p. 1729.

[Wil73] R.G. Wilson, G.R. Brewer, in "Ion Beams: with applications to Ion Implantation", John Wiley and Sons, New York (1973), pp. 152.

[Win93] J. Winter, G. Esser et al., Phys. Rev. Lett. **71**, 10, 1549 (1993).

[Win96] J. Winter, "Wall Conditioning in Fusion Devices and its influence on Plasma Performance", Forschungszentrum Jülich Report, Jül-3217 (1996).

[WinB74] H.F. Winters, P. Sigmund, J. Appl. Phys. **45** (11), 4760 (1974).

[Wol84] G.H. Wolf, J. Nucl. Mater., **122 & 123**, 1124 (1984).

[Zie84] J.F. Ziegler; in "Ion implantation science and technology", Academic Press, Orlando (1984), pp. 51.

[Zie87] J.F. Ziegler, TRIM-88: The transport code of ions in matter, program manual.

Acknowledgements

I would like to thank my supervisor, Professor H. Nickel, for his invaluable guidance and support throughout this project. In addition, I am indebted to Dr. V. Philipps and Dr. E. Vietzke for their direction and encouragement. I am also appreciative of the valuable discussions with Dr. B. Unterberg and Dr. R. Jaspers. I would also like to recognize the contributions of the other members of our Plasma-Wall-Interaction group in the Institute of Plasma Physics in Forschungszentrum Jülich.

The financial support provided by the DAAD (Deutscher Akademischer Austauschdienst) is gratefully acknowledged.

I would like to thank my family, especially my wife Ji Yoon, for her unwavering patience and understanding.

Finally, I give all my thanks to God for his unimaginable grace.

Forschungszentrum Jülich

Jül-3670
July 1999
ISSN 0944-2952